

Atmospheric Channel Performance Measurements at 10 to 100 GHz

R.H. Espeland
E.J. Violette
K.C. Allen



U.S. DEPARTMENT OF COMMERCE
Malcolm Baldrige, Secretary

David J. Markey, Assistant Secretary
for Communications and Information

April 1984

TABLE OF CONTENTS

	<u>Page</u>
LIST OF FIGURES	v
ABSTRACT	1
1. INTRODUCTION	1
2. SYSTEM CAPABILITIES AND DESCRIPTION	4
2.1 Description of the Probe	5
2.2 Meteorological Instrumentation	14
2.3 Computer-Controlled Data Acquisition and Recording Equipment	15
3. DEVELOPMENT AND CALIBRATION OF THE 96.1-GHz CHANNEL	17
4. OPERATION OF THE DIAGNOSTIC PROBE AND DATA ANALYSIS	26
4.1 Calibration Path	27
4.2 11.8-km Path	27
4.2.1 On-Line, Direct-Path Pointing	27
4.2.2 Off-Line Pointing	32
4.2.3 Performance in the Presence of Multipath Signals	32
4.2.4 Performance During Rain	35
4.3 27.2-km Path	40
4.3.1 Seasonal Data	45
4.3.2 Fog, Snow and Rain Data	48
4.3.3 Multipath Fading	59
4.3.4 Propagation Conditions Analyzed with Impulse Response	67
5. STATISTICAL ANALYSES	75
5.1 Rain Attenuation	75
5.2 Water Vapor Content and Attenuation	89
5.3 Cumulative Distributions of Bit Error Rate	98
6. CONCLUSION	108
7. REFERENCES	112

LIST OF FIGURES

<u>FIGURE</u>		<u>PAGE</u>
2.1	Block diagram of the transmitter terminal.	6
2.2	Block diagram of the rf section of the receiver terminal.	8
2.3	Block diagram of the receiver demodulator.	9
2.4	Block diagram of the bit synchronizer, signal conditioner, and bit error receiver.	11
2.5	Block diagram of the impulse response cross-correlator.	13
2.6	Diagram of the data acquisition and recording equipment.	16
3.1	Block diagram of the 96.1-GHz transmitter.	18
3.2	Block diagram of the 96.1-GHz receiver rf stage and local oscillator source generator.	19
4.1	The system calibration path.	28
4.2	Photographs of the transmitter and receiver terminals on the calibration path.	29
4.3	A photograph and height profile of the 11.8-km path.	30
4.4	Selected RSL and BER recordings at 30.3-GHz and corresponding impulse response curves. a) with on-line pointing (receiving antenna at an elevation angle = 0 deg) b) with off-line pointing (receiving antenna at an elevation angle = -2 deg).	31
4.5	An ensemble of measured impulse response curves with the receiving antenna pointing at -2 deg (elevation angle).	33
4.6	A scatter plot of RSL and BER representing the system calibration response operating on the 11.8-km path.	34
4.7	RSL and BER data and a corresponding scatter-plot with the receiving antenna elevation angle at 0 deg.	36
4.8	RSL and BER data and a corresponding scatter plot with the receiving antenna elevation angle at -2 deg.	37
4.9	RSL and BER data and corresponding scatter plot with the receiving antenna elevation angle at -2 deg. Strong RSL variations.	38
4.10	Scatter plots of RSL and BER measured on the 11.8-km path during rainfall.	39
4.11	Height profile of the 27.2-km diagnostic path.	41
4.12	Photographs of the 27.2-km diagnostic path.	42
4.13	Typical spring-time records from the 27.2-km path showing bit-error-rates, received signal levels (11.4, 28.8, and 30.3 GHz) and rain-rate.	46

<u>FIGURE</u>		<u>PAGE</u>
4.14	Typical summer-time records from the 27.2-km path showing bit-error-rates, received signal levels (11.4, 28.8, and 30.3 GHz) and rain-rate.	47
4.15	Time series records for periods of fog on the 27.2-km path between the hours of 0300 and 1030 on February 25 and between the hours of 0500 and 1030 on March 24, 1983.	49
4.16	Time series records for periods of snow on the 27.2-km path occurring on March 16 and 17, 1983.	51
4.17	Time series records showing periods of rain and snow on the 27.2-km path on March 15, 1983.	52
4.18	Time series records showing periods of rain on the 27.2-km path occurring on June 12 and June 26, 1983.	53
4.19	Time series records showing results from the 27.2-km path during a rain storm between 1200 and 1600 hours on June 12, 1983.	55
4.20	Time series records from the 27.2-km path showing results during a rain storm between 1700 and 2100 hours on June 26, 1983.	57
4.21	Time series segments from the 27.2-km path during rain recorded on August 18 and August 21, 1983.	58
4.22	Time series records for periods of scintillation and fading on the 27.2-km path recorded on June 30 and July 6, 1983.	60
4.23	Time series segments from the 27.2-km path during periods of fading recorded on June 30, 1983.	61
4.24	Time series segments from the 27.2-km path during periods of fading recorded on July 6, 1983.	63
4.25	Time series records for periods of scintillation and fading on the 27.2-km path recorded on July 18, 1983.	64
4.26	Time series records during periods of scintillation and fading on the 27.2-km path recorded on August 12, 1983.	65
4.27	Time series segments during periods of fading on the 27.2-km path recorded on August 10 and 11, 1983.	66
4.28	A time series of BER and the received signal level at 30.3-GHz recorded September 23, 1983 between 1000 and 1100 on the 27.2-km path.	68
4.29	Selected impulse response curves recorded from the 27.2-km path between the hours of 1000 and 1100 on September 23, 1983.	69
4.30	A time series of BER and 30.3-GHz received signals recorded on the 27.2-km path during a period of moderate scintillation, 0700 to 0800 on September 23, 1983.	71
4.31	Selected impulse response curves recorded from the 27.2-km path between 0700 and 0800 hours on September 23, 1983.	72

<u>FIGURE</u>		<u>PAGE</u>
4.32	A time series of BER and the received signal levels of 30.3 GHz recorded during rain on the 27.2-km path, May 16, 1983.	73
4.33	Selected impulse response curves recorded during a period of rain on the 27.2-km path, May 16, 1983.	74
5.1	A time series record of 11.4 and 28.8-GHz signals recorded during periods of rain and snow on the 27.2-km path on March 15, 1983.	78
5.2	A cross-plot of 28.8 and 11.4-GHz signal amplitudes recorded between 0100 and 0500 MST, March 15, 1983.	79
5.3	Signal amplitude at 28.8 and 11.4-GHz for rain-rates of 1, 10, 100 mm/h as the rainy path length is varied from 0 to 27.2-km. Attenuations predicted using (5.4) with the a and b parameters of Table 1 for the Laws and Parson's low rain rate distribution.	81
5.4	Signal amplitude at 28.8 and 11.4-GHz for paths of 1, 10, and 27.2-km as the rain-rate is varied from 0 to 150 mm/h. Attenuations predicted using (5.4) with the a and b parameters of Table 1 for the Laws and Parson's low rain rate distribution.	82
5.5	Plots of attenuation ratios due to precipitation for 28.8 GHz compared to 11.4 GHz as a function of time of day. Symbols: M = morning, A = afternoon, E = evening, and N = night.	84
5.6	Plots of attenuation ratios due to precipitation for 28.8 GHz compared to 11.4 GHz as a function of fade depth at 28.8 GHz. Symbols: S = snow, C = convective rain (thunderstorms), and W = wide-spread rain.	85
5.7	A histogram of the ratio of attenuation (28.8/11.4 GHz) for all the precipitation events recorded on the 27.2-km path.	86
5.8	A histogram of the ratio of attenuation (28.8/11.4 GHz) for convective type (thunderstorm) rain events recorded on the 27.2-km path.	87
5.9	A histogram of the ratio of attenuation (28.8/11.4 GHz) for wide-spread rain events recorded on the 27.2-km path.	88
5.10	A histogram of the ratio of attenuation (28.8/11.4 GHz) for snow events recorded on the 27.2-km path.	90
5.11	A plot of the measured specific attenuation at 96.1-GHz versus the measured water vapor pressure.	92
5.12	A plot of the measured specific attenuation at 96.1-GHz (with the attenuation due to dry-air and water vapor lines below 1 THz subtracted out) versus the measured water vapor pressure.	93
5.13	A plot of the measured specific attenuation (with the attenuation due to dry-air and water vapor lines below 1 THz subtracted out) at 96.1-GHz versus data from the predicted continuum absorption using the Gaut-Reifenstein model.	95

<u>FIGURE</u>		<u>PAGE</u>
5.14	A plot of the measured specific attenuation (with the attenuation due to dry-air and water vapor lines below 1 THz subtracted out) at 96.1-GHz versus data from the predicted continuum absorption using the Rice-Ade model.	96
5.15	A plot of the measured specific attenuation (with the attenuation due to dry-air and water vapor lines below 1 THz subtracted out) at 96.1-GHz versus data from the predicted continuum absorption using the Liebe-Layton model.	97
5.16	Cumulative distribution of BER and the portion of the distribution contributed under each meteorological classification recorded during March, 1983 on the 27.2-km path.	100
5.17	Cumulative distribution of BER and the portion of the distribution contributed under each meteorological classification recorded during April, 1983 on the 27.2-km path.	102
5.18	Cumulative distribution of BER and the portion of the distribution contributed under each meteorological classification recorded during May, 1983 on the 27.2-km path.	103
5.19	Cumulative distribution of BER and the portion of the distribution contributed under each meteorological classification recorded during June, 1983 on the 27.2-km path.	104
5.20	Cumulative distribution of BER and the portion of the distribution contributed under each meteorological classification recorded during July, 1983 on the 27.2-km path.	105
5.21	Cumulative distribution of BER and the portion of the distribution contributed under each meteorological classification recorded during August, 1983 on the 27.2-km path.	106
5.22	Cumulative distribution of BER and the portion of the distribution contributed under each meteorological classification for all recorded data on the 27.2-km path from March through August, 1983.	107
5.23	Cumulative distributions of BER for each month on the 27.2-km path from March through August, 1983.	109

MEASUREMENTS AT 10 TO 100 GHz

R. H. Espeland, E. J. Violette, and K. C. Allen*

A diagnostic probe designed to investigate propagation at millimeter wavelengths was operated on 11.8 and 27.2-km line-of-sight paths near Boulder, CO. A 30.3-GHz carrier is biphase-shift-keying modulated at a 500 Mb/s with bit error rates less than 10^{-8} in clear air and a fade margin of about 30 dB on the 27.2-km path. In addition, fully coherent carrier wave channels at 11.4, 28.8, and 96.1 GHz provide data to analyze fade mechanisms and evaluate frequency dependent performance characteristics of the link. Data during fog, snow, rain, and clear-air fade events are included with statistical analyses of event occurrence, signal levels, and bit error rates. Time delay distortion and amplitude dispersion on the channel are also examined during fading events by the wide-band digital channel operated as an impulse probe. Rain attenuation, path absorption due to water vapor content, and seasonal variations as a function of frequency are presented and described.

Key Words: atmospheric; diagnostic; digital; millimeter waves, probe; propagation; water vapor; wide band

1. INTRODUCTION

One of the missions of the Institute for Telecommunication Sciences, National Telecommunications and Information Administration (ITS/NTIA) is to determine an effective means of managing the electromagnetic (EM) spectrum and to explore methods of extending its usable range. The radio spectrum which lies between 10 and 100 GHz probably can accommodate many existing and future telecommunication demands, particularly in the area of wide-band digital communication channels. Hardware and antenna size permit the use of small terminals to establish line-of-sight (LOS) links up to 50 km with considerable ease. However, two areas are preventing rapid development of this portion of the spectrum: (1) the expense of hardware and (2) weather-related factors that degrade performance and may produce a link outage. Hardware expense should be reduced by high-technology, low-cost quantity production similar to the recent advances in the computer industry which led to the development of less expensive computers. Information concerning the adverse effect of weather on EM propagation in this frequency band will allow the application of improved system design and link engineering techniques to eliminate or reduce the severity of this problem.

*The authors are with the Institute for Telecommunication Sciences, National Telecommunications and Information Administration, U. S. Department of Commerce, Boulder, CO 80303

Therefore, the purpose of this report is to describe the use of a millimeter wave diagnostic probe developed by ITS (Violette, et al., 1983) to measure and characterize degradation of the atmospheric channel due to weather.

For all radio applications of micro/millimeter waves, an understanding of the effects of the atmospheric medium is essential. Of concern to a user are any propagation effects that result in a change in the received signal amplitude or arrival time. The basic parameter of link performance is the signal-to-noise ratio (S/N). If the signal amplitude is reduced excessively, it may not be possible to extract the desired information or message from the signal because of system noise. Rain on a propagation path decreases the signal level of micro/millimeter waves and is one of the major degraders of communication system performance above 10 GHz. Factors that cause signal distortion are also of particular interest especially for wide bandwidths and digital systems. Objects mutually illuminated by the antenna of each terminal produce delayed signals or multipath signals by means of reflection, refraction, or diffraction that combine with the direct signal at the receiving antenna. If the delayed signals are of sufficient amplitude and delay, the received signal will be distorted, adversely affecting performance.

A variety of other mechanisms in addition to precipitation and path terrain affect the propagation of micro/millimeter waves. Micro/millimeter waves are absorbed in the atmosphere by the molecular spectral lines of the atmospheric constituents, oxygen and water vapor. The resulting attenuation is dependent upon radio frequency, atmospheric pressure, temperature, and the amount of water vapor in the air. Another important mechanism is the refractivity structure of the lower atmosphere. Atmospheric turbulence causes signal scintillation while more stable atmospheric conditions often develop layers that can result in atmospheric multipath, ray focusing (or defocusing), and angle-of-arrival variations.

The severity of most atmospheric effects on propagation increases with frequency in the micro/millimeter wave band. Because they are weather dependent, they are time variable and must be treated statistically. The statistical prediction of communication system performance depends on the climate and path geometry.

The prediction of channel performance and the effect of design options are the goals of the work being done by (ITS/NTIA). It is, of course, possible to design a micro/millimeter wave radio system that will have small outage times by selecting options to provide a sufficient fade margin. Distance between terminals, frequency, bandwidth, climate, antenna gain, and receiver noise-figure are some of the factors and tradeoffs to be considered in designing links to meet the performance requirement. Propagation performance models are still needed to allow the user to predict

whether requirements can be met with the available options and tradeoffs, and if so, at what expense compared with other means of establishing a communications link.

To assist in providing this information, ITS/NTIA has a program under way to develop models from existing theoretical information and experiments, to verify these models, and to provide statistical models through measured data. Much model development has already been accomplished by ITS in the areas of attenuation by gaseous absorption in the atmosphere (Liebe, 1981; Allen and Liebe, 1983), attenuation by hydrometeors (Dutton, 1977; Dutton, et al., 1982; Allen, 1983), and multipath fading (Crombie, 1983). This report, however, describes some of the effort toward obtaining measured data for model development and verification in the 10 to 100 GHz frequency band.

With the probe it is possible to identify the mechanisms responsible for particular fades (Allen et al., 1982) making it an extremely useful investigative tool. The probe would be especially effective for identifying the causes of fading on existing problem links. In addition the probe is very useful for characterizing the propagation-related signal degradations due to individual mechanisms and for testing prediction models.

Some of this type of work accomplished using the probe over paths in Colorado is described in this report. In Section 2 the probe itself is described. In Section 3 special attention is given to the 96.1-GHz link equipment recently added to the probe. The operation of the probe on several paths and observations and examples of the type of data available from the probe are given in Section 4. In Section 5 the data are used to characterize some fading mechanisms and performance statistics. In particular, in Section 5.1 the relation between the attenuation observed at 11.4 and 28.8 GHz due to rain is analyzed and compared to predictions based on popular raindrop-size distribution models. In Section 5.2 observations of clear air absorption at 96.1 GHz are compared to several models. Finally, the statistics of the bit-error-rate (BER) performance of the wideband digital biphase-shift-keying (BPSK) link of the probe are given in Section 5.3.

2. SYSTEM CAPABILITIES AND DESCRIPTION

The diagnostic probe designed to investigate propagation at millimeter wavelengths operates at 11.4, 28.8, 30.3, and 96.1 GHz. The 30.3-GHz channel is phase modulated at a 500 Mb/s rate. The 11.4, 28.8, and 96.1-GHz channels are unmodulated carriers. Received signal levels for all channels and BER information from the wide-band channel provide system performance data and diagnostic information on the propagation medium.

One of the features of the diagnostic probe is the ability to measure the impulse response of the channel. This is accomplished by the phase modulation of the 30.3-GHz carrier with a pseudorandom binary sequence. The 30.3-GHz signal is transmitted through the channel to a receiver where the signal is demodulated to reproduce the 500 Mb/s pseudorandom sequence degraded by any distortion that may have occurred in the propagation between transmitter and receiver. At the receiver terminal, a replica of the transmitted binary sequence is generated. A cross-correlation is performed between the received demodulated bit stream and the replica of the transmitted bit stream by allowing one bit stream to slide by the other in time as a result of a slight offset in the bit-clock frequencies. At the time when the bit sequences are identically aligned, an impulse is generated with a base duration equal to two bit durations. The impulse response measurement repeats at a rate corresponding to the number of bits in the sequence or word divided by the clock offset rate. Channel amplitude and phase dispersion during propagation of the signal appear as changes in the impulse shape. A channel is completely described by the channel impulse response or its Fourier transform, the transfer function of the channel. Thus, the diagnostic probe is a means of acquiring data to determine parameters in modeling channel characteristics and predicting performance for specific applications.

The received bit stream can be routed for processing by matched filters and decision-making circuitry to estimate the binary states of the received data stream. With knowledge of the transmitted word, a count of the occurrence of errors can be recorded. This permits a performance measure of a channel in terms of bit error rate (BER) which can be compared to channel characteristics as seen by the impulse probe.

Amplitude response information across the channel bandwidth is desirable to provide a complete diagnosis of a channel and improve measurement accuracy. The high data rate of 500 Mb/s and the relatively long pseudorandom word lengths (2^7 or 2^{15} bits) provide a wide bandwidth (1 GHz) with closely spaced spectrum lines (4 MHz or 15 kHz correspondingly), so that amplitude distortion of a channel can be

viewed with high resolution. This is particularly useful for channels containing multipath signals that produce selective fades. An amplitude response display across the bandwidth shows the relative location of fade nulls that are not as easily obtained from the impulse probe and this feature is important in analyzing short-term (millisecond to seconds) link performances.

The carrier wave (cw) probes at 11.4, 28.8, and 96.1 GHz are coherent, i.e., all signals, rf carriers, modulation signals, and data clocks, are derived from a single stable reference oscillator either directly or by phase-locking techniques. Phase coherence in the diagnostic system allows frequency-dependent propagation mechanisms to be isolated.

2.1 Description of the Probe

Transmitter Terminal

Figure 2.1 shows a block diagram of the transmitter terminal of the probe, contained in two enclosures. One houses the hardware that generates the rf signals fed to the antennas and the other houses the baseband data generators and modulators to provide the 1.5-GHz modulated subcarrier. To avoid problems with beat frequency components and relative phase shifts, all signals are derived from a single temperature compensated crystal oscillator (TCXO). All active multipliers are phase locked and those with outputs at microwave frequencies are cavity tuned to reduce the noise bandwidth. The blocks shown in Figure 2.1 with the heavy line at the base indicate those units with active components.

The Gunn effect source is injection-locked through a circulator and supplies an output of 150 mW at 28.8 GHz for the upconverter local oscillator and the cw probe output. With 10 mW of subcarrier at 1.5 GHz, the upconverter generates a 30.3 GHz carrier with modulation at 1 mW of upper sideband (USB) power after the low-pass reject filter. A flat (± 2 dB) bandwidth of 2 GHz has been achieved with the balanced mixer and computer-designed etched waveguide filter, which is a key element in generating a sum of the input signals with the low distortion necessary to maintain a high resolution probe. Another critical element is in the design of a K_a -band power amplifier. The 1 mW is increased to 100 mW with a high degree of amplitude flatness and phase linearity across the 29 to 31-GHz portion of the 26 to 38-GHz response range of the power amplifier. The power rating of this amplifier increased the useful range of the wide-band probe to at least 50 km. The antennas used on the 30.3-GHz link are 3-ft parabolic reflectors (0.75° beamwidth) with feeds that provide dual linear polarization. Isolation between orthogonal linear modes is specified to be better than 38 dB, allowing depolarization measurements for many path conditions.

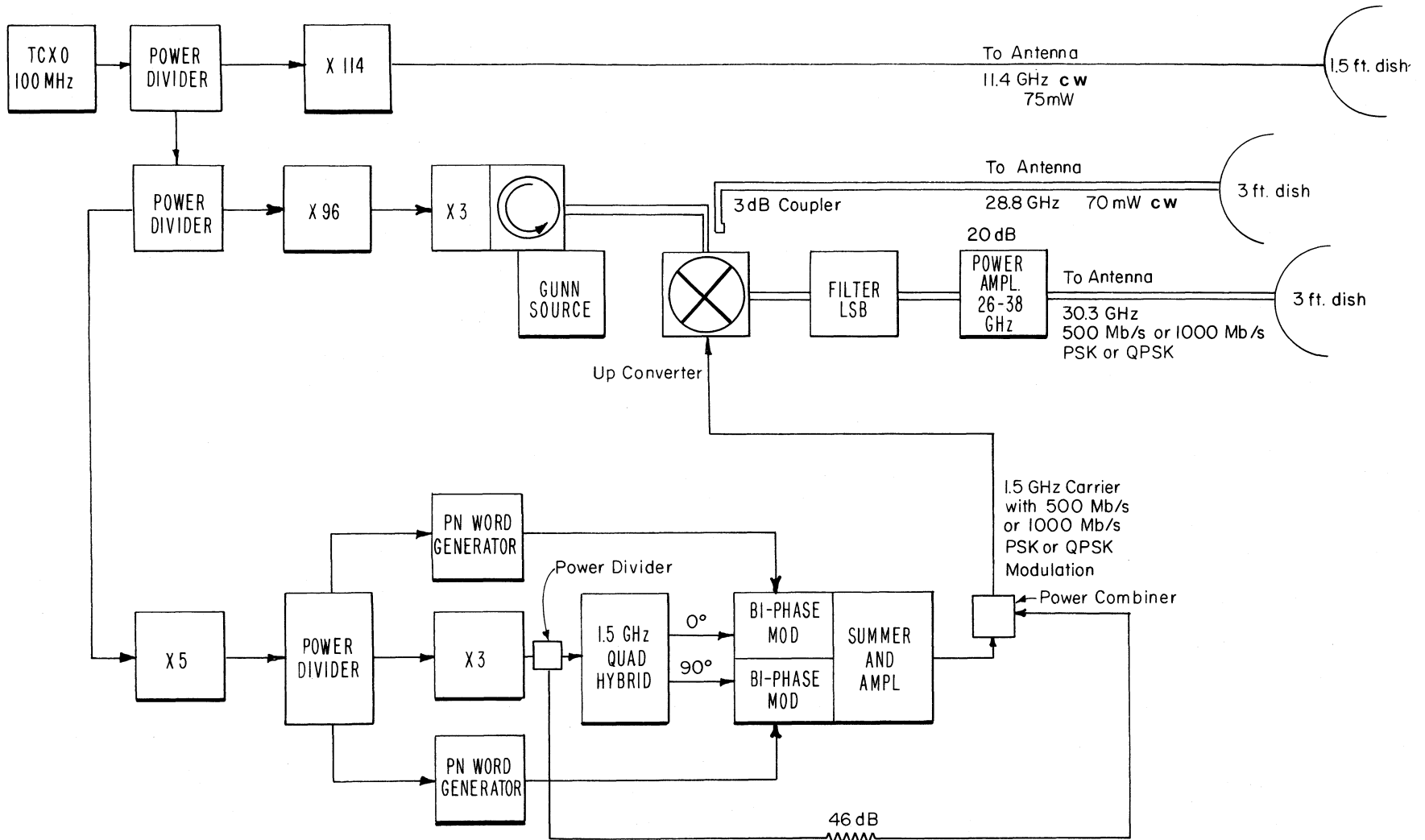


Figure 2.1. Block diagram of the transmitter terminal.

The baseband digital generators are capable of producing a pseudorandom data stream at rates from 200 to 1000 Mb/s. Because of matched filters and decision circuitry at the demodulator, a fixed data rate is required. For all BER diagnostic applications a rate of 500 Mb/s was used. Pseudorandom code lengths or word lengths of either 2^7-1 (127 bits) or $2^{15}-1$ (32,767 bits) can be selected. One or both data streams from the word generator can be applied to quadrature components of the 1.5 GHz subcarrier, summed, and amplified to provide 10 mW of drive to the upconverter.

Receiver rf Portion

A block diagram of the rf portion of the receiver is shown in Figure 2.2. The first-stage downconverter and integrated preamplifier is a balanced mixer, using strip-guide design, direct coupled to a low-noise linear amplifier with a 3 dB noise figure. This combination has a single sideband effective noise figure of less than 8 dB with 24 dB (± 1 dB) gain and ± 7 degrees phase linearity over a 1.5-GHz bandwidth. Generation of the local oscillator signal is from a 100-MHz voltage-controlled crystal oscillator (VCXO), a times-96, phase-locked, cavity-tuned multiplier, and a passive harmonic tripler, all selected for their low phase noise. All received IF signals are phase locked to the transmitted signal by controlling a 100 MHz VCXO which is used to generate the local oscillator (LO) reference for each rf downconverter. The purpose of the cw probes is to isolate frequency-dependent parameters of the transmission channel. As indicated in Figure 2.2, dual antennas are employed with the cw probes (a wide beamwidth and a narrow beamwidth) in order to isolate angle of arrival or beam decoupling fades from other sources of fades. Also, the two-beam link enables some determination to be made on direction and type of multipath present, especially those associated with paths generated by refractive bending of rays. When the narrow-beam antenna is pointed for ground clearance and no fading is seen, but the wide-beam channel shows fading, then ground multipath signals are assumed. If both beams show fading characteristic of multipath, then atmospheric multipath is assumed.

Demodulator S/N Performance Tester

Figure 2.3 is a block diagram of the demodulator portion of the wide-band probe. It consists of a S/N performance tester that primarily allows white noise to be mixed with the modulated 1.5-GHz input signal or at baseband frequencies to calibrate the BER in terms of the ratio of bit energy to noise energy (E_b/N_0) for either of the bands in question.

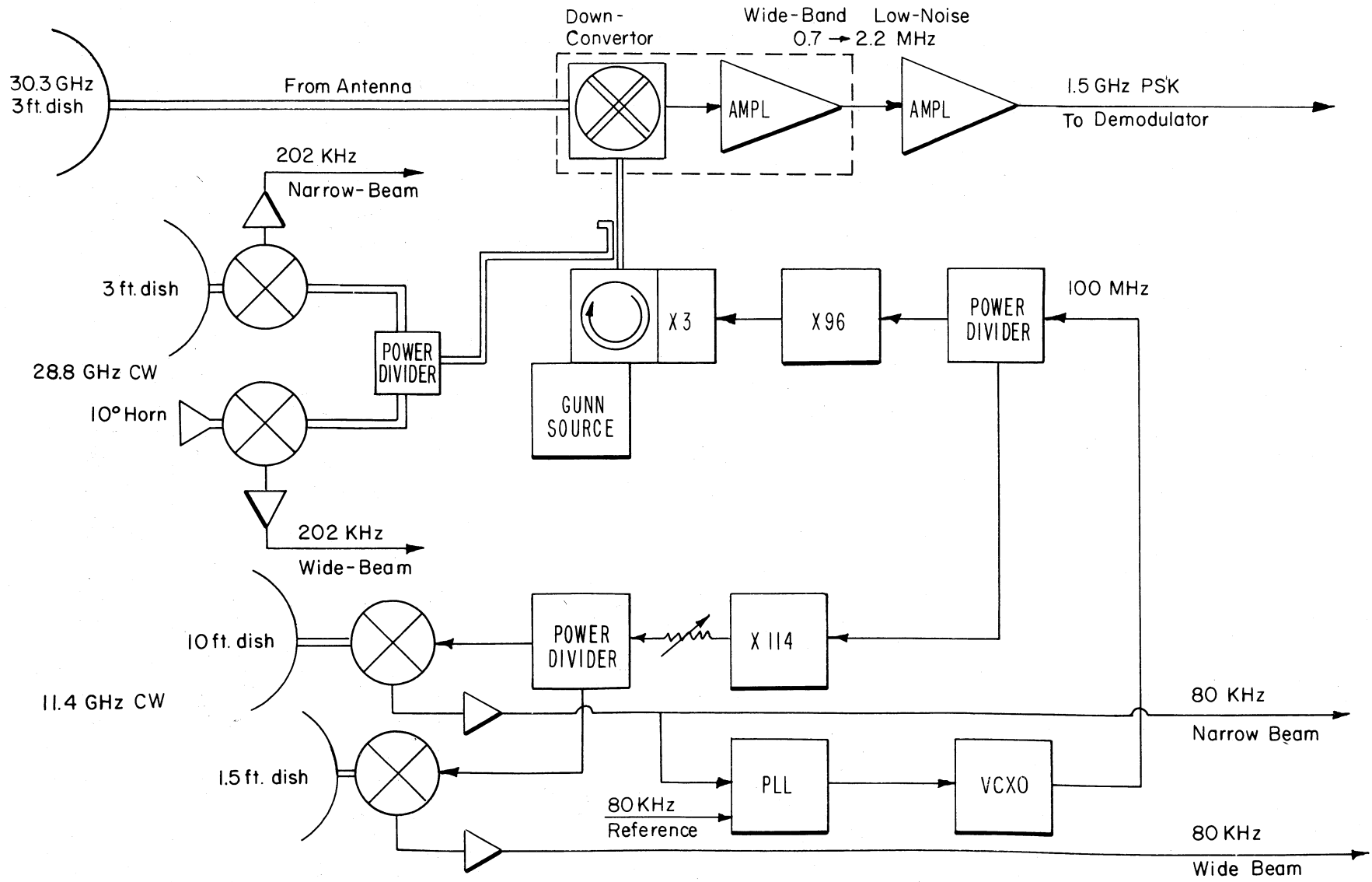


Figure 2.2. Block diagram of the rf section of the receiver terminal.

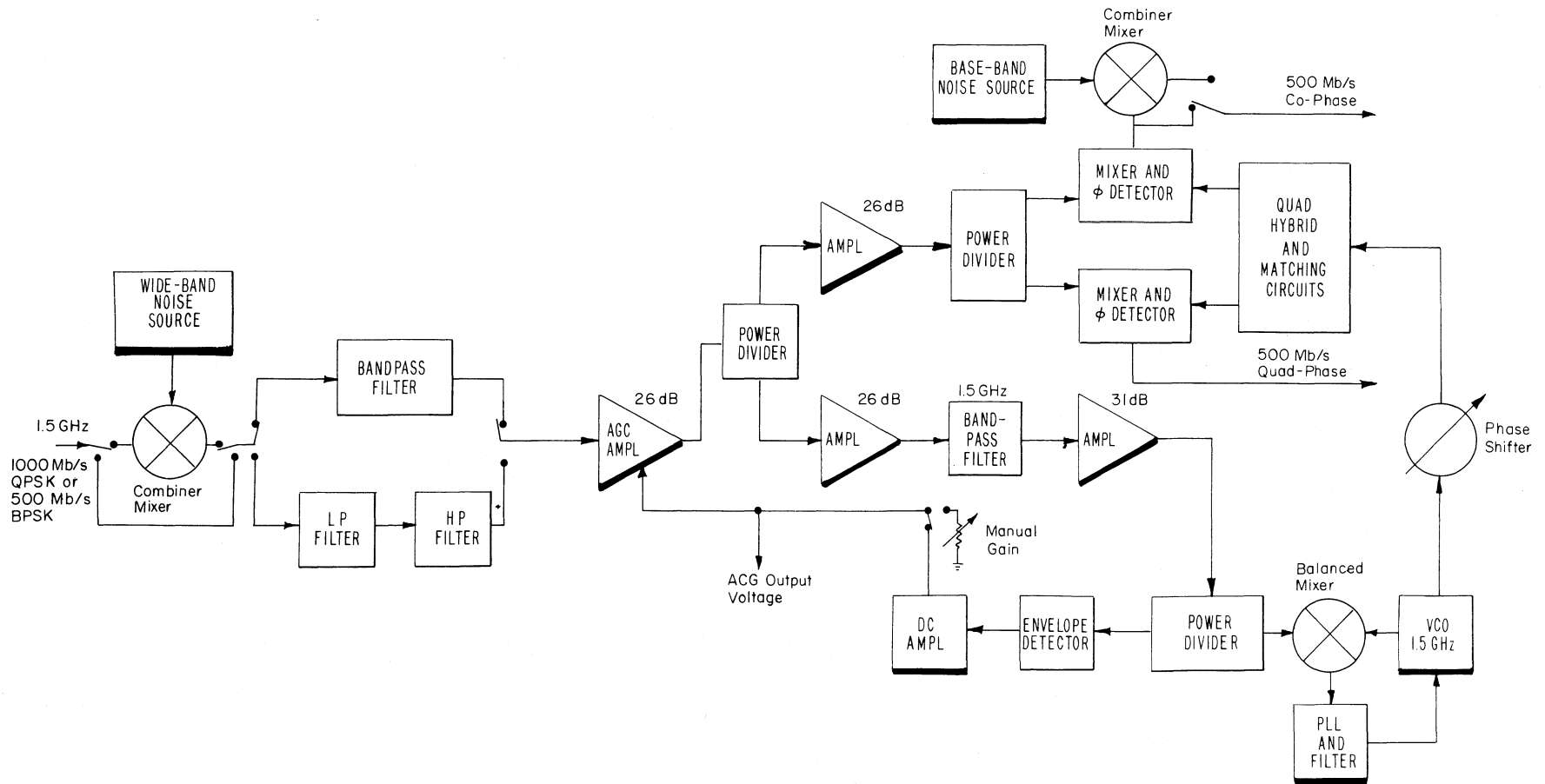


Figure 2.3. Block diagram of the receiver demodulator.

The 1.5-GHz modulated carrier is filtered, amplified by the 24 dB gain-controlled circuit, and then divided. The upper branch is again amplified, divided, and fed into the baseband mixer-detectors to provide a cophase and a quadphase channel. When measuring the channel impulse response, a BPSK transmission is used to permit a sum of the squares operation at the cophase and quadphase channels to accurately measure the amplitude for all phase combinations of the incoming signals.

The lower branch of the modulated 1.5 GHz signal is likewise amplified and divided for use in the carrier reconstruction and automatic gain control (AGC) circuitry. Carrier reconstruction is accomplished by inserting a small subcarrier signal (30 dB below the total power in band) at the modulator to serve as a source to phase lock a voltage controlled oscillator (VCO). A narrow-band, phase-tracking loop greatly improves the signal-to-noise ratio (S/N) resulting in a lower BER than would be achieved without the inserted subcarrier. The output of the VCO is passed through a phase shifter then split into quadrature phase components to properly regenerate the baseband data stream at the mixer phase-detector. To insure a proper inphase and quadphase relationship of the 1.5-GHz VCO reference relative to the modulated signal phase at the detector, the AGC circuit adjusts the amplifier gain for a constant output from the first demodulator amplifier. A constant phase is held by this AGC action over a 20-dB range of received signal level. Programmable attenuators are used at the demodulator input to extend the range of the input signal level (with constant phase to the detector) beyond the 20-dB range of the AGC amplifier. One of the diagnostic parameters is the AGC voltage, calibrated to give a dBm level for the received signal. The AGC voltage indicates signal plus noise power over a \pm 350-MHz bandwidth centered at 1.5 GHz.

Bit Synchronizer and Signal Conditioner

Functional diagrams of the bit synchronizer and signal conditioner and bit error detector circuitry are shown in Figure 2.4. A discussion of the techniques used is contained in Gray (1969) and Gray (1972).

Bit Error Detector

A functional diagram of the bit error detector is included in Figure 2.4. The unit used for this purpose is a wide-band digital receiver with an input range of from 200 to 1000 Mb/s. Internally, the data estimate is shaped and demultiplexed to 1/4 rate to allow compatibility with commercially-available, high-speed emitter-coupled-logic integrated circuits. An error detector module processes the demultiplexed signals and does a parallel bit-by-bit comparison between the locally

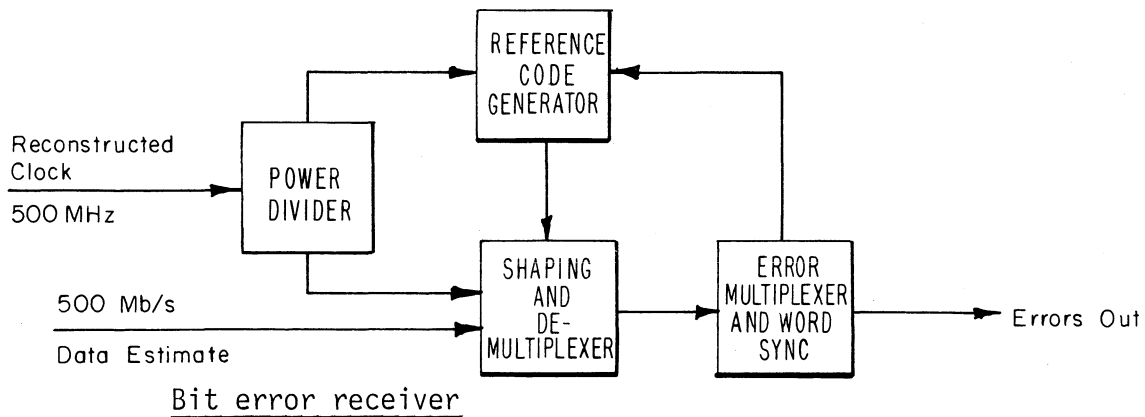
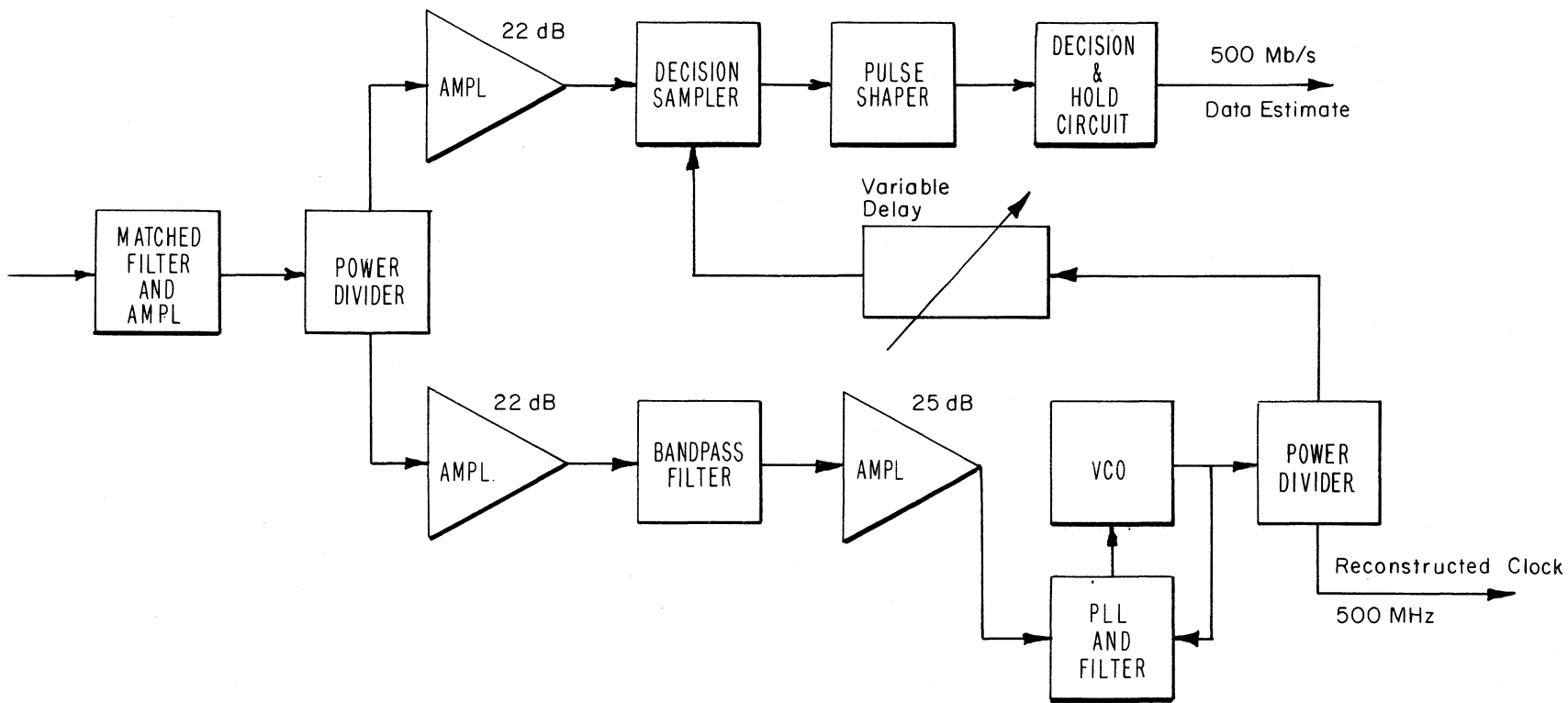


Figure 2.4. Block diagram of the bit synchronizer, signal conditioner, and bit error receiver.

generated 4-phase signal and the 4-phase signal derived from the input signal. Automatic synchronization occurs by counting successive zeros in the data stream and latching the internal bit clock when this number reaches $n-1$, where n is the number of stages in the data generator shift register. Synchronization acquisition is assumed if there are fewer than 30,000 errors in an 80,000-bit frame of received data. This also describes the maximum error-burst detectable, and a greater number of errors within a frame defines an out-of-sync condition. The error output is fed to a gated counter that is sampled by the data logging computer at a 1-s interval establishing the minimum detectable error rate for one second of 2×10^{-8} . An ungated counter is used as a totalizer to accumulate errors over longer periods of time to measure lower BER.

Impulse Response Cross-Correlator

The impulse response mode can be programmed automatically if a preset data threshold is exceeded or by manual command. A functional diagram of the cross-correlator for the impulse mode is shown in Figure 2.5. The correlator best suited to the purpose is an extended frequency range (1 to 1000 MHz) double-balanced mixer. Since a positive or negative level occurs at the mixer output depending on the phase of the received signal, a cophase and quadphase data stream is generated in the demodulator so that the sum of the squares operation can be performed to obtain the proper magnitude of the impulse response curve (the power impulse function). Each correlator is driven as a local oscillator by a 2^n bit word generator that creates a replica of the signal transmitted. An offset frequency clocks the replica generator a few hertz (rate depends on word length 2^7-1 or $2^{15}-1$) slower than the transmitted bit clock, so that in roughly a 1-s period, all bits in the replica word slide by the received word. When all the ones and zeros within the two words coincide, a triangular impulse voltage waveform occurs with a normalized maximum peak to base amplitude ratio equal to 2^n-1 providing a maximum dynamic range of about 42 dB for the 2^7-1 word length and 90 dB for the $2^{15}-1$ word length. Because a 3-1/2 digit voltmeter was the best available for the high sampling rate required, the dynamic range of the measurement is restricted to 30 dB. This minimum recordable voltage level falls above the noise threshold of the 30.3-GHz, 500 Mb/s probe until the receiver input level is less than about -76 dBm. As shown in an earlier report (Violette et al., 1983), a multipath signal 30 dB below the direct signal level produces very little degradation of the channel. In fact, voltage standing waves at waveguide or coaxial connections are visible in the impulse response curves.

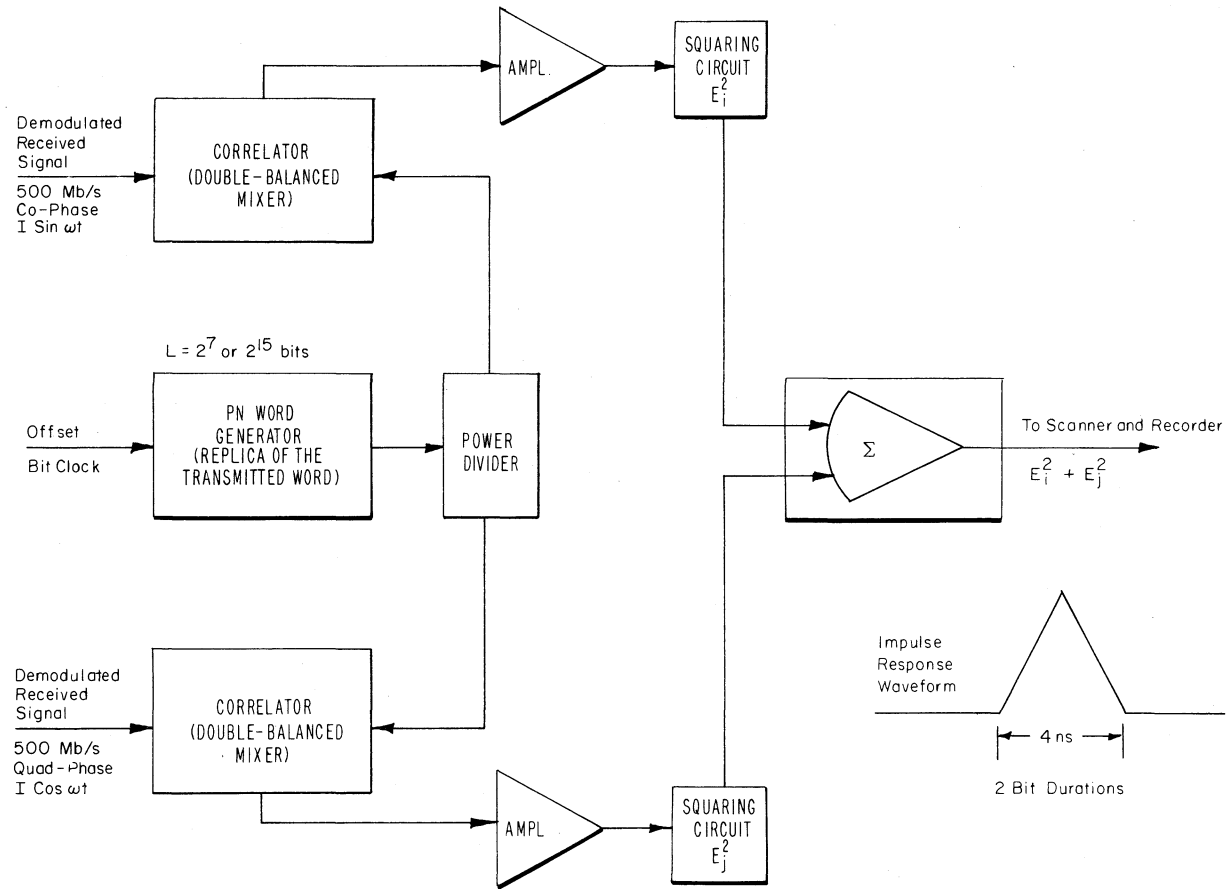


Figure 2.5. Block diagram of the impulse response cross-correlator.

In the ideal case, the base width of the impulse response curve is 2 bits in duration (4 ns) but the actual record time for this base width is approximately 15.75 ms ($\frac{2 \text{ bits}}{127 \text{ bits}} \times 1 \text{ s}$) at a clock offset rate providing an impulse repetition period of 1 per second for the 127-bit word length. This 15.75-ms interval is normally small compared to atmospherically-induced changes. Since all circuits used in the correlation process are not perfectly linear, the hardware produces some distortion in the impulse measurements and for this probe an increase in the base width to about 5 ns occurred. The impulse curve generated by the hardware only becomes the reference to compare channel distortion resulting from an atmospheric path. Any circuit or channel distortion occurring within the impulse time period affects the shape of the impulse. However, any time delayed signal (multipath signal) greater than the 1 bit-clock period shows as a separate delayed impulse with an amplitude that is a function of its contribution to the total received rf power. Examples of these impulse waveforms are shown in Section 4 of this report.

2.2 Meteorological Instrumentation

A meteorological instrumentation package was installed at the receiver terminal of the 27.2-km path. This package includes a microwave refractometer (9.375 GHz) which provides a direct reading of N (refractivity of the atmosphere.) Ambient air and cavity temperatures and barometric pressure are also available for recording. From these parameters, water vapor pressure and relative humidity are calculated. A Belfort capacitive-bridge rain-rate gauge provides rainrate in millimeter per hour. A brief description of these instruments and conversion formulas is given below.

The refractometer sensor package includes a microwave cavity, two solid-state temperature probes for measuring cavity and ambient air temperature, and a solid-state pressure transducer for measuring atmospheric pressure. The temperature and pressure probes have been calibrated to be accurate to 0.5 deg Celsius and one millibar, respectively. The microwave cavity has been calibrated with temperature in an evacuated bell jar to determine a correction curve for the changes in resonant frequency. When corrected for temperature, the cavity measure of atmospheric refractivity is accurate to less than 0.5 N units. The refractometer sensors are packaged in a meteorological enclosure with louvered sides mounted in the vicinity of the receiving antennas. A fan circulates air over the atmospheric temperature probe and around and through the microwave cavity. In this configuration the response time of the cavity and pressure transducer is less than

1 s. The response time of the atmospheric temperature probe is less than 1 min. Data from the sensors are available once per second.

Refractivity N (Smith and Weintraub, 1953) in N-units is defined as

$$N = \frac{77.6P}{T} + \frac{3.73 \times 10^5 e}{T^2} \quad (2.1)$$

where

P = barometric pressure, millibars

T = absolute temperature, °K

e = partial pressure of water vapor, millibars

With the above-stated accuracy in measured atmospheric refractivity, temperature, and pressure, the partial water vapor pressures can be determined to within 0.3 millibars.

The Belfast remote sensing instrument translates instantaneous rate of rainfall into a dc voltage level. A 12-in diameter collector funnels the flow between electrodes of a capacitor that forms one leg of an rf bridge. Changes in capacitance unbalances the bridge proportional to the amount of water present in the capacitor. The bridge output is fed into a difference amplifier and the output voltage is directly proportional to rate of rainfall. A heating element is wrapped around the funnel area to melt snow and prevent icing at the capacitor channel.

A calibration of voltage versus rain rate was accomplished by using an accurately-controlled flow rate meter. Rates of 1 to 200 mm per hour were adjusted on the flow meter and the resulting voltage curve was stored in the computer for translation into rain rates. For this calibration a flow rate of 1 cc/min is equivalent to a 0.822 mm/hr rain rate. To obtain reliable readings down to a 1 or 2 mm/hr rate, the capacitor was modified to prevent bunching of droplets within the channel.

2.3 Computer-Controlled Data Acquisition and Recording Equipment

All data logging and recording operations are controlled by a desk-top computer. Functions controlled by the computer are shown in Figure 2.6. Input signals are sampled by a scanner and read by a high speed 3-1/2-digit voltmeter (4000 readings per second) for processing in the computer. Parameters of the rf channels such as amplitude of the 11.4, 28.8, 30.3, and 96.1-GHz carriers can be sampled at up to a 0.1-s rate. Also, channel impulse response measurements can

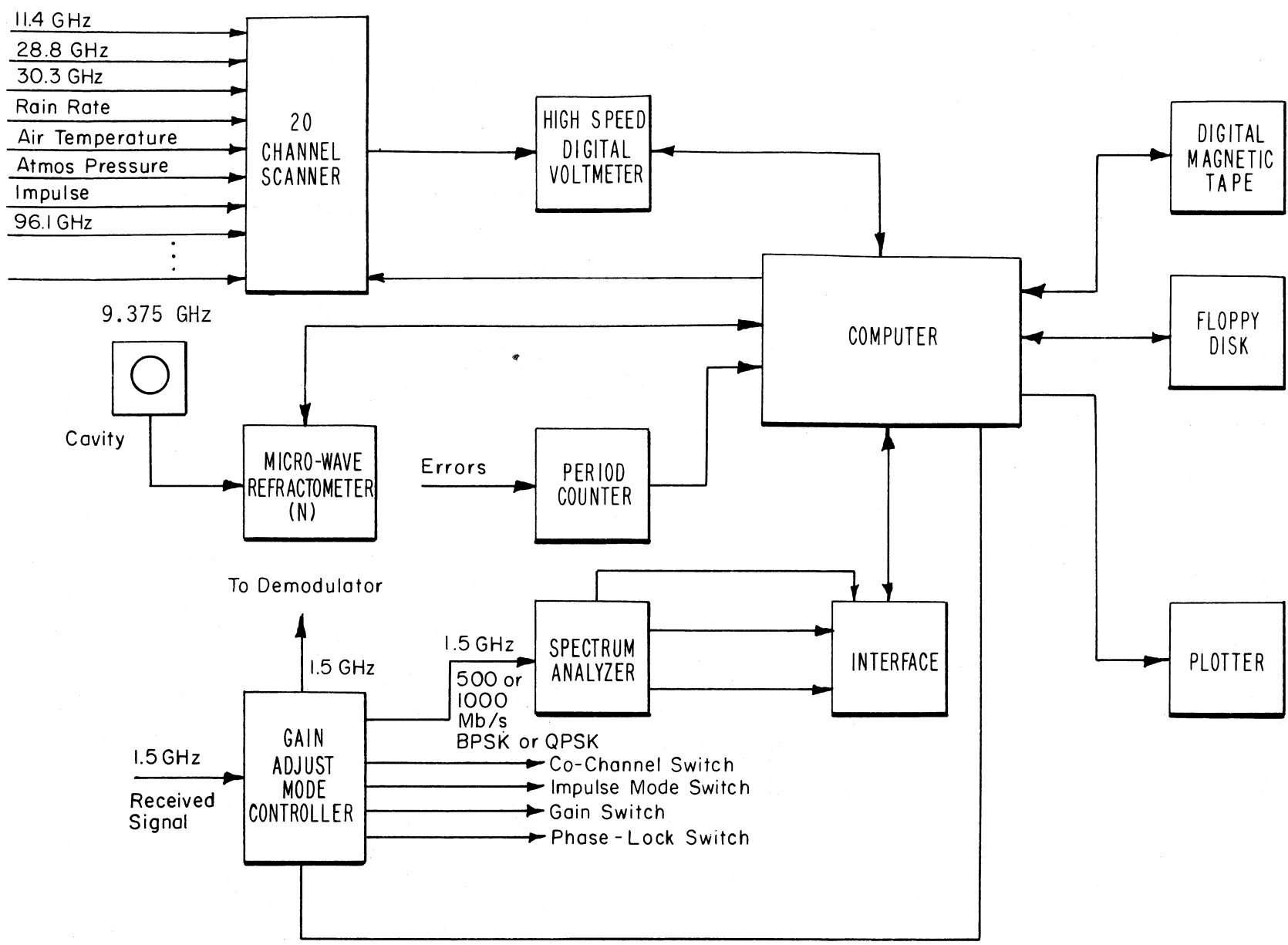


Figure 2.6. Diagram of the data acquisition and recording equipment.

be completed and recorded at 2-s intervals. Meteorological data, which includes air temperature, pressure, and rain rate are generally sampled at the same rate as the rf amplitudes. A cavity-type microwave refractometer supplies the computer with N values of $\pm 0.1 N$ resolution each second or $\pm 1.0 N$ resolution in a 0.1 s sampling period. At a 1-s gate-time, a period counter reads BER down to 2×10^{-8} .

Computer programs are fed from either the magnetic tape or floppy disk and each also serves to store the data. Data can be retrieved, processed, and displayed on the plotter connected to the system. Several kinds of software are available for the computer including ray tracing from refractive index profiles to predict channel performance. The basic logging programs monitor the channel signal amplitudes, BER, and meteorological data until the BER exceeds a preset threshold (such as 10^{-6}). When it is not raining at the receiving terminal and this threshold is exceeded, it is assumed that channel distortion is present and the impulse response and amplitude scans are programmed.

3. DEVELOPMENT AND CALIBRATION OF THE 96.1-GHZ CHANNEL

A phase-lockable source at 96.1 GHz and a downconverter (balanced mixer) pre-amplifier with a phase-lockable local oscillator source were procured. These devices were assembled with the components required to integrate the 96.1-GHz channel into the existing coherent multichannel system (diagnostic probe) described in Section 2. Figure 3.1 contains a block diagram of the circuits housed at the transmitter terminal. A phase-locked IMPATT oscillator provides 28 mW of power to a linearly-polarized 10-in parabolic antenna. All signals--timing, data clocks, IF and rf sources of the diagnostic probe--are derived from a single temperature compensated crystal oscillator (TCXO). The output of this 100-MHz TCXO is multiplied to 96 GHz by successive phase-locked stages for comparison to the output of the IMPATT oscillators through an rf balanced mixer. Phase-lock electronics generate an error signal that is added to the dc bias voltage supplied to the IMPATT. If the IMPATT is not in a locked state, a voltage sweep is triggered and added to the dc bias supply until the IMPATT frequency is the same as the multiplied TCXO signal at which time the error signal takes control to hold the IMPATT in lock.

A block diagram of the 96.1-GHz receiving terminal is shown in Figure 3.2. A Gunn oscillator is used as the local oscillator (LO) source in place of an IMPATT because of superior noise performance that relates to the overall noise figure of the receiver. One important goal was to provide a state-of-the-art noise figure in the first stage of the receiver (mixer-preamplifier). Low-loss conducting surfaces, physical mounting, and matching of the mixer diodes, as well as LO spectra purity

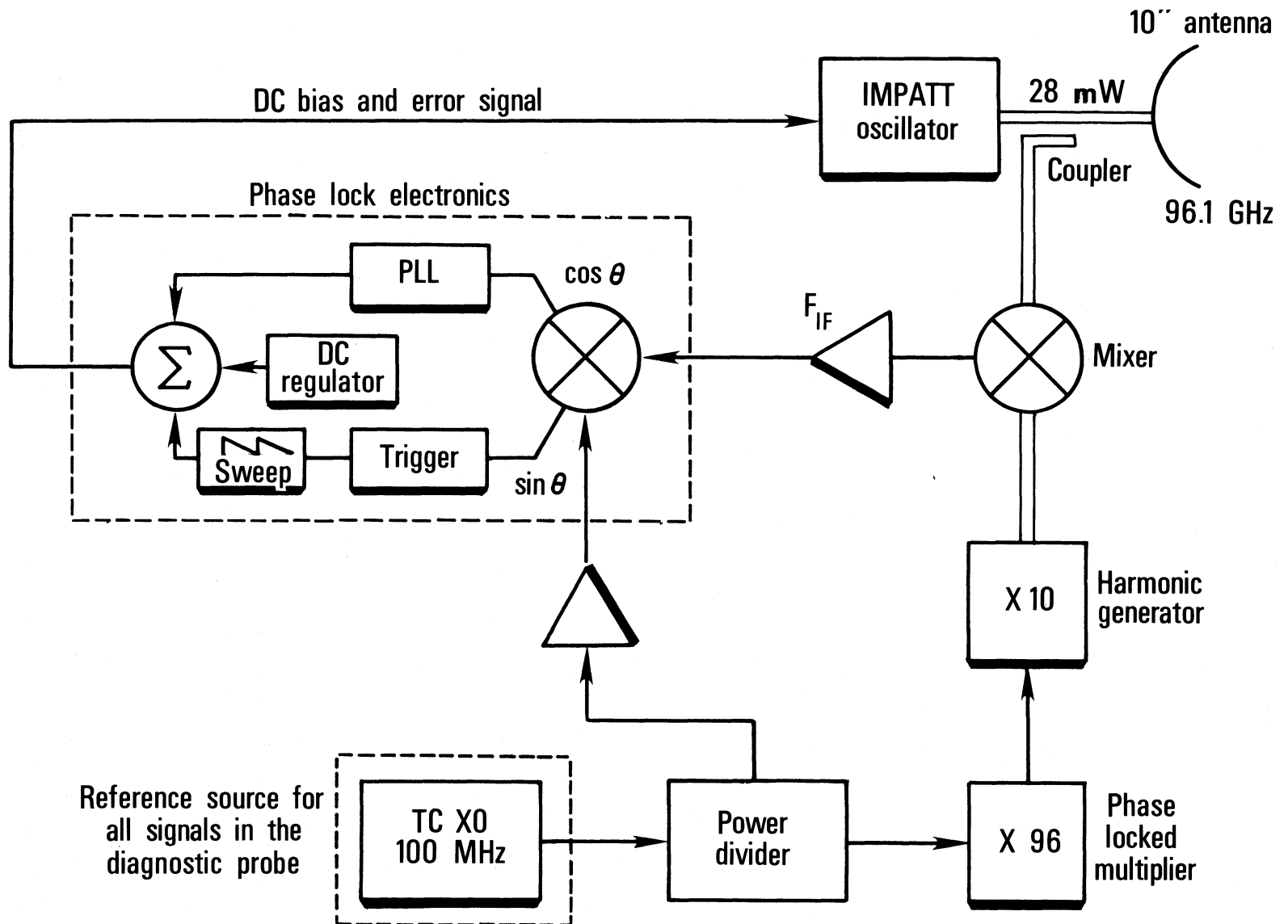


Figure 3.1. Block diagram of the 96.1-GHz transmitter.

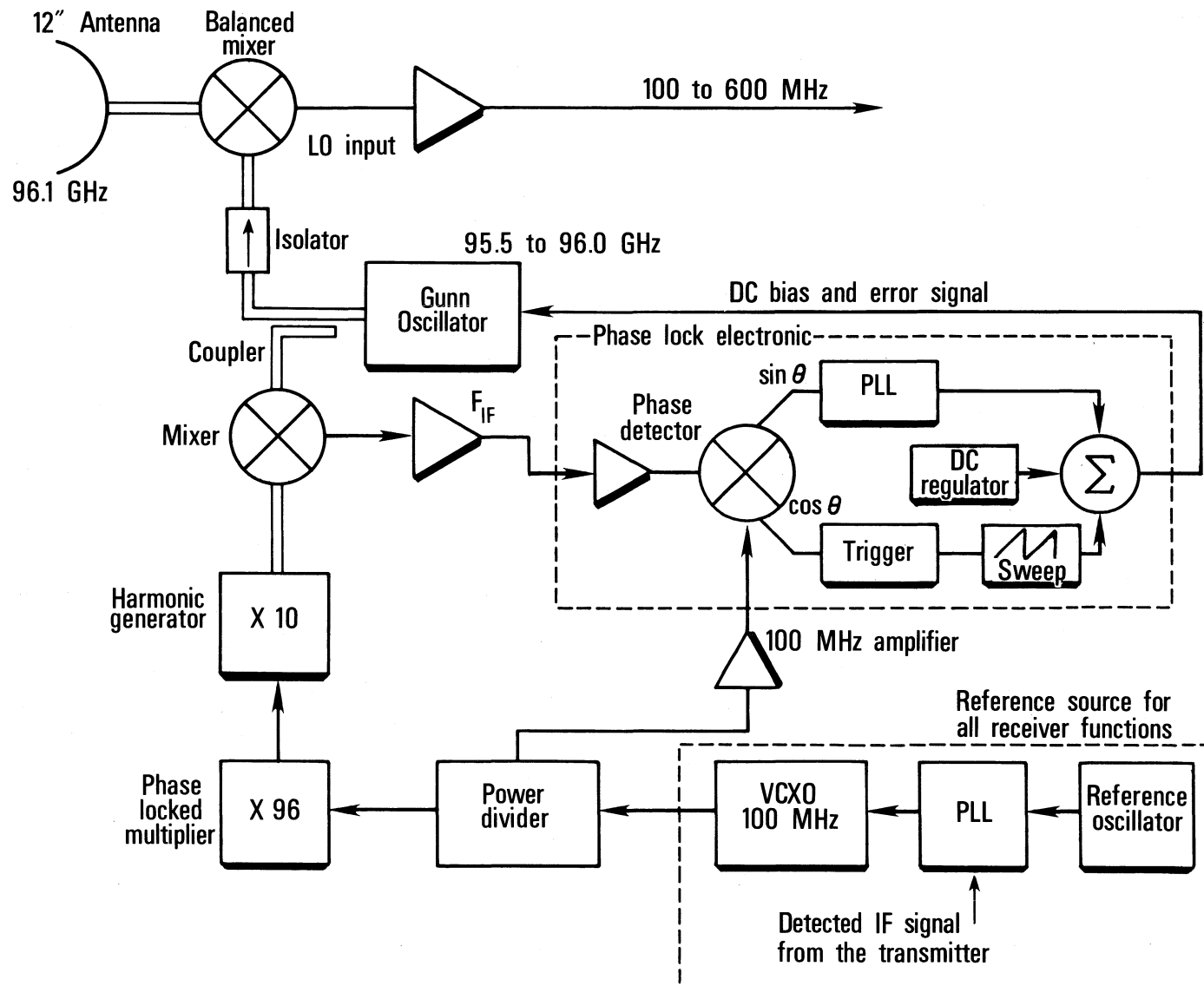


Figure 3.2. Block diagram of the 96.1-GHz receiver rf stage and local oscillator source generator.

and the technique used to apply the pump signal, are critical in the design of a unit with a low noise figure. Effective coupling to the IF input of a wide-band low-noise preamplifier also contributes to the achievable overall noise figure. Because of the higher gaseous absorption on an atmospheric path and especially the higher rain attenuation, a low-noise floor is necessary for the 96-GHz channel to operate at path lengths commensurate with the lower rf frequencies used in the probe.

The received signals are coherently detected as a result of phase locking the voltage controlled crystal oscillator (VCXO) frequency to the IF signal of the lowest transmitted probe frequency (11.4 GHz). As in the transmitter, all timing, data clocks, IF and rf sources are derived from a single reference, a VCXO that is phase locked to the TCXO of the transmitter terminal. Frequency multipliers to phase-lock the Gunn sources use electronics similar to that used in the transmitter to lock the IMPATT. The Gunn will lock over a frequency range of 96.0 to 95.5 GHz which translates to an IF center frequency range of 100 to 600 MHz. If an IF of 500 MHz is selected, an instantaneous bandwidth through the mixer-preamplifier of about 1000 MHz is available. However, normal probe operation with the 96.1-GHz channel is for the LO (Gunn) to be locked at an IF of 242.15 MHz, a number that results from the phase-lock electronics being set to provide twice the 100-MHz reference signal plus the IF of the lowest transmitted frequency channel (11.4 GHz at 5 MHz IF) times the ratio of 96.1/11.4. A 6.2% IF passband filter is used now, but a 0.4% passband filter is on order that will provide an additional fade margin of 12 dB.

Calibration of the 96.1-GHz channel included measuring the output power with a waveguide thermistor referenced to the NBS 6-port network analyzer and a micro calorimeter. With this capability the power delivered to the antenna was found to be 27.7 mW. All waveguide-type attenuators used in the link calibrations were also measured in this manner providing a ± 0.1 dB accuracy.

Once these calibrations were accomplished, the transmitter and receiver were again coupled by waveguide attenuators, and the measured and calculated output signal levels then agreed to the resolution of the measuring equipment (± 0.05 dB). This agreement confirmed the receiver front-end rf/IF gain of 33.5 dB. The conversion loss of the mixer is found to be 6.5 dB, the difference between the IF amplifier gain at 242 MHz (40 dB) and the IF-rf gain of 33.5 dB.

This information permits determination of signal-to-noise ratios for any path length for which received power can be calculated, provided the signal substantially exceeds the ambient noise power at the antenna. The receiver noise power measured

with a 242-MHz IF and 6.2% bandpass filter was -97.75 dBm at the IF output port of the mixer with the rf port terminated. With a recently acquired 0.4% bandpass filter the receiver noise power will be -109.6 dBm, not including antenna noise.

An equation for calculating the receiver noise power (P_n) is

$$P_n = 10 \log k (F-1) T_o B \quad (3.1)$$

where

k = Boltzmann's constant = 1.38×10^{-23} joule/deg

F = power ratio of noise figure taken from F_{dB} (receiver noise figure)

T_o = temperature of device in degree Kelvin (293°)

B = noise bandwidth in Hz (15×10^6)

The manufacturer reported a measured mixer-preamplifier noise figure (F_{dB_1}) of 4.3 dB at an IF of 250 MHz. Using this value (4.3 dB) and a mixer temperature of $293^\circ K$, the calculated receiver noise power is -99.87 dBm. This is a valid calculation since we know that if the gain of the first network of a receiver is large, then for all intents and purposes, F_{dB} is equal to the noise figure of the receiver first stage (F_{dB_1}) (Skolnik 1962).

The difference of about 2.1 dB between the calculated P_n using the manufacturer's data for (F_{dB_1}) and the measured value seemed too large. In an attempt to explain the difference, the noise figure of the mixer-preamplifier was remeasured. The procedure used for the mixer-preamplifier noise figure (F_{dB_1}) measurement is described by Wait (1973) and resulted in a value of 5.55 dB. Using this value F_{dB_1} , $P_n = -98.04$ dBm, resulting in a difference of only 0.29 dB compared to the measured value of -97.75 dBm. In this procedure, a hot source and cold source are sequentially connected to the input of the device under test and the ratio of the noise power output is measured. The hot source used in this measurement was an NBS reference which is the only such device calibrated in this frequency range.

A noise figure of 5.55 dB for a mixer-preamplifier at 96 GHz is a commendable accomplishment but an important point to note is that state-of-the-art precision measurement instrumentation has not yet extended to this portion of the spectrum at the hardware design level. The fact that the measurements of receiver noise power and the noise power determined from the measured noise figure agreed to within 0.3 dB may have been a coincidence but it will be interesting to perform additional checks of accuracy without the use of a calibrated noise source.

With this information, the received minimum detectable threshold can be obtained if the receiver terminal rf line loss and antenna noise temperature are known. Line loss is essentially a function of the waveguide attenuation between

the antenna and the mixer rf port. A 12-in parabolic antenna with a prime-focus feed that requires a 15-in length of waveguide was used at the receiver. Each inch of non-oxidized silver plated guide (WR-12) has an attenuation of 0.052 dB for a total rf loss (L_{rf}) of 0.62 dB. This excessive loss has a small effect on minimum detectable signal level, however, it will be improved when a cassegrain antenna is obtained.

Based on CCIR Report 720 (CCIR, 1978a), the effective clear air noise temperature (T_a) at 96 GHz for a narrow antenna beam at a 0-deg elevation angle is approximately 290°K. This temperature indicates a nearly-totally absorbing medium but some noise temperature is due to ground illumination of the main beam and side lobes. At lower frequencies or higher elevation angles noise temperatures below 290°K occur.

The total effective received noise temperature (T_{re}) can be calculated from

$$T_{re} = T_a + (L_{rf} - 1)T_a + T_e L_{rf} \quad (3.2)$$

where

T_a = the effective clear air noise temperature

T_e = the mixer noise temperature

L_{rf} = the rf line loss.

Substituting in (3.2), 290°K for T_a , 0.62 dB for L_{rf} , and 758°K for T_e , T_{re} was calculated to be 1209.4°K. Knowing T_{re} , the minimum detectable threshold level (P_d) can be determined from

$$P_d(\text{dBm}) = 10 \log k + 10 \log T_{re} + 10 \log B + 30 \quad (3.3)$$

where

k = Boltzmann's constant (1.38×10^{-23} joule/deg)

T_{re} = total effective received noise temperature

B = receiver bandwidth

From (3.3), using $T_{re} = 1209.4^\circ\text{K}$ and $B = 15$ MHz, the minimum detectable threshold level (P_d) is -96.0 dBm. With a cassegrain antenna and a 0.4% bandpass filter, P_d would be decreased to -108.0 dBm, the minimum detectable threshold level of the 96.1-GHz channel in its intended final hardware configuration.

Before the 96.1-GHz channel was installed on the 27.2-km line-of-sight diagnostic path, it was calibrated on a 105-m path. The minimum far field distance of $2D^2/\lambda$, where D is the antenna aperture and λ the rf wavelength, is 56.3 m for the 12-in reflectors. The plan for obtaining the absolute path loss was to measure the difference in signal loss between the 105-m calibration path and the

27.2-km diagnostic path with the highest accuracy the instrumentation permits. On the calibration path, only the free-space loss was used to calculate the received power because the gaseous absorption loss (≈ 0.03 dB) is well below the noise of the measurement accuracy. By inserting attenuation between the transmitter source and antenna that approximates the path loss difference (loss at 27.2 km - loss at 105 m), errors due to nonlinearity would be greatly reduced or eliminated. Two attenuators (nominally 30 dB) were inserted between the transmitter output and the antenna for the 105-m calibration path. Before these pads were used, they were measured on the NBS 6-port network analyzer resulting in individual values at 96 GHz of 32.16 and 26.14 dB (58.3 dB total). The additional loss of a 27.2-km path, compared to the 105-m calibration path was estimated at 56.4 dB. The calculated free-space path loss is 48.2 dB and the gaseous absorption of 0.3 dB/km taken from CCIR Report 721 (1978b), for 1 atmosphere of pressure at 20°C and 7.5 gm/m³ of water vapor density accounts for the remainder. Because of the lower pressure due to the 1500-m elevation at Boulder, CO, the absorption would be less if all other parameters were the same.

The 10-in antenna for the transmitter was not optimum at 96.1 GHz. A WR-12 waveguide (60 to 90 GHz) instead of WR-10 (75 to 110 GHz) was used for the antenna feed. With the 6-port analyzer, the voltage standing wave ratios (VSWR) were measured for four waveguide flange connections between WR-12 and WR-10. Of the four measurements, the best and worst VSWR were 1.1 and 1.27, respectively, and the average VSWR was 1.16. These low VSWR's indicate that the effect on the transmitted power measurement of dissimilar waveguide sizes is negligible. The use of WR-12 for the antenna feed had an advantage, because at 96 GHz the attenuation for WR-12 silver rectangular waveguide (TE₁₀ mode) is less by 1/3 than WR-10, resulting in a lower value for P_d . However, a waveguide transition was used between the antenna and the receiver rf port, eliminating the flange mismatch.

Received power P_R at the first stage of the receiver is calculated from

$$P_R \text{ (dBm)} = 10 \log P_T + G_T + G_R - K - 20 \log f - 20 \log d - L_t - L_r - L_a \quad (3.4)$$

where

- P_T = transmitted power in mW
- G_t = transmitting antenna gain in dB
- G_R = receiving antenna gain in dB
- K = constant for units used (32.4 dB)

- f = frequency of the link in MHz
- d = distance between terminals in km
- L_t = loss in waveguide at transmitter in dB
- L_r = loss in waveguide at receiver in dB
- L_a = atmospheric (gaseous) absorption in dB - taken from CCIR Report 721 (1978,b) at 1 atmosphere, 20°C and 7.5 gram/m³ water vapor density.

For the 105-m path, L_a is assumed to be zero. Waveguide loss L_t includes 58.3 dB for the attenuators plus 0.58 dB for the feed and L_r is estimated at 0.62 dB for antenna feed loss. Values of 45.9 dB for G_T and 47.6 dB for G_R were determined from appropriate parabolic reflector diameters at an efficiency of 60 percent. The transmitted power is 27.7 mW. Applying these values to (3.4), P_R equals -64.0 dBm at the first stage of the receiver (rf mixer). Adding the rf-IF gain of the mixer-preamplifier, 1.6 dB gain from the combination of a second IF amplifier, a 30-dB pad and the filter insertion loss resulted in a calculated value of -28.6 dBm at a calibrated log-amplifier. The measured value for the 105-m path was -28.1 dB checked with a calibrated signal generator at 242 MHz.

Temperature controllers are used in the transmitter and receiver enclosures to limit the range of component temperature change, which in turn reduces changes in system gain that could occur due to normal ambient temperature excursions at the terminals. Full proportional control devices using thermistor sensors regulate resistive heaters to raise the enclosure temperatures to 39°C (102°F). Bi-metallic switches are used to control blowers that circulate fresh air for cooling when the enclosure temperatures exceed 39°C. The proportional control characteristics of the heating device and the thermal lag in the system enclosures, permits the use of a zero differential between the heating and cooling temperature. Link gain stability is maintained at ± 0.5 dB over an ambient temperature range from -25°C to + 35°C.

Antenna pointing on long paths, such as the 27.2-km diagnostic path, becomes a problem due to visual clutter around the antenna at the terminals. Sighting was particularly difficult from the transmitter, looking into the urban Boulder and mountain background. Haze and air turbulence can also add to the problem. The transmitter and receiver are both mounted in enclosures equipped with precision elevation and azimuthal scan capability. Thus, when the antennas have first been coarsely aligned with the aid of spotting scopes, they can then be aligned with precision by monitoring the received signal level. Repetitive scans in elevation and azimuth at both the transmitting and receiving terminals assure main beam

alignment. Signal loss from pointing errors was reduced to less than -0.5 dB. This level of accuracy is accomplished by selecting optimum times for pointing (during periods of minimum scintillation) and by signal averaging.

With the antennas properly aligned, an accurate measurement of the total path loss over the 27.2-km path was made for comparison to the 105-m path. Ten-second average values of signal level, at 1315 MST on 9 August 1983, gave a differential path loss of 58.3 dB, by coincidence the same value as the attenuators used for the 105-m calibration path. The free space loss difference is 48.2 dB, so there is slightly over 10 dB (0.37 dB/km) of gaseous absorption loss.

The gaseous losses toward the higher frequency end of the millimeter wave band are largely due to water vapor absorption in clear air. A reading of partial water vapor pressure (e) was determined, using values of refractivity from a microwave cavity-type refractometer measured at the receiving terminal and the equation

$$e_{(\text{mb})} = (NT/300^\circ\text{K} - 0.259P/(1251/T - 0.019)). \quad (3.5)$$

where

N = refractivity index of the atmosphere

T = ambient atmospheric air temperature ($^\circ\text{K}$) and

P = atmospheric pressure (mb).

Equation (3.5) is derived from (2.1) in Section 2. By taking the 10-s average values at 1315 MST on 9 August, 1983, an e of 12.6 mb was calculated (N = 260, T = 300 $^\circ\text{K}$, and P = 834 mb). This value defines only the receiving end of the path, but a significant variation was unlikely unless a frontal system were passing between terminals. Using the value of e at 1315 MST to find water vapor content (R) from the ideal gas law $R = 216.68(e)/T$ gave 8.77 gm/m³. A second sample from data at 1800 MST on 9 August showed the absorption had increased by slightly over 2 dB; when e = 15.9 mb, N = 272, T = 300 $^\circ\text{K}$ and P = 834 mb. There are large disagreements in models for water vapor absorption in the millimeter wave band and it is hoped that with careful calibration and data processing, good experimental data can be obtained to test these models. A detailed analysis on this subject is contained in Section 5.2.

4. OPERATION OF THE DIAGNOSTIC PROBE AND DATA ANALYSIS

As explained in Section 1 and Section 2 the wide-band (30.3-GHz) channel and the 11.4, 28.8, and 96.1-GHz cw channels of the probe were used to measure propagation characteristics and link performance over atmospheric paths.

The separate channels were operated on a short path for calibration before establishing longer diagnostic paths. The wide-band and 11.4 and 28.8-GHz cw links were operated on an 11.8-km path during the summer of 1982 and on a 27.2-km path since February 1983. The 96.1-GHz system was added in early August 1983.

Data collected on these paths are as follows:

a) Received Signal Levels

<u>Frequency (GHz)</u>	<u>Antenna Polarization</u>	
11.4	Transmit (Vertical)	Receive (Vertical)
11.4	" (Vertical)	" (Horizontal)
28.8	" (Horizontal)	" (Horizontal)
30.3	" (Vertical)	" (Vertical)
96.1	" (Vertical)	" (Vertical)

b) Bit Error Rate (BER) Data

30.3 GHz (500 Mbit/s rate)

c) Meteorological Data (Receiving Site Only)

<u>Recorded</u>	<u>Derived</u>
Rain Rate	Water Vapor Pressure
Temperature	Relative Humidity
Pressure	
Refractive Index	

The above data are sampled at 1-s intervals. Time series of 10-s block averages are stored in the computer; bit error rate, rain rate, and receiver signal level data are plotted on the computer CRT. At the end of each hour, these time-series data are stored in disk memory, if predetermined threshold for received-signal, rain-rate, or bit-error-rate levels are exceeded. If these levels are not exceeded, only statistics and histograms are recorded for the hour. With this criteria for data recording, time series are recorded for all periods of local rain (at the receiver terminal), all periods of attenuation (> 6 dB) of any of the receiver signals, and all periods of BER above 2×10^{-6} . Detailed analyses of some time series were made and some analyses of the recorded histograms are presented in Section 5.

4.1 Calibration Path

The 30.3-GHz wideband and the 28.8 and 11.4-GHz cw channels were first operated on a 125-m calibration path. Data from this path provided stability and reliability information and a reference BER for a case where the propagation medium induced negligible attenuation and distortion. Figure 4.1 is a plan view of the top of the U.S. Department of Commerce building in Boulder, CO, with the locations of the transmitter and receiver terminals indicated on the drawing. Figure 4.2 shows the transmitter site as viewed from the receiver in the top picture (a) and the receiving site as viewed from the transmitter site in the lower picture (b). The path is clear of obstacles and provides a far-field ($> D^2/\lambda$) link at these frequencies.

4.2 11.8-km Path

After the calibration measurements, the system was placed on an 11.8-km link to study performance and record data during a controlled multipath mode of operation. The 11.8-km line-of-sight (LOS) link was established by moving the transmitter terminal to a site on Gunbarrel Hill, northeast of Boulder.

The picture in Figure 4.3(a) was taken from the receiver site looking toward the transmitter. The arrow in the center of the photo locates the transmitter. An elevation profile of the path is shown in Figure 4.3(b). Both the transmitter and receiver are at elevations of 1650 m. A ridge (about 40 m high) is located near mid-path and urban Boulder covers much of the path between the receiver and the ridge.

The probe was operated on this path for approximately three weeks. During the first two weeks of this period, the antennas were aligned for a maximum received signal level. During a 4-day period of the third week, the receiving antenna was adjusted to point down two degrees (an elevation angle of -2 deg).

4.2.1 On-Line, Direct-Path Pointing

On the direct LOS path the 30.3-GHz, 500 Mb/s PSK channel provides 100 mW to the transmitting antenna. To compensate for excessive signal strength at the receiver, an rf attenuator between the receiving antenna and the downconverter was set at 29 dB to produce detectable errors (approximately 1×10^{-6} BER). A received signal level (RSL) of -62.5 dBm was chosen as a basis for a direct comparison with the results from the 125-m path.

Data from the 11.8-km path, shown in the upper half of Figure 4.4a, was recorded between 2200 and 2300 MDT on July 22, 1982, indicating a period with stable atmospheric conditions, little turbulence and no refractive layers. The

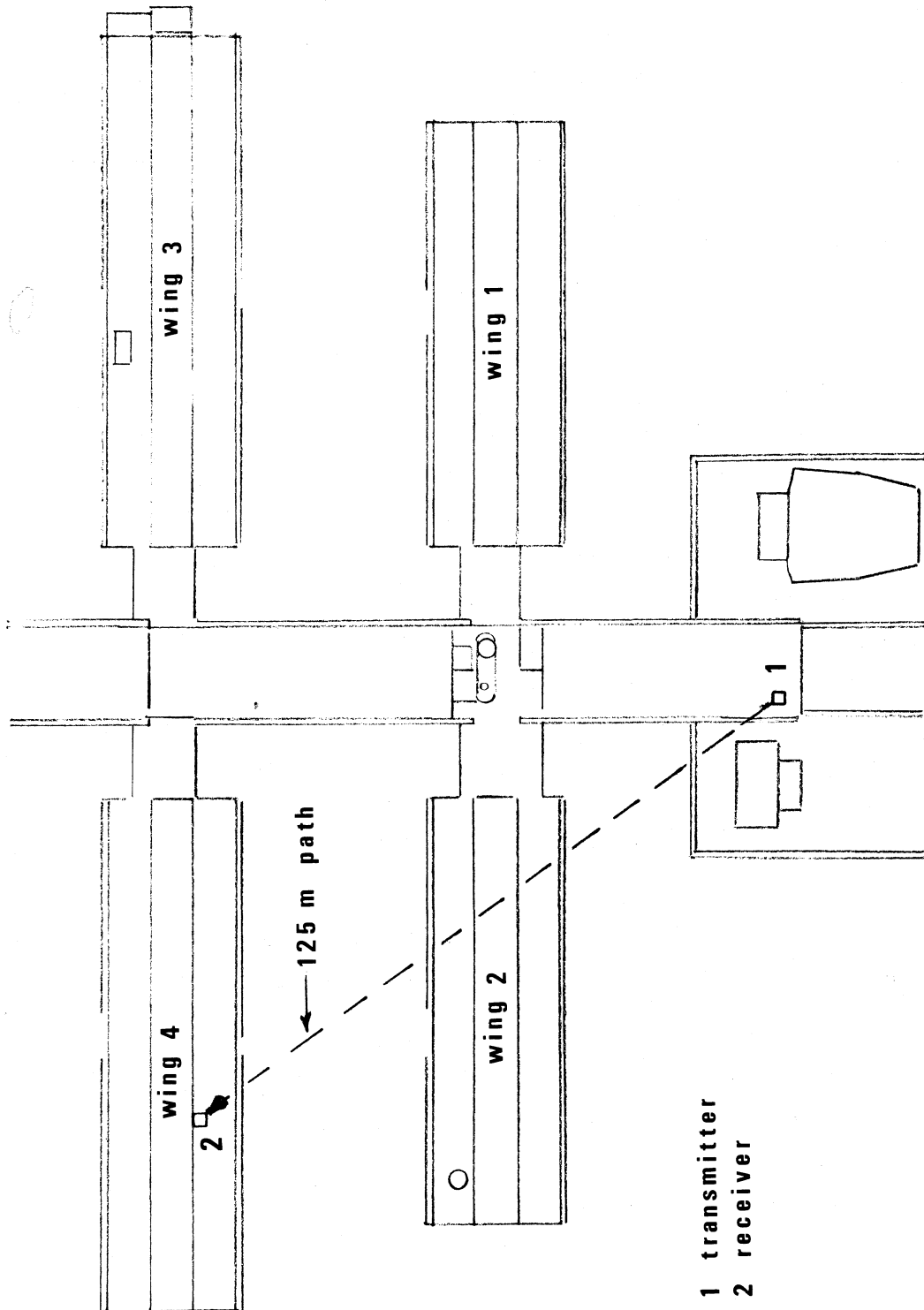
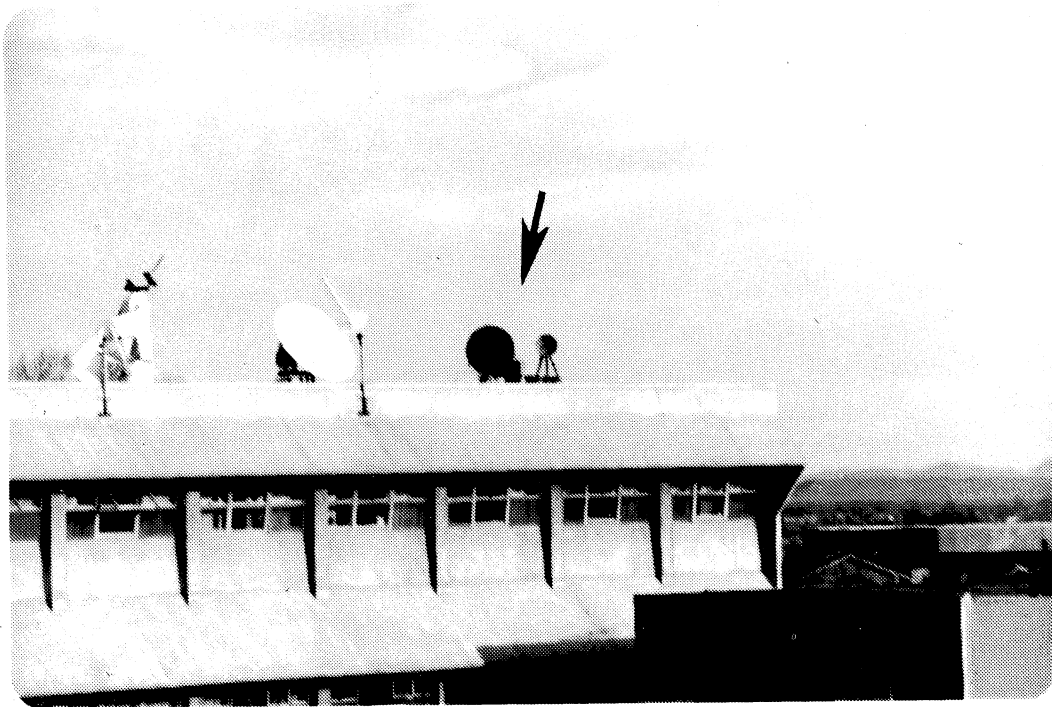
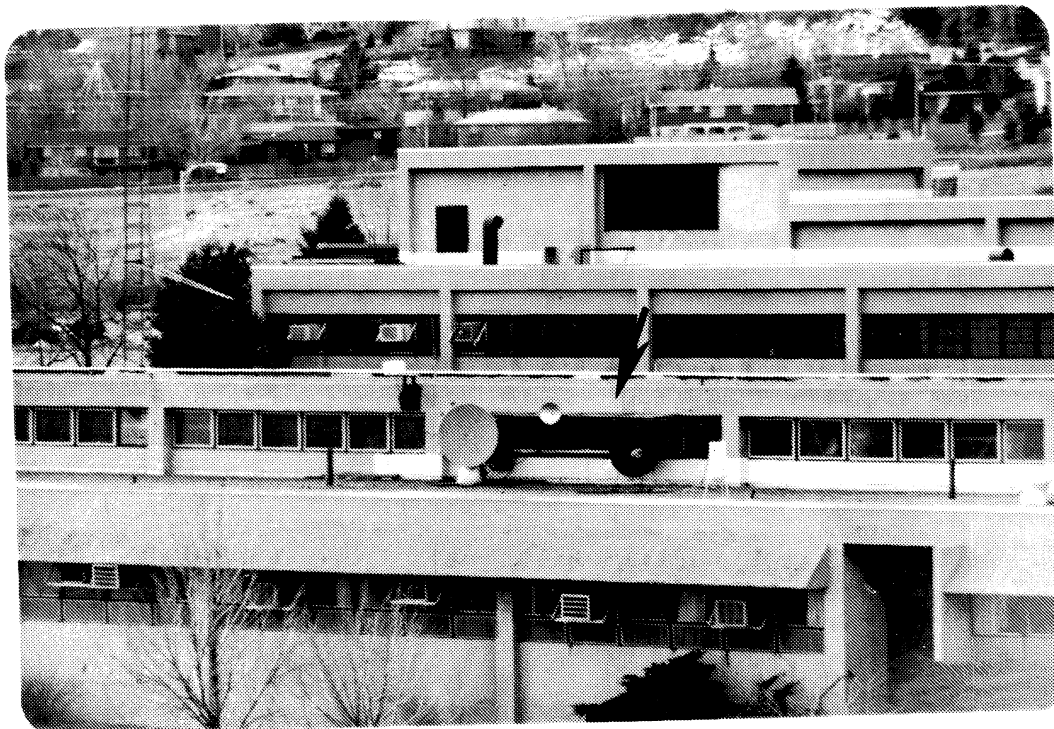


Figure 4.1. The system calibration path.



a.) transmitter site

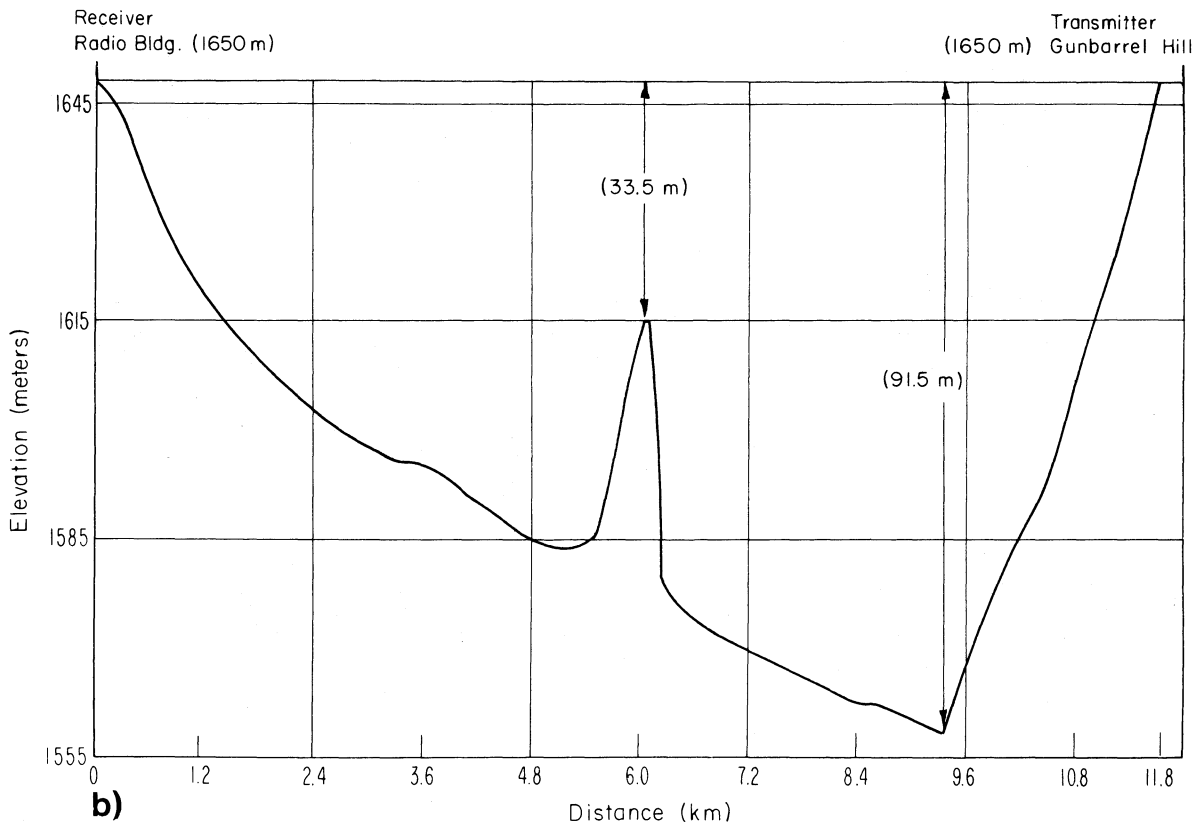


b.) receiver site

Figure 4.2. Photographs of the transmitter and receiver terminals on the calibration path.

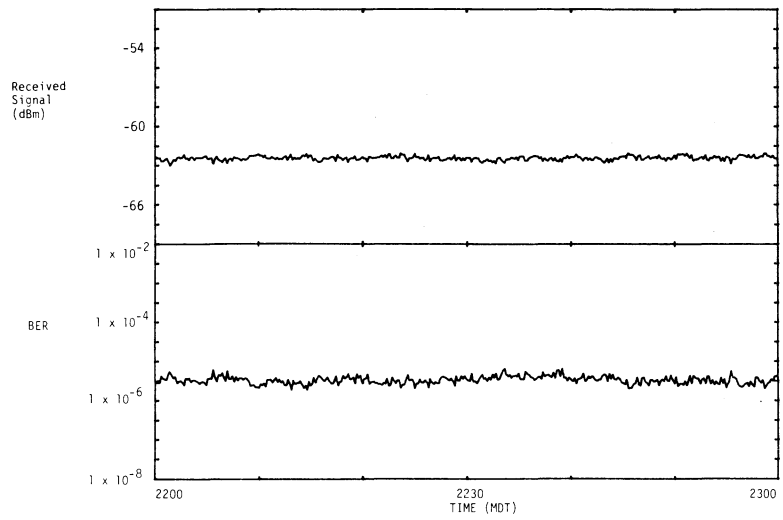


a)



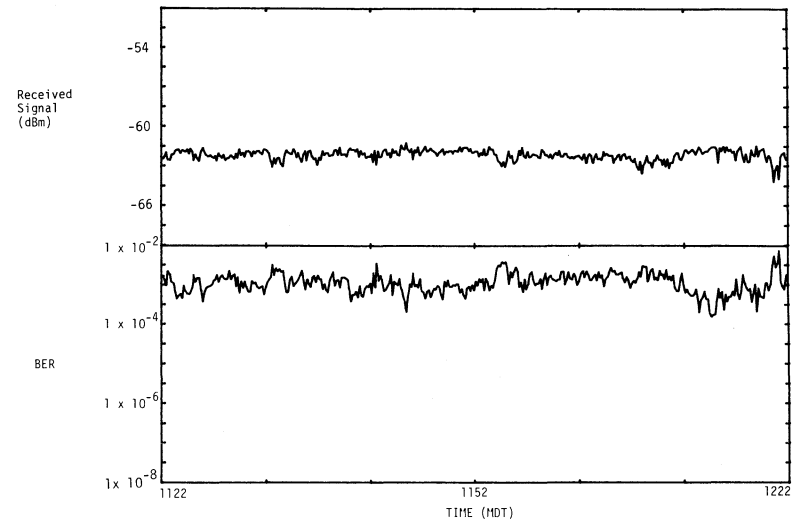
b)

Figure 4.3. A photograph and height profile of the 11.8-km path.



July 22, 1982

Receiving Antenna = 0°



July 23, 1982

Receiving Antenna = -2°

31

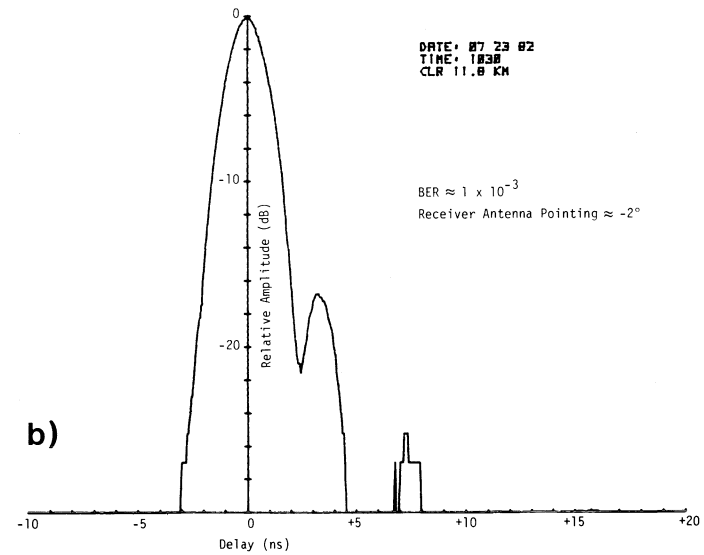
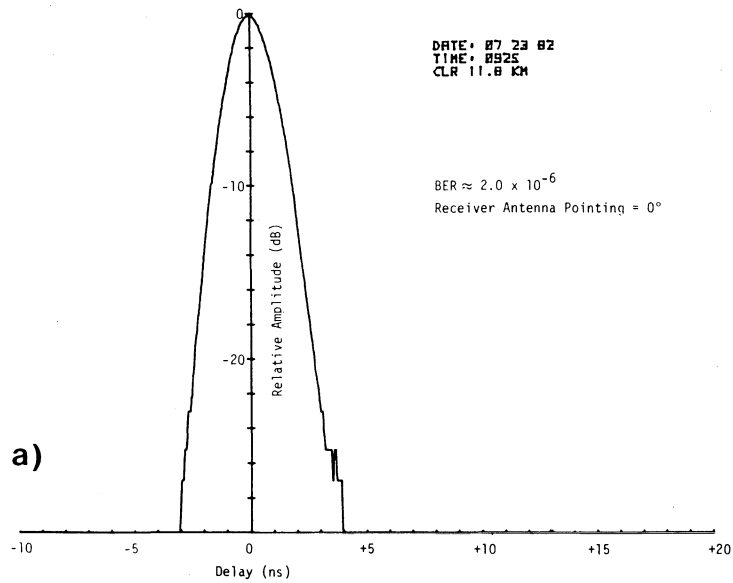


Figure 4.4. Selected RSL and BER recordings at 30.3 GHz and corresponding impulse response curves. a.) with on-line pointing (receiving antenna at an elevation angle = 0 deg), b.) with off-line pointing (receiving antenna at an elevation angle = -2 deg).

lower half of Figure 4.4a contains an impulse response curve recording during a similar stable period. No significant multipath components are evident in this response curve.

4.2.2 Off-Line Pointing

Because no evidence of multipath appeared in the data with the antennas pointing at the 0-deg elevation, the receiving antenna was repositioned downward until significant multipath was observed. This new position resulted in a 2-deg downward shift that produced a 20-dB reduction in signal level at the antenna because the direct signal was no longer on the main lobe of the receiving antenna. To compensate for this reduction, the rf attenuator was changed from 29 dB to 9 dB. This change brought the RSL back to the level for the 0-deg pointing. Changes in the BER and the impulse response curves, resulting from this change in operating mode, are shown in Figure 4.4b. The BER increased to an average 1×10^{-3} from the previously recorded 2×10^{-6} and a broadening of the impulse response curve indicates the presence of multipath. Three impulse response curves are superimposed in Figure 4.5, including the curve shown in Figure 4.4b. These curves, taken with the receiving antenna at -2 deg elevation pointing, show a range of amplitudes of the multipath component and corresponding bit error rate. The multipath amplitude range varies between -14 dB and -20 dB, relative to the direct component. The multipath delay is approximately 3.2 ns, the difference between the occurrence of the peak amplitude of the direct component and the occurrence of the peak amplitude of the multipath component. The variation in the multipath amplitude is thought to be due to atmospheric variations that cause a bending of rays over the irregular terrain.

4.2.3 Performance in the Presence of Multipath Signals

Data plots such as the upper half of Figures 4.4a and 4.4b show an inverse correlation between the RSL and BER. As the received signal increases, the S/N increases (noise level is determined by the front end mixer) and the BER decreases; and vice-versa. However, in the presence of multipath, the BER is a function of both S/N and distortion producing intersymbol interference. A scatter plot, Figure 4.6, represents the system calibration on the 11.8-km path and shows the correlation between the 1-s RSL and BER samples. These data were recorded by first setting the rf attenuator at a level to produce measurable errors (approximately 3×10^{-6} as observed in Figure 4.4a). The rf attenuator was then stepped above and below the reference operating level producing a response curve for clear-air, non-distorted conditions. This set of data follows the shape of the BER vs S/N

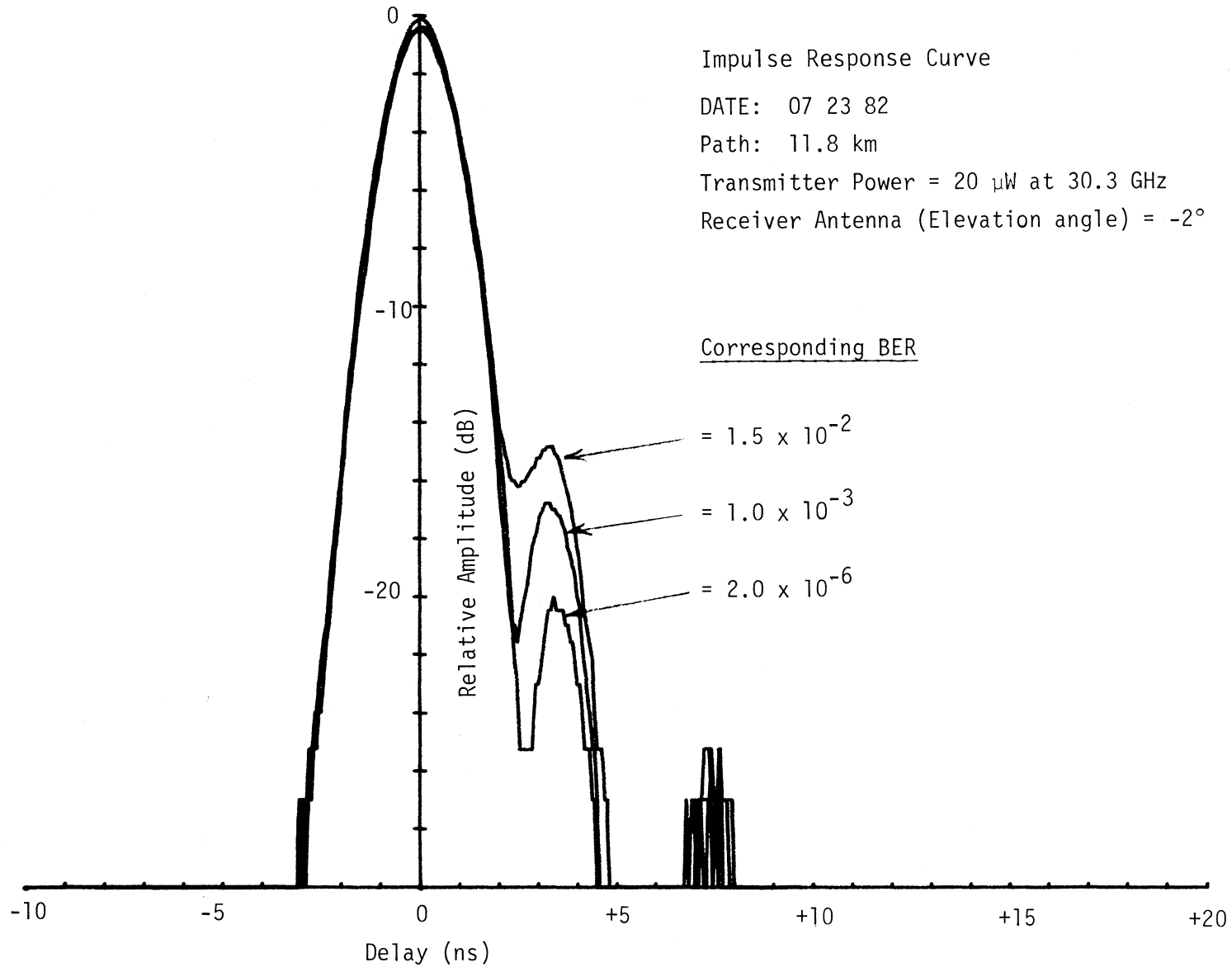


Figure 4.5. An ensemble of measured impulse response curves with the receiving antenna pointing at -2 deg (elevation angle).

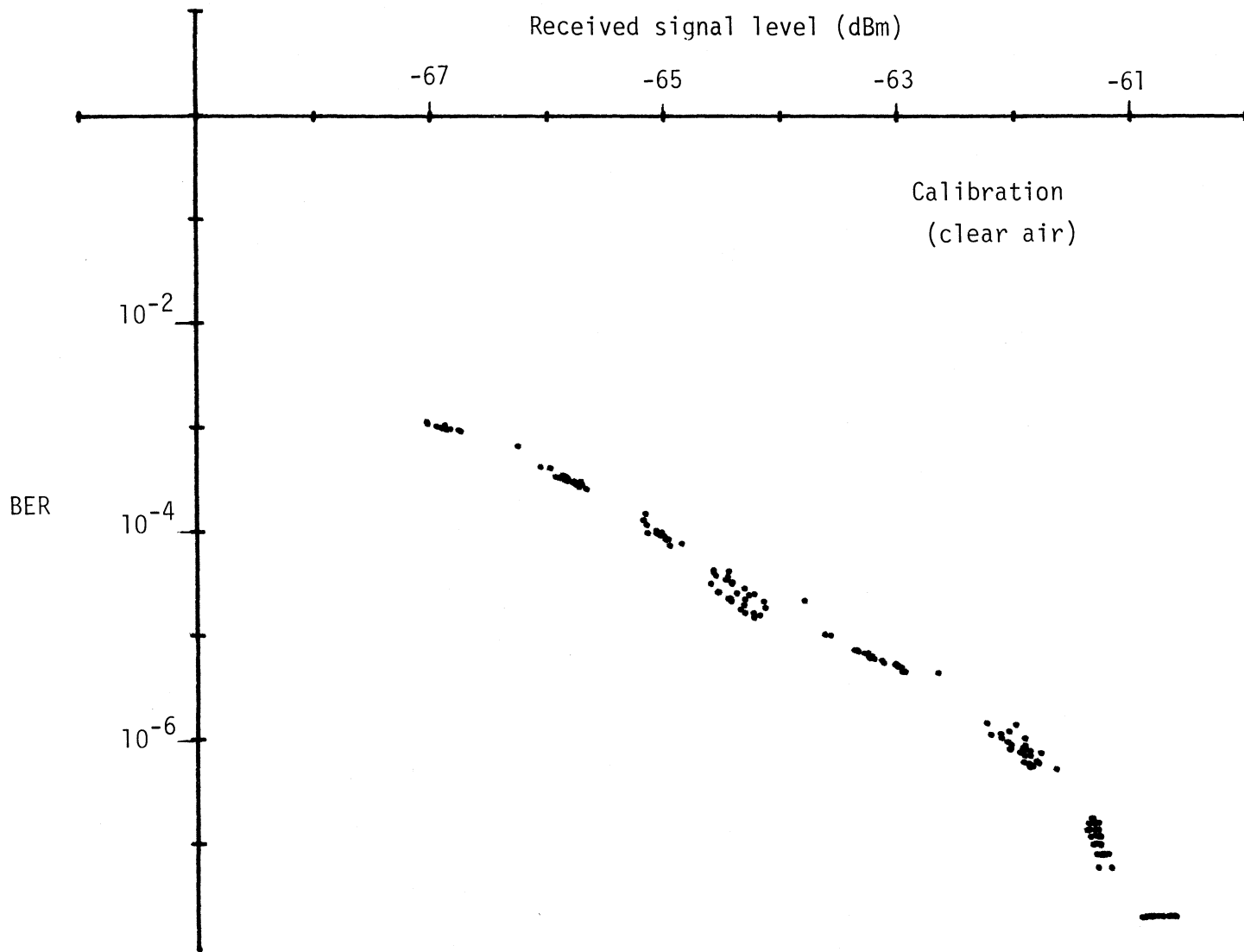


Figure 4.6. A scatter plot of RSL and BER representing the system calibration response operating on the 11.8-km path.

curve for back-to-back operation of the system reported by Violette, et al., (1983). Examples of multipath propagation conditions are shown in Figures 4.7, 4.8, and 4.9. A smooth line representation of the data in Figure 4.6 is added to the above figures as a reference. The data in Figure 4.7 show an example of the correlation between RSL and BER on a link without significant multipath. The presence of strong inverse correlation is evident in Figure 4.7a and in the scatter plot of Figure 4.7b. If no distortion exists on the channel, the scatter plot should follow the reference curve. When channel distortion is present, such as intersymbol interference, then a departure from the reference will occur. The data points in Figure 4.7b are only slightly spread and show a small offset relative to the measured reference (traced as a heavy line). This small offset and spread may be due to some low-level distortion (multipath) but mostly it is due to the fact that there are amplitude scintillations on the channel produced by a turbulent atmosphere. These amplitude scintillations induce false point spreading and apparent offsets in the data since the BER is an accumulated count over a 1-s interval, while the signal level is an instantaneous reading at a given time during the 1-s interval. Whereas the data in Figure 4.7 were recorded with the receiving antenna at 0 deg elevation angle, representing a condition of only slight multipath, the data in Figures 4.8 and 4.9 were recorded with the receiving antenna at -2 deg elevation angle generating a multipath signal at about 14 to 20 dB below the direct ray. The scatter plot in Figure 4.8b representing the RSL and BER data in Figure 4.8a, shows a large offset relative to the reference trace and a small spread of the data points. This is a condition of intersymbol interference due to significant multipath but with not much variation in the received signal amplitude. By contrast, the scatter plot in Figure 4.9b shows both a large offset and spread resulting from a condition of intersymbol interference due to significant multipath and a less stable atmosphere producing considerable variation in the received signal levels.

4.2.4 Performance During Rain

Rain along an operating path causes signal attenuation as a function of rain rate, drop-size distribution, and effective storm cell size. The system signal-to-noise and BER are strongly correlated with attenuation. No attempt was made to correlate rain rates with signal attenuation or BER, because only one gauge (at the receiving terminal) was used to monitor rain rate.

However, during the few days when it rained, sufficient data were collected to determine if there was evidence of distortion due to time delay dispersion caused by rain scatter. Data shown in Figure 4.10 indicates that rain scatter components in this case are not large enough to produce detectable channel distortion.

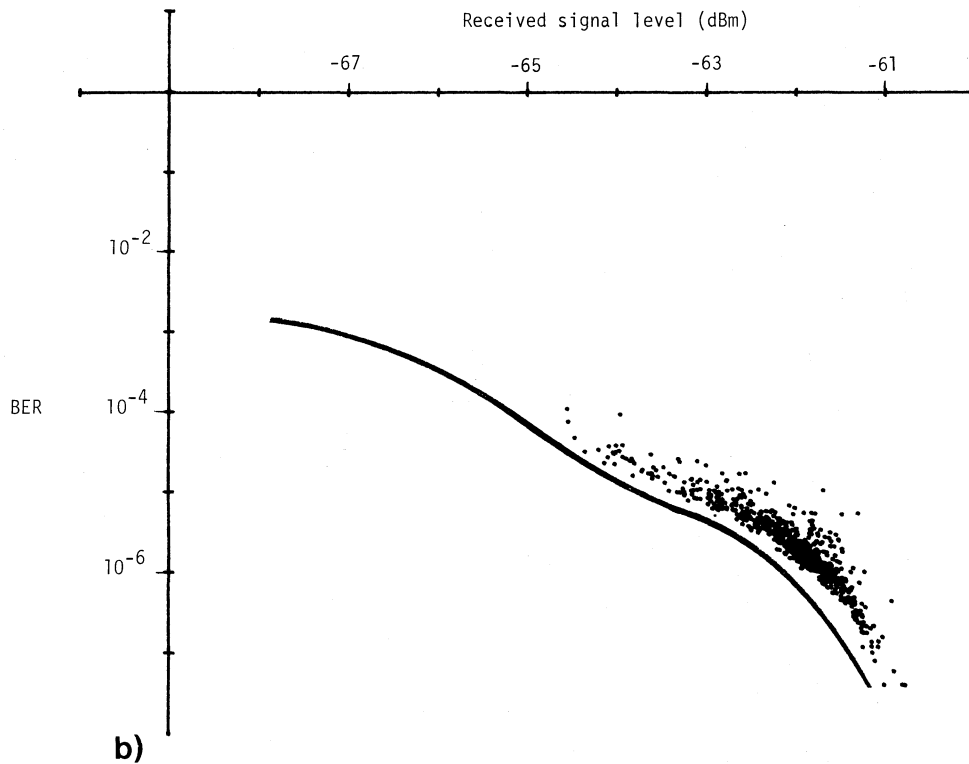
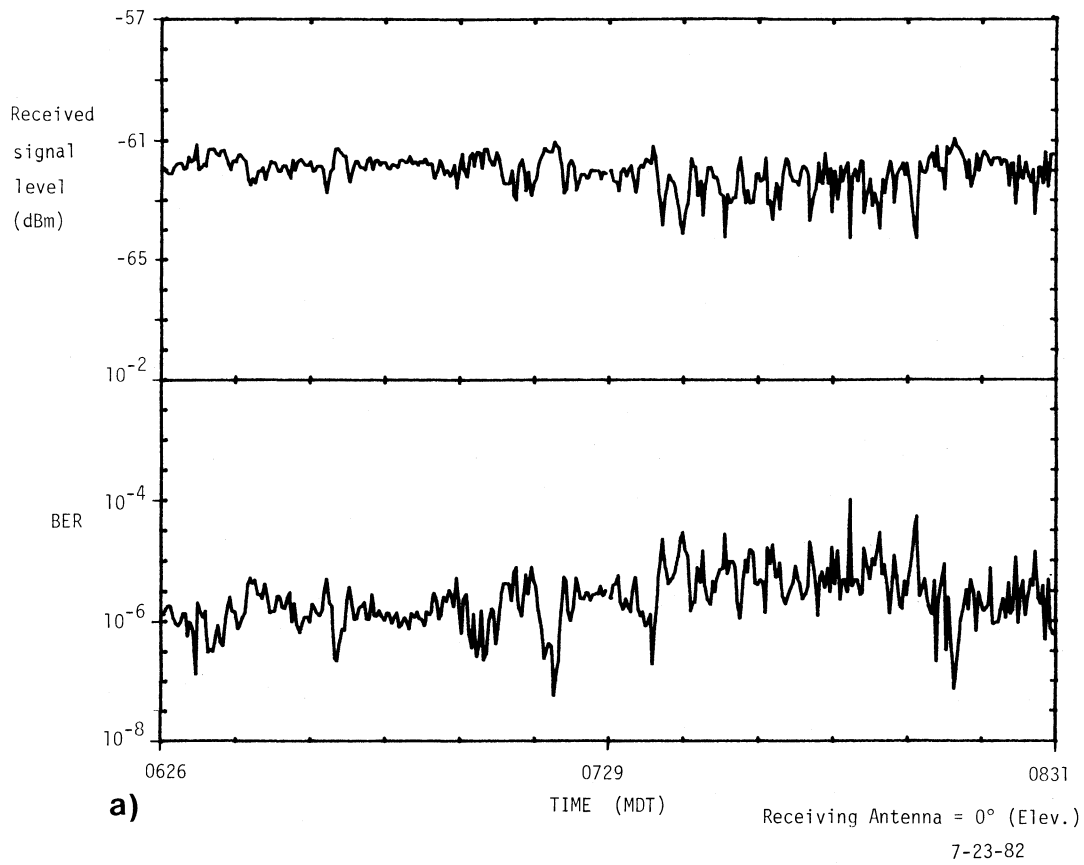


Figure 4.7. RSL and BER data and a corresponding scatter-plot with the receiving antenna elevation angle at 0 deg.

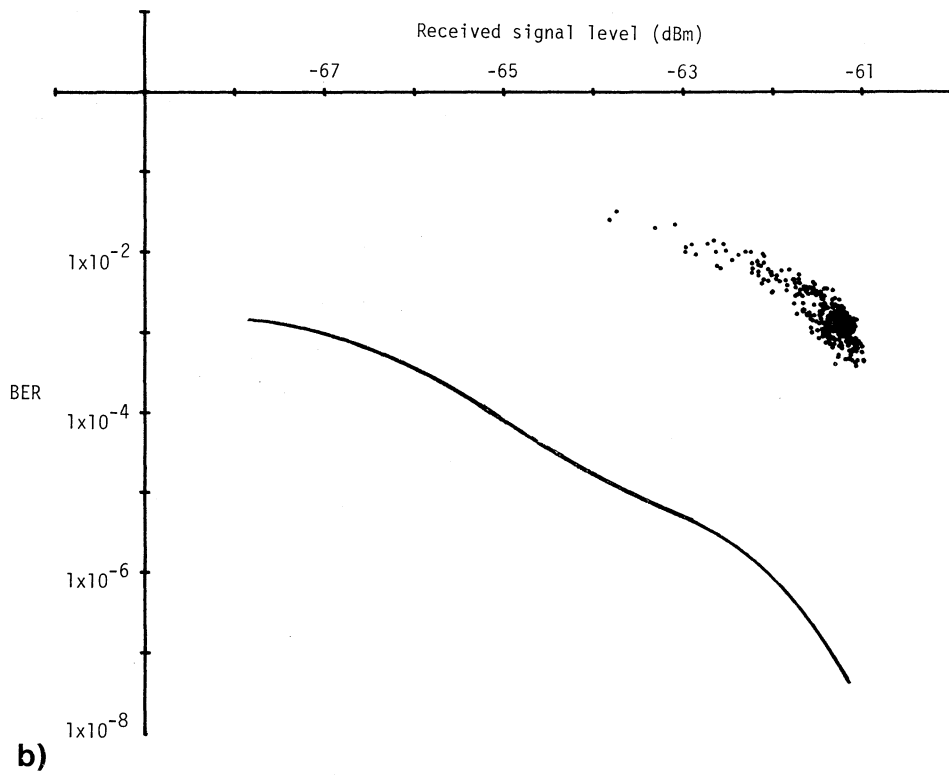
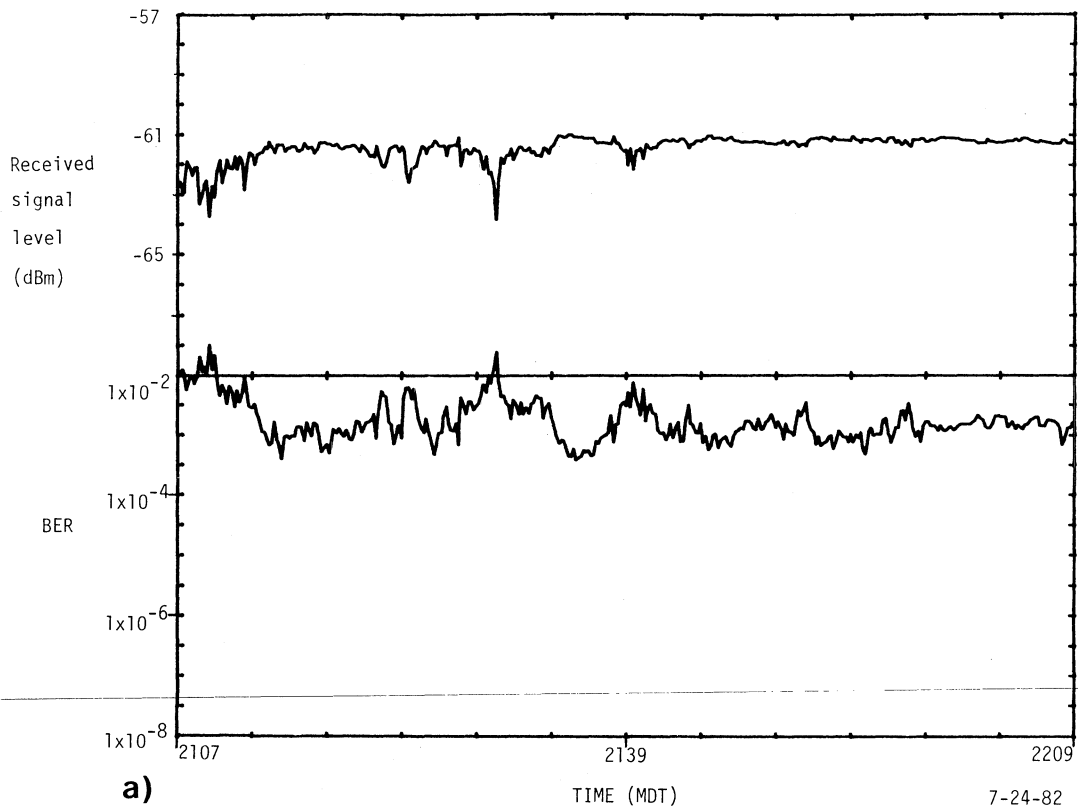


Figure 4.8. RSL and BER data and a corresponding scatter plot with the receiving antenna elevation angle at -2 deg.

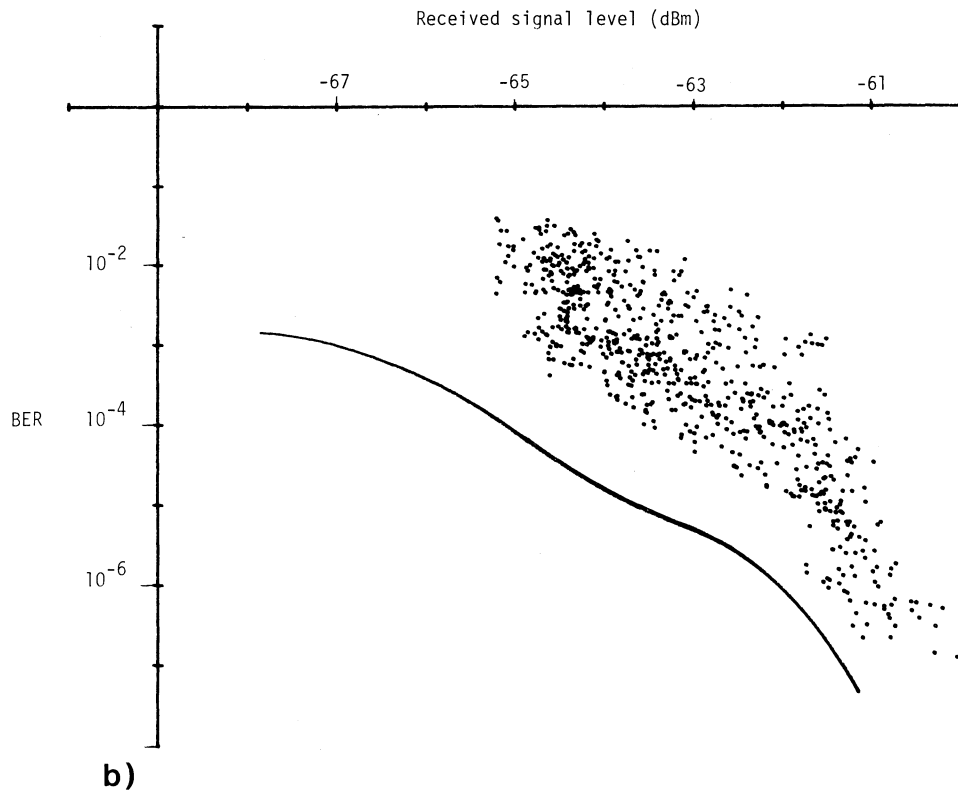
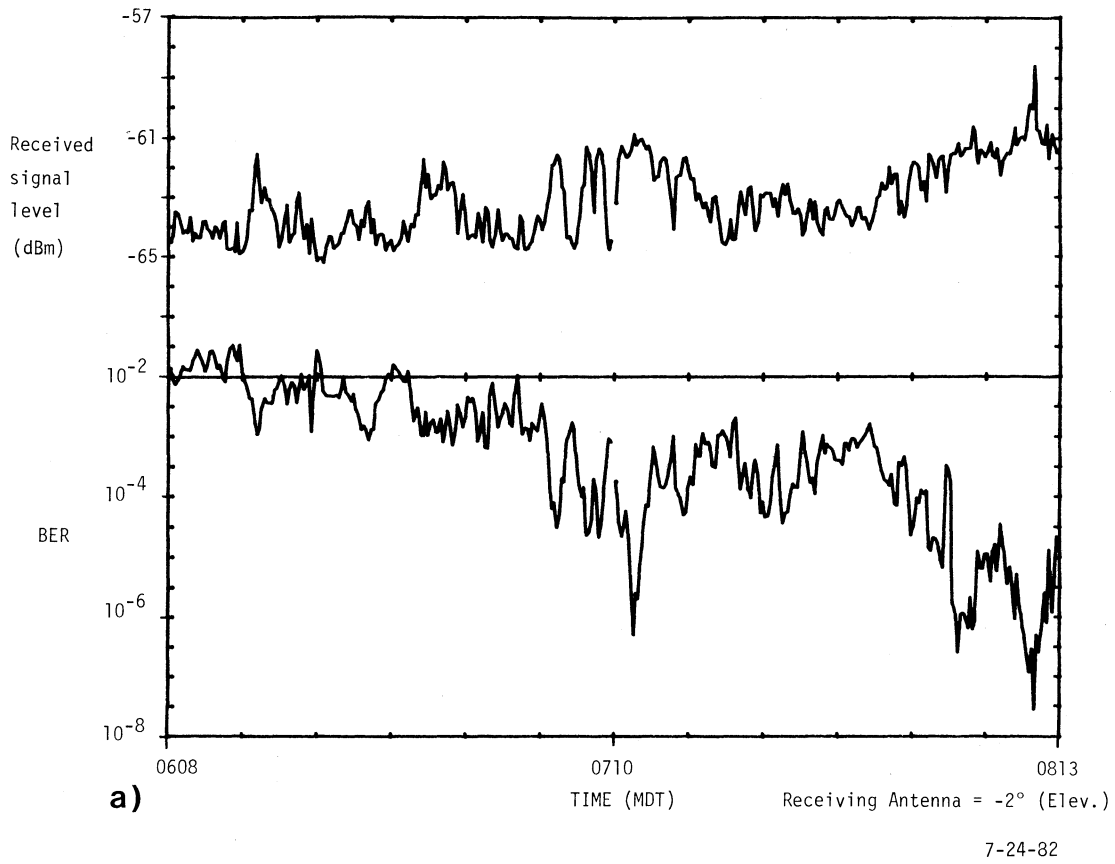


Figure 4.9. RSL and BER data and corresponding scatter plot with the receiving antenna elevation angle at -2 deg. Strong RSL variations.

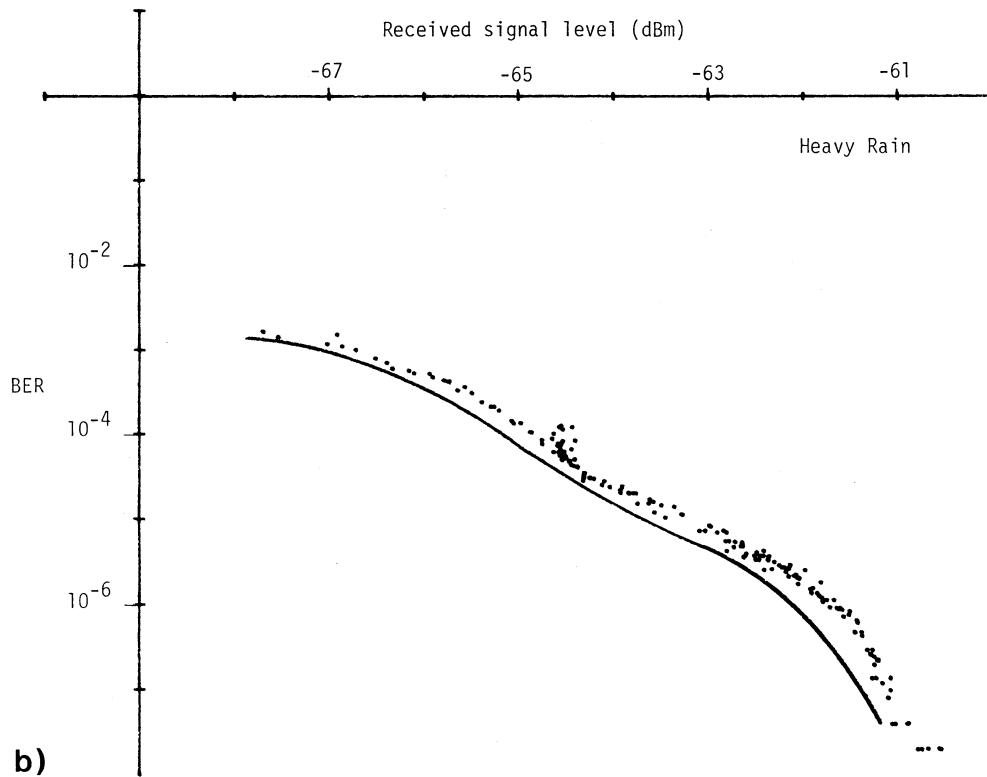
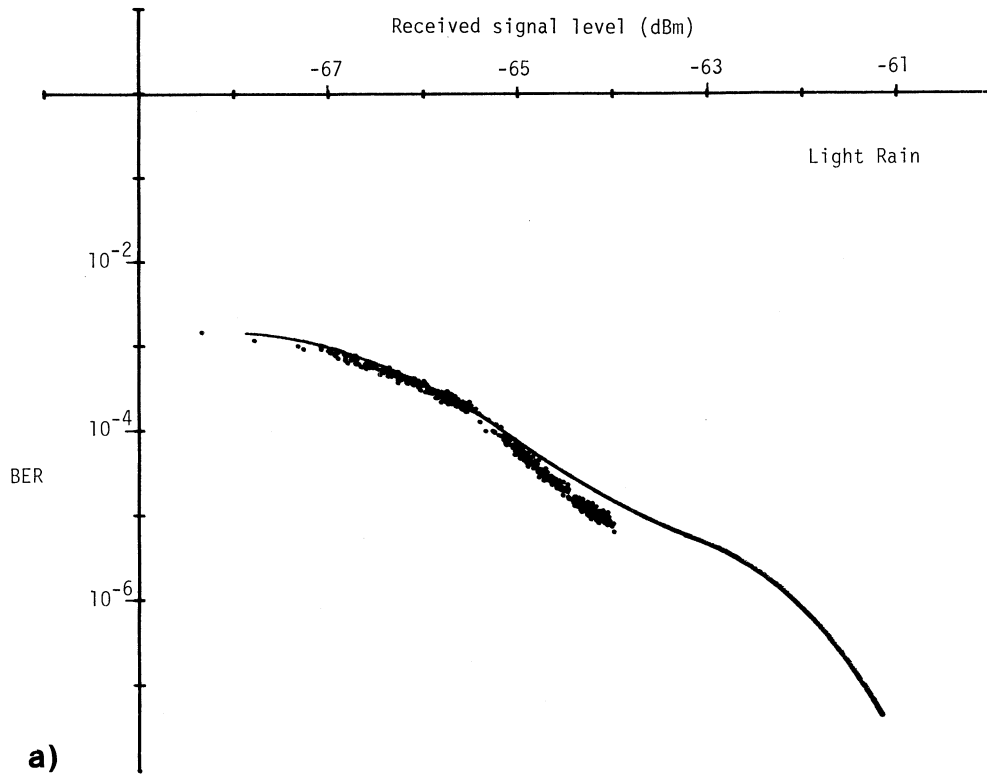


Figure 4.10. Scatter plots of RSL and BER measured on the 11.8-km path during rainfall.

The data in Figure 4.10 (a and b) are scatter plots from periods of rainfall. It is obvious that both figures show a good correlation between the RSL and corresponding bit error rates, and that these correlated data closely followed the reference curve (described in the previous section). Had errors due to time delay dispersion been present, a spread and increase in BER would be evident, similar to the data in Figures 4.8b and 4.9b, when significant multipath was present. The received signal level in Figure 4.10a shows a loss of about 4 dB due to attenuation during a light rain. In Figure 4.10b, rain attenuation of up to 25 dB was observed and rain-rates of more than 50 mm/h were recorded at the receiver terminal. In recording these data, the rf attenuator was manually adjusted to keep the received signal levels within the system AGC range.

4.3 27.2-km Path

Following operations on the 11.8-km test path (Section 4.2), the transmitter terminal was relocated to a site 27.2 km north of the receiver terminal, Figure 4.11 shows the receiver and transmitter terminal locations and path height profile. Antenna beamwidths and operating frequencies are indicated in the figure. The ray paths are also shown for a constant refractive index gradient of -40 N/km (standard value of N change with height) and for a 390 N/km gradient. The latter gradient will just illuminate the surface at the center of the antenna beams. The receiver terminal is at a height of 1654 m. The transmitting terminal is on the west end of Table Top Mountain at an elevation of 1646 m. The first 7-km segment of the path starting at the receiver terminal is across the city of Boulder and the remainder is over open fields and farms. This path runs generally parallel to the foothills on the west, approximately 5 to 7 km from the first mountain ridge.

Figure 4.12 shows the terminal sites and a segment of the 27.2-km path. Figure 4.12(a) was taken at the transmitter site looking toward the receiver site, as was Figure 4.12(b), which shows more clearly the farm land and open field portion of the path. The photograph in Figure 4.12(c) was taken at the receiving site looking toward the transmitting terminal. The arrow indicates the transmitter location on the horizon.

On the 11.8-km path (Section 4.2), the receiver input level at 30.3 GHz was adjusted for a measurable BER in clear air. On the 27.2-km path, all rf attenuation at the receiver was removed for a maximum received signal level and minimum BER. This mode of operation resulted in an average received signal level at 30.3 GHz of -48 dBm in clear air and a BER below 1×10^{-10} . The other channels were also adjusted for maximum received signal level, which were determined to be -67 dBm, -47 dBm, and -64 dBm, at 11.4, 28.8, and 96.1 GHz, respectively. These received

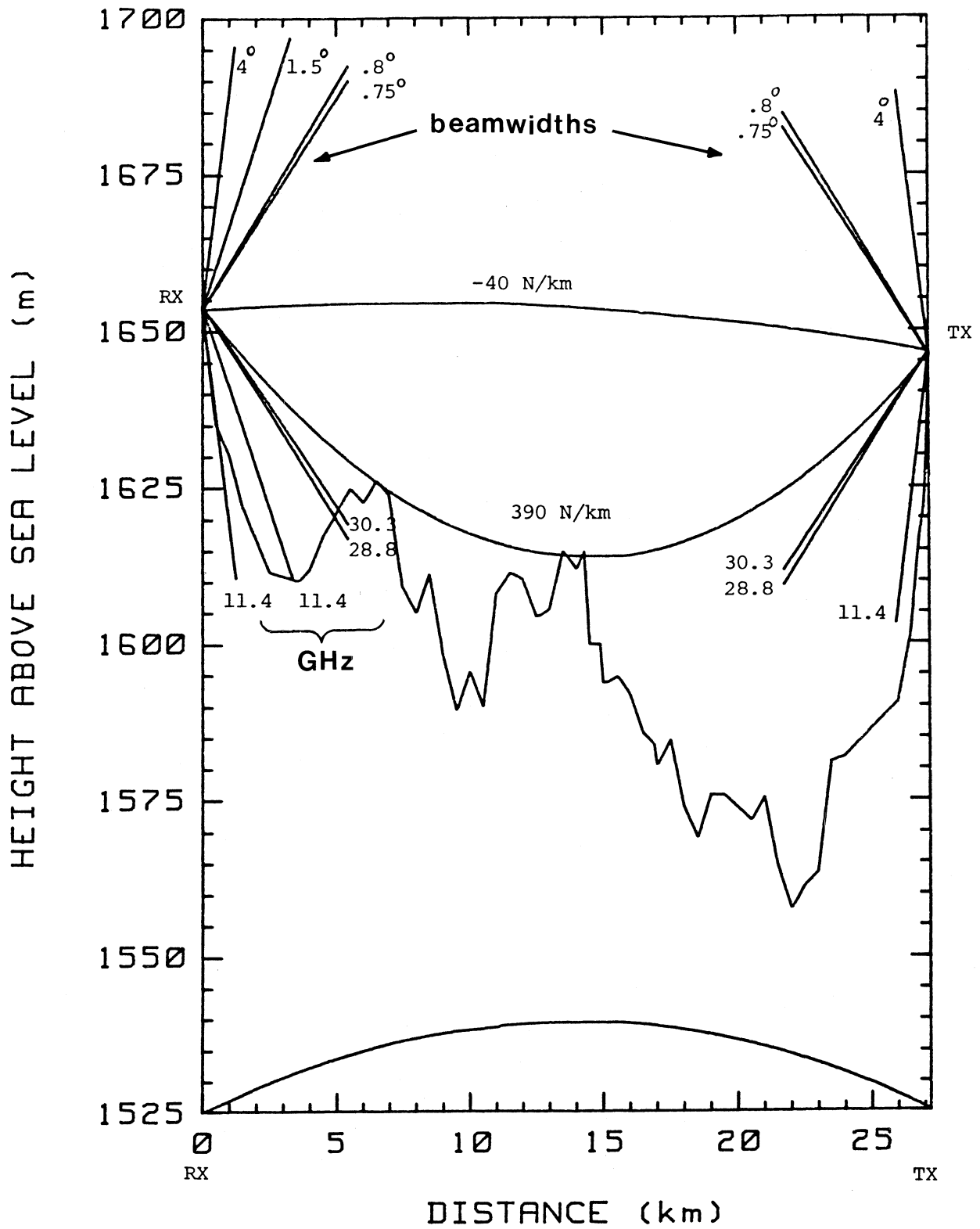


Figure 4.11. Height profile of the 27.2-km diagnostic path.



Figure 4.12. Photographs of the 27.2-km diagnostic path.

signal levels were measured by substituting equivalent levels from a calibrated signal generator at the output of the rf mixer. The conversion loss of the mixers was added to these substitute levels resulting in the above quoted received signal levels as determined at the rf mixer input. The conversion loss values used were nominally-specified values that may differ from actual values because the mixers may not have been optimally tuned at the operating frequency in all cases.

Using the free-space propagation equation (3.3) given in Section 3, received signal levels were calculated for comparison with the measured levels.

The calculated received power levels and corresponding measured levels at each of the four frequencies are given below:

11.4 GHz

$$\begin{aligned}
 f &= 11.4 \text{ GHz} && \text{antenna (TX)} = 18 \text{ in (4 deg BW)} \\
 P_t &= 75 \text{ mW} && \text{antenna (RX)} = 18 \text{ in (4 deg BW)} \\
 d &= 27.2 \text{ km} \\
 P_r &= 18.75 + 32.0 + 32.0 - 32.44 - 81.2 - 28.7 \\
 &\quad - 1.0 - 3.0 - 0.35 \\
 &= \underline{-63.45 \text{ dBm}} && \text{calculated} \\
 P_r &= \underline{-67.0 \text{ dBm}} && \text{measured}
 \end{aligned}$$

28.8 GHz

$$\begin{aligned}
 f &= 28.8 \text{ GHz} && \text{antenna (TX)} = 36 \text{ in (0.8 deg BW)} \\
 P_t &= 70 \text{ mW} && \text{antenna (RX)} = 36 \text{ in (0.8 deg BW)} \\
 d &= 27.2 \text{ km} \\
 P_r &= 18.45 + 46.6 + 46.6 - 32.44 - 89.2 - 28.7 \\
 &\quad - 2.5 - 1.0 - 2.45 \\
 &= -44.6 \text{ dBm} && \text{calculated} \\
 P_r &= \underline{-47.0 \text{ dBm}} && \text{measured}
 \end{aligned}$$

30.3 GHz

$$\begin{aligned}
 f &= 30.3 \text{ GHz} && \text{antenna (TX)} = 36 \text{ in (0.75 deg BW)} \\
 P_t &= 100 \text{ mW} && \text{antenna (RX)} = 36 \text{ in (0.75 deg BW)} \\
 d &= 27.2 \text{ km} \\
 P_r &= 20.0 + 47.1 + 47.1 - 32.44 - 89.6 - 28.7 \\
 &\quad - 2.5 - 1.0 - 1.9 \\
 &= \underline{-41.9 \text{ dBm}} && \text{calculated} \\
 P_r &= \underline{-47.7 \text{ dBm}} && \text{measured}
 \end{aligned}$$

96.1 GHz

$$\begin{aligned} f &= 96.1 \text{ GHz} & \text{antenna (TX)} &= 10 \text{ in (0.85 deg BW)} \\ P_t &= 27.7 \text{ mW} & \text{antenna (RX)} &= 12 \text{ in (0.70 deg BW)} \\ d &= 27.2 \text{ km} \end{aligned}$$

$$P_r = 14.4 + 45.9 + 47.6 - 32.44 - 99.6 - 28.7 \\ - 0.62 - 0.58 - 6.53$$

$$= \underline{-60.6 \text{ dBm}} \quad \text{calculated}$$

$$P_r = \underline{-64.0 \text{ dBm}} \quad \text{measured at water vapor pressure of 12.6 mb.}$$

As seen from the above methods of determining received signal power, the measured values for all frequencies are less than the calculated values as would be expected. It is particularly difficult to estimate antenna gain; thus the values used in the calculations were computed for the nominal sizes at an efficiency of 60%. One would not expect the actual gain to exceed this value. Antennas for the 11.4-GHz link had been in field use for many years and suffered reflector surface damage and the feed position was not necessarily correct for the operating frequency; either condition reduces the gain. The 28.8 and 30.3-GHz links share an orthomode transducer for simultaneous orthogonal dual linear polarization, which obviously cannot be optimized in gain at both frequencies. An antenna range to measure gain with good precision requires elaborate instrumentation and an extensive setup effort; therefore, a short calibration path (described in Sections 3 and 4.1) to remove most of the system gain uncertainties was chosen as the most suitable option.

Other gain uncertainties are excessive rf transmission line losses, rf mixer conversion loss, and antenna pointing loss, all of which may contribute to a lower measured value of received signal. Losses due to gaseous absorption plus any other clear-air propagation losses have not been extensively measured nor are modelled values verified, especially for the higher frequencies. Therefore, determining these losses is of particular interest.

The 96.1-GHz system, however, did receive a thorough calibration allowing accurate identification of all rf hardware losses described above leaving only the antenna pointing and atmospheric path losses to be determined. With signal level averaging, antenna pointing errors can be reduced to less than -0.5 dB, therefore, the gaseous absorption loss measurements at 96.1 GHz are believed to contain this degree of accuracy. An analysis of these data appears in Section 5.2. Other data

processing techniques can reduce measuring errors still further and details of these will be discussed in subsequent reports.

The fade margin values for the 27.2-km path as presently instrumented are -41, -35, -31, and -32 dB, at 11.4, 28.8, 30.3, and 96.1 GHz respectively. During the 7-month operating period, these fade margins were exceeded on channels 28.8, 30.3, and 96.1 GHz only during heavy rainfall. The fade margin on the 11.4-GHz channel was not exceeded. It should be noted that these fade margins can easily be extended in an operational link. For an experimental system, extra waveguide lengths to accommodate polarization switching, the combined packaging for multi-frequency diagnostics, and provision for transportability increases rf attenuation and losses due to some impedance mismatches. Also for single frequency links, optimization of antenna performance and IF filtering will improve fade margin performance. In the near future fade margins on all cw channels will be increased by at least 10 dB by means of improved bandpass filtering so that deeper fades can be recorded.

Having discussed the maximum received signal levels, calculated and measured power levels, and fade margins; the following subsections describe specific channel characteristics as a function of season, precipitation, fading, etc. These data indicate the performance of a communications link and are useful as input data for propagation models.

4.3.1 Seasonal Data

The records in Figure 4.13 are two examples of the data format displayed on the computer monitor showing samples of typical received signal levels during the springtime. The data in each figure covers a 24-h period starting at 0000 MST. Received signal levels are plotted for each frequency and BER at 30.3 GHz is shown by dots to indicate the error rate for a particular 1-s interval. During periods of low BER, only sporadic dots appear, because most of the time the BER is below 1×10^{-8} , the lowest level on the scale. No rain occurred for the two days represented in Figure 4.13; consequently, there are no line tracings for rain rate. Typical received signals for spring have scintillation levels of about 2 dB and low-level, short-duration fades of 2 to 3 dB. These data represent very stable operating conditions as indicated by the very low BER.

A second set of data shown in Figure 4.14 represents summer conditions. The format for these data is the same as in Figure 4.13. The significant differences between the summer and spring data are the greater scintillation levels and the greater fade depths during the summer. These increases in scintillation are caused by enhanced turbulence due to convective heating and the deeper fades result from

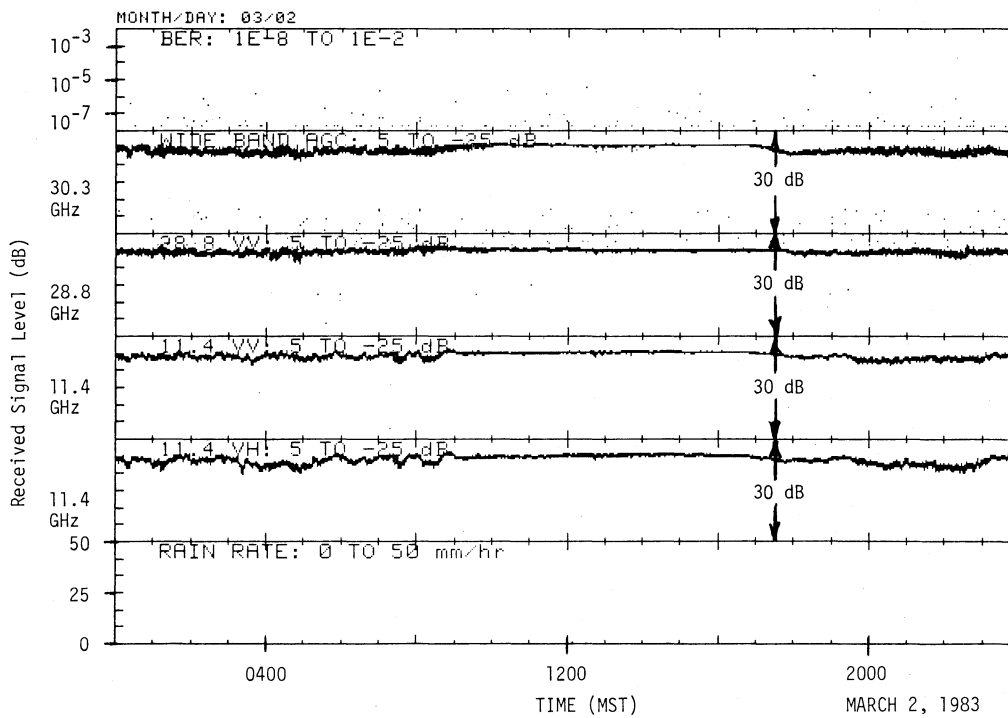
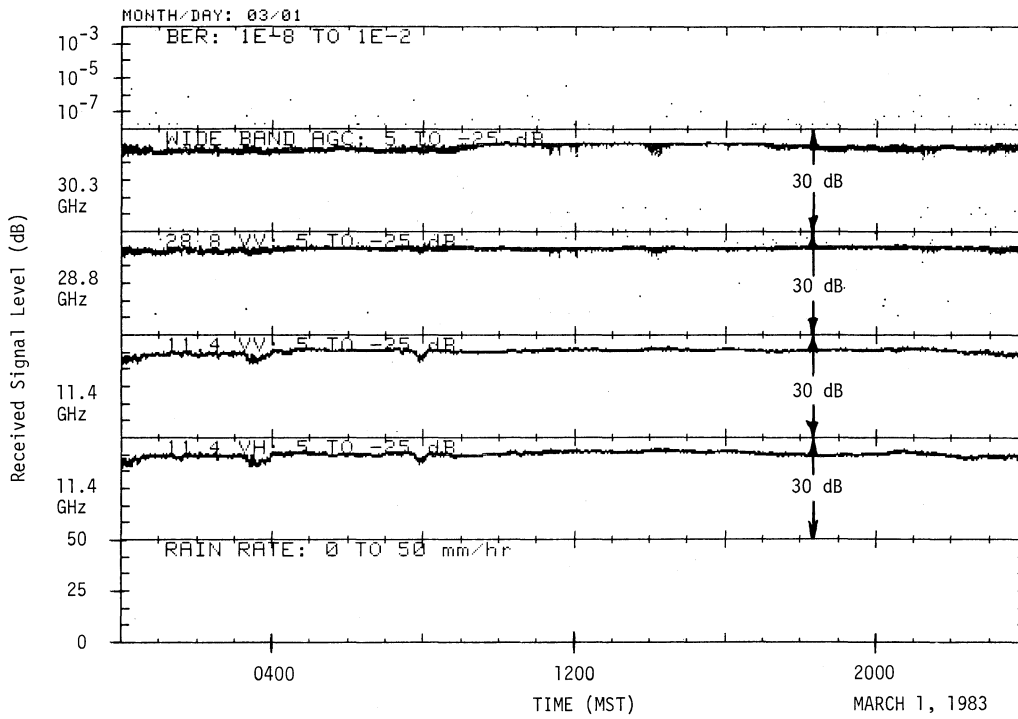


Figure 4.13. Typical spring-time records from the 27.2-km path showing bit-error-rate, received signal levels (11.4, 28.8, and 30.3 GHz) and rain rate.

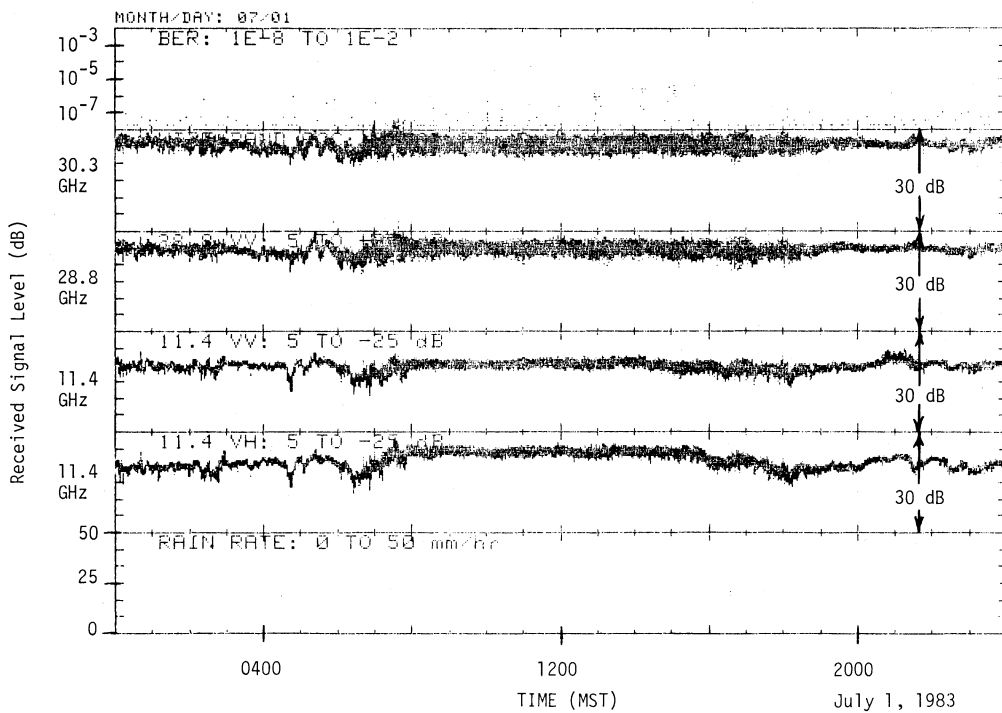
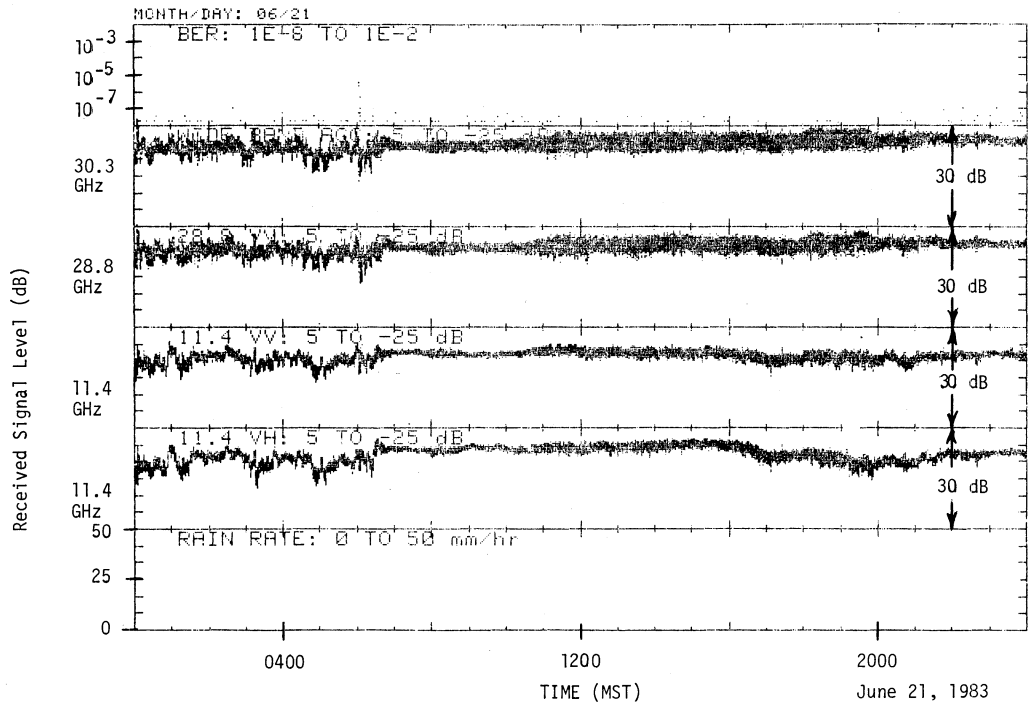


Figure 4.14. Typical summer-time records from the 27.2-km path showing bit-error-rates, received signal levels (11.4, 28.8, and 30.3 GHz) and rain rate.

increased ray bending as the result of nighttime atmospheric layering in the presence of warm moist summer air. Even with scintillation levels of 6 to 8 dB and fades of the same magnitude, channel performance in terms of BER for example, was not affected.

The recording periods shown in Figures 4.13 and 4.14 are for clear-air conditions free of precipitation, but the signal behavior shows evidence of occurrences of refractive layering along the path. Also, these data indicate that a 27.2-km clear-air channel can support a wide band digital link at a 500 Mb/s without detectable distortion or increase in BER.

4.3.2 Fog, Snow and Rain Data

In this section, the effects of fog and precipitation are discussed. Neither fog nor snow caused detrimental signal attenuation. However, during some heavy rain storms, the fade margin was exceeded for short periods with maximum bit error rates recorded.

Fog

Although, occurrences of heavy fog are not common in the Boulder area, two such periods were noted during observations between the middle of February and the middle of September, the first on February 25 and the second on March 24. The data for these two days are shown in Figure 4.15, using the format shown in Figures 4.13 and 4.14. The primary effects of fog on the path are an increase in signal attenuation at 28.8 and 30.3 GHz and essentially no change in the level of the 11.4-GHz signals (the 96.1 GHz channel was not yet in operation). The increase in attenuation of the 28.8 and 30.3-GHz signals is first observed at about 0300 MST for the fog that occurred on February 25. The fog covered most of the path with estimated visibility at daybreak in the range of 100-200 m. Attenuation due to fog for this event reached maximum levels at about 0530 MST. Maximum attenuations of 8 dB on the 30.3-GHz channel and 6 dB on the 28.8-GHz channel correspond to a uniform fog over the path of almost 0.25 g/m^3 (Liebe, 1984). Short periods of increased BER are noted during the fog event, but are not directly attributable to the attenuation due to fog. On this date, the BER receiver had only been in service for a few days and was still being adjusted for optimum performance.

In the March 24 recordings, maximum attenuation levels of 5 dB and 4 dB are noted on the 30.3 and 28.8-GHz channels, respectively, at 0730 MST. These signal level changes are attributable to the fog on that day; however, visual observations indicated that the fog was not as extensive as on February 25.

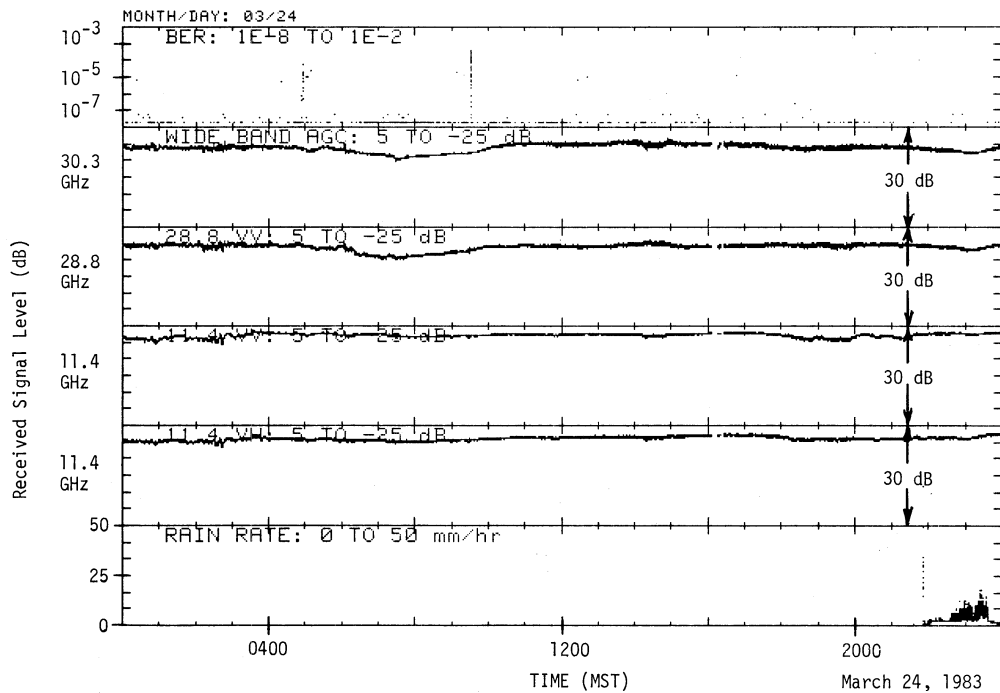
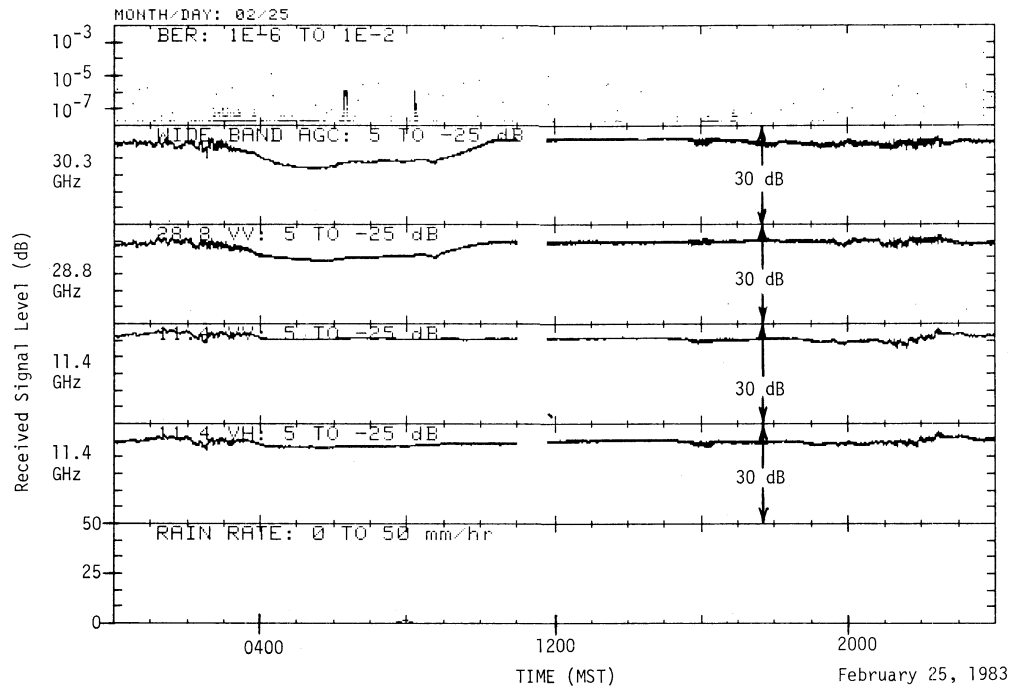


Figure 4.15. Time series records for periods of fog on the 27.2-km path between the hours of 0300 and 1030 on February 25 and between the hours of 0500 and 1030 on March 24, 1983.

Although the data reported in Figure 4.15 are from only two fog events, they are typical from the standpoint of duration and intensity of what occurs in the Boulder area. Based on these observations, link outages due to fog would not be expected.

Snow

The system was in operation during several snowstorms during the spring. One such storm started on March 15 and continued through March 17. This storm covered a large area, including the propagation path, with periods of heavy snowfall observed. The records for March 16 and March 17, Figure 4.16, show essentially no increase in attenuation during the snowstorm. The rain-rate traces show heavy precipitation rates (for snow) during the storm, particularly on the 16th.

The examples in Figure 4.16 are typical of major storms for this area. Based on these observations, a link outage due to attenuation from snow appears unlikely for this climate and path length.

The data in Figure 4.17 show a transition period from rainfall to snowfall. In the early hours of March 15, rain occurred on the 27.2-km path, causing significant signal attenuation on all channels and BER in excess of 1×10^{-2} . Sometime during the night, the rain changed to snow and continued for most of the next 3 days. Of interest in this figure are the high signal attenuations on the 30.3 and 28.8-GHz channels during the rain and the corresponding increase in BER as the 30.3-GHz signal level is reduced. The gap in the data from 0230 to 0320 MST resulted from a software instruction that was changed later. These data show a strong correlation between the attenuation of the 30.3-GHz channel and the recorded BER as the rain attenuation builds and subsequently decreases, whereas during the remaining 3 days of snow no significant attenuation resulted from even heavy snow. A point to remember in interpreting the results recorded on this path is that only one rain rate gauge was used (at the receiver); it was obviously not an indicator of the precipitation rate for the entire path. It was, however, helpful as a monitor to indicate periods of area precipitation. More rain data are presented and discussed in the next section.

Rain

Data from two of the many rainy days during the monitoring period are shown in Figure 4.18 as examples of signal attenuation due to rain and associated bit error rates. Segments of these rainstorms and others are presented and discussed in detail in this section and statistical analyses of rain attenuation are presented in Section 5.

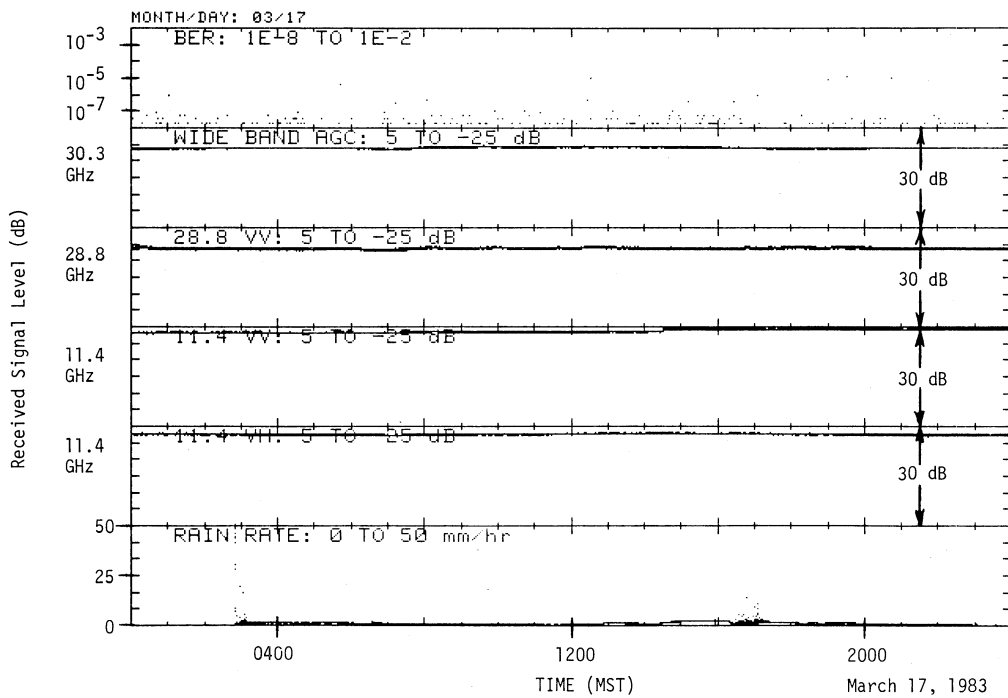
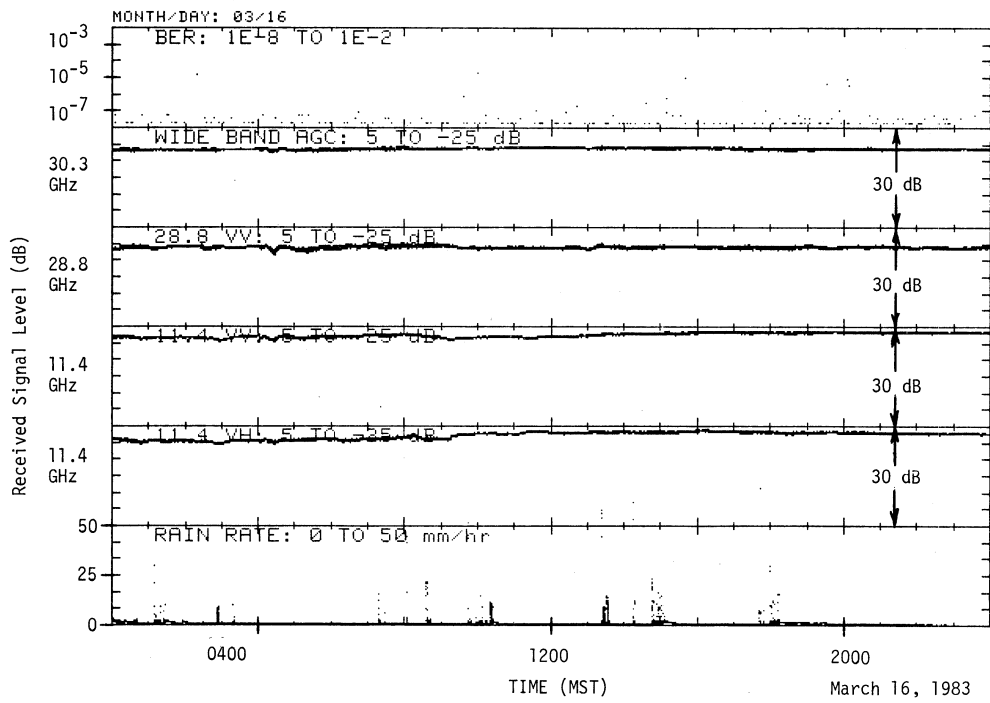


Figure 4.16. Time series records for periods of snow on the 27.2-km path occurring on March 16 and 17, 1983.

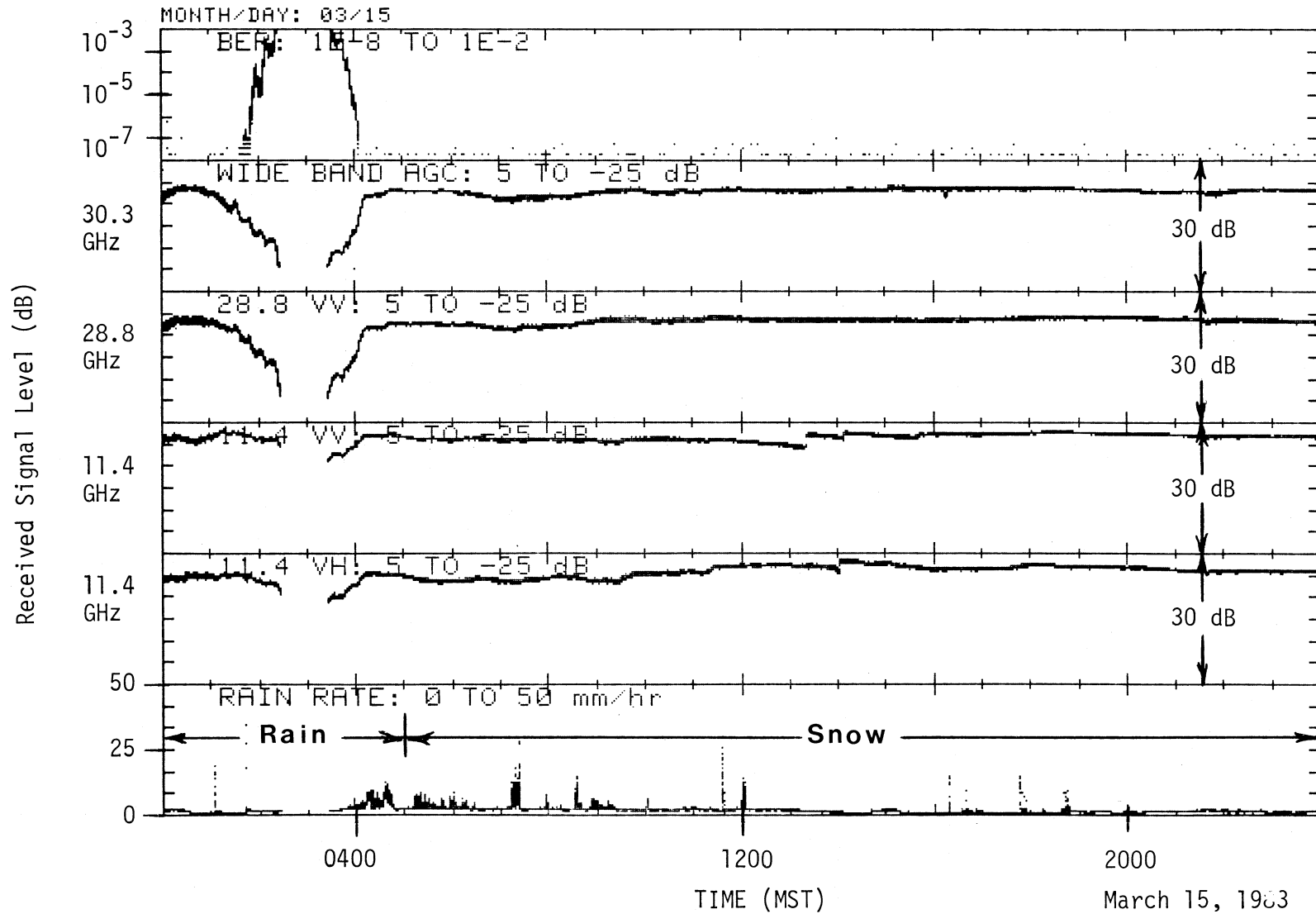


Figure 4.17. A time series record showing periods of rain and snow on the 27.2-km path on March 15, 1983.

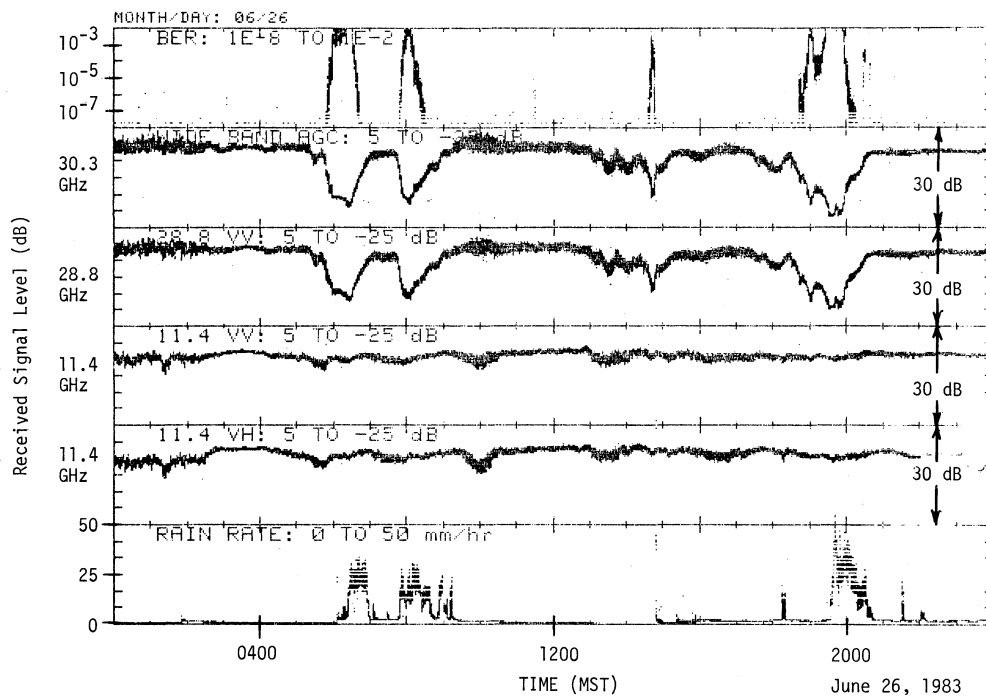
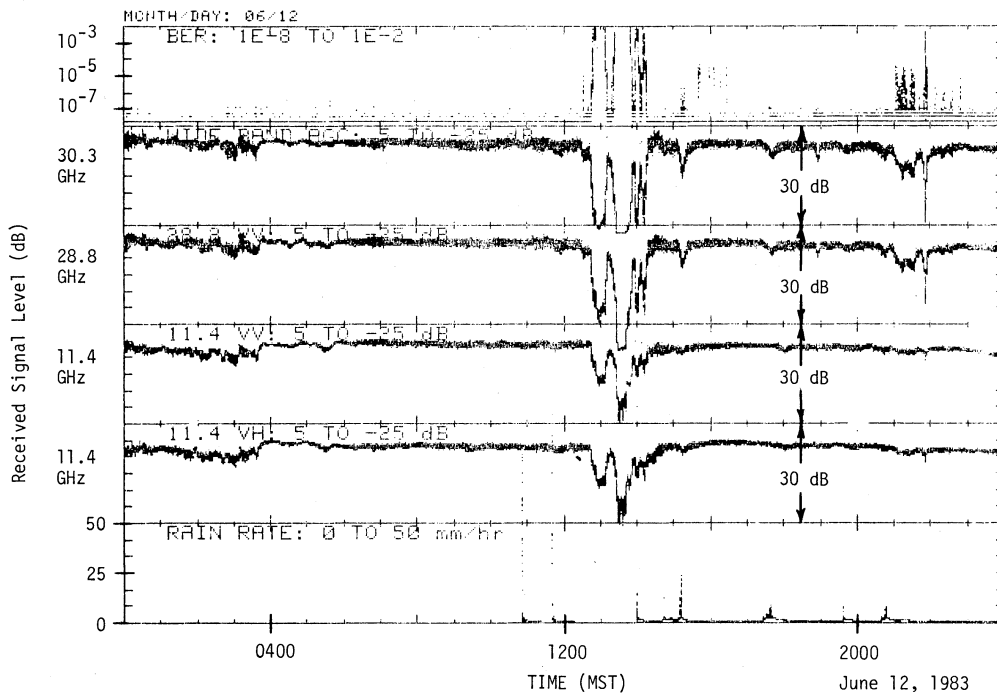


Figure 4.18. Time series records showing periods of rain on the 27.2-km path occurring on June 12, and June 26, 1983.

On June 12, in the 2-h span from 1230 to 1430 MST, periods of large attenuation are observed on all four signal channels and bit error rates exceed 1×10^{-2} . Later in the day, short periods of less attenuation and smaller bit error rates occur. These periods of attenuation (build-up and decay) are typical of most convective storms, resulting from a rain cell moving through the path. First the leading edge progresses until it centers on the path, then diminishes in extent as it moves out of the path. Because the 27.2-km path parallels the foothills and several canyons funnel into the path from the higher elevations in the mountains, it is possible for two or perhaps more cells to be in the path simultaneously during periods of high convective storm activity. This helps explain the overlapping peaks of signal attenuation seen around 1300 MST on June 12 and the attenuation due to rain activity in the afternoon of June 26th.

It is interesting to compare this path with a 22.8-km path that extended directly east, perpendicular to the foothills. Rain rate gauges were used at both ends of the second path for almost two years, high rain rates (15 mm/hr or more) never occurred at both ends simultaneously. In addition, maximum attenuation did not exceed 26 dB at 28.8 GHz whereas, on the foothill path, rain attenuation exceeded 30 dB on several occasions during a 7-month period.

In these data, the ratio between the 30.3 and 28.8-GHz attenuation levels for a given rain event is interesting because this ratio is affected by antenna polarization and somewhat by the drop-size distribution of the rain on the path. Also there is a strong correlation between the 30.3-GHz received signal amplitudes and the recorded bit error rates. For these rain events, the bit error rates are entirely due to received S/N levels as opposed to channel distortion caused by time delay dispersion due to forward scattering in rain.

Figure 4.19 shows the 1200 to 1600 MST segment of the time series from June 12 in greater detail. These data show the strong correlation between BER and the 30.3-GHz received signal level (RSL). During the time period 1330 to 1345 MST, the attenuation for both 30.3 and 28.8 GHz exceeded the fade margin (-27 dB for 30.3 and -32 dB for 28.8 GHz). At the same time, the BER reaches 5×10^{-1} , which is the point of maximum errors with a 50% probability of correctly receiving a bit.

Also to be noted in this data is the ratio of signal attenuations as a function of frequency (the higher frequencies, 30.3 and 28.8 GHz versus the lower frequency 11.4 GHz). Using 30.3 GHz horizontal-to-horizontal antenna polarization (HH) and 11.4 GHz VV as an example, the attenuation ratio in decibels at 1300 MST is 25/12 or approximately 2 to 1. This rainstorm was described as a thunderstorm or a convective type of storm cell. A different type of rain produced the results

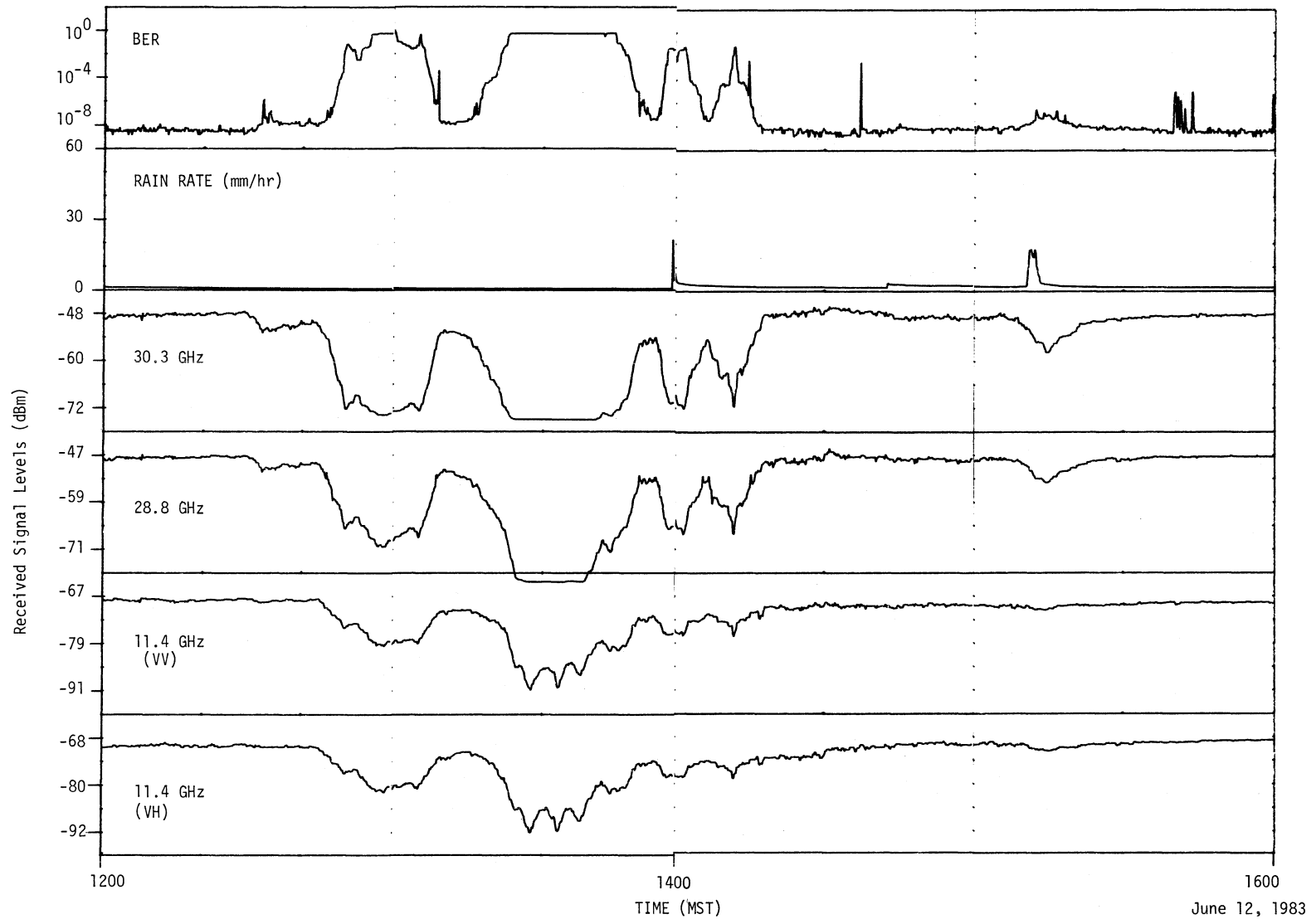


Figure 4.19. Time series records showing results from the 27.2-km path during a rain storm between 1200 and 1600 hours on June 12, 1983.

in Figure 4.20. These data were recorded on June 26, between 1700 and 2100 MST. This storm was described as a frontal system, slowly moving into the path and covering a large area. The highest attenuations occurred at approximately 1945 MST, when the 30.3-GHz level dropped to -21 dB. This produced a BER of 1×10^{-1} . At this time the local rain rate (at the receiver) was about 40 mm/hr. The received signal levels (30.3 and 28.8 GHz) show increasing attenuation starting at about 1730 MST indicating rain on the path. At 1845 MST, the RSL had dropped to -10 dB (30.3 and 28.8 GHz) and the BER receiver was beginning to record errors. During this entire period, the maximum increase in attenuation noted on the 11.4-GHz channels never exceeded 2 to 3 dB, with a resultant attenuation ratio of 21/3 or about 7/1. This result contrasts sharply with the ratio of 2/1 observed for the June 12 rain. The difference in the attenuation as a function of frequencies is thought to depend primarily to the raindrop-size distributions associated with the two storms. Further comment is made on this subject in Section 5, where data from approximately 100 separate rain events have been analyzed.

Two additional rain examples are shown in Figure 4.21. These are the time series for 1500 to 1800 MST from August 18 and the 1900 to 2200 MST from August 21. The format for these data are the same as in previous figures, except that only three received signal levels are shown, with the 11.4-GHz VH channel replaced by the 96.1-GHz VV channel which was added on August 9. The 28.8-GHz signal was not included because it faded nearly the same amount as the 30.3-GHz signal. These figures show three frequencies attenuated by the same rain. The fade margin for 96.1 GHz is 30 dB and this value is reached several times. At about 1545 MST on August 18, the received signal levels were -9, -20, and -29 dB for 11.4, 30.3, and 96.1 GHz, respectively. These attenuation levels are in the order that would be predicted by rain models (increasing with frequency); however, as suggested in the discussion of Figures 4.19 and 4.20, these values may vary according to the drop-size distribution. The data from August 21 in Figure 4.21 shows three periods of increased attenuation with corresponding periods of high BER. An interesting feature of these data is the sustained higher attenuation observed on the 96.1 GHz channel. Whereas the 30.3 and 11.4-GHz signals tend to recover between showers and after the rain cell has moved through the path, the 96.1-GHz signal is still substantially attenuated. This is mainly due to increased water vapor absorption, a topic discussed further in Section 5.

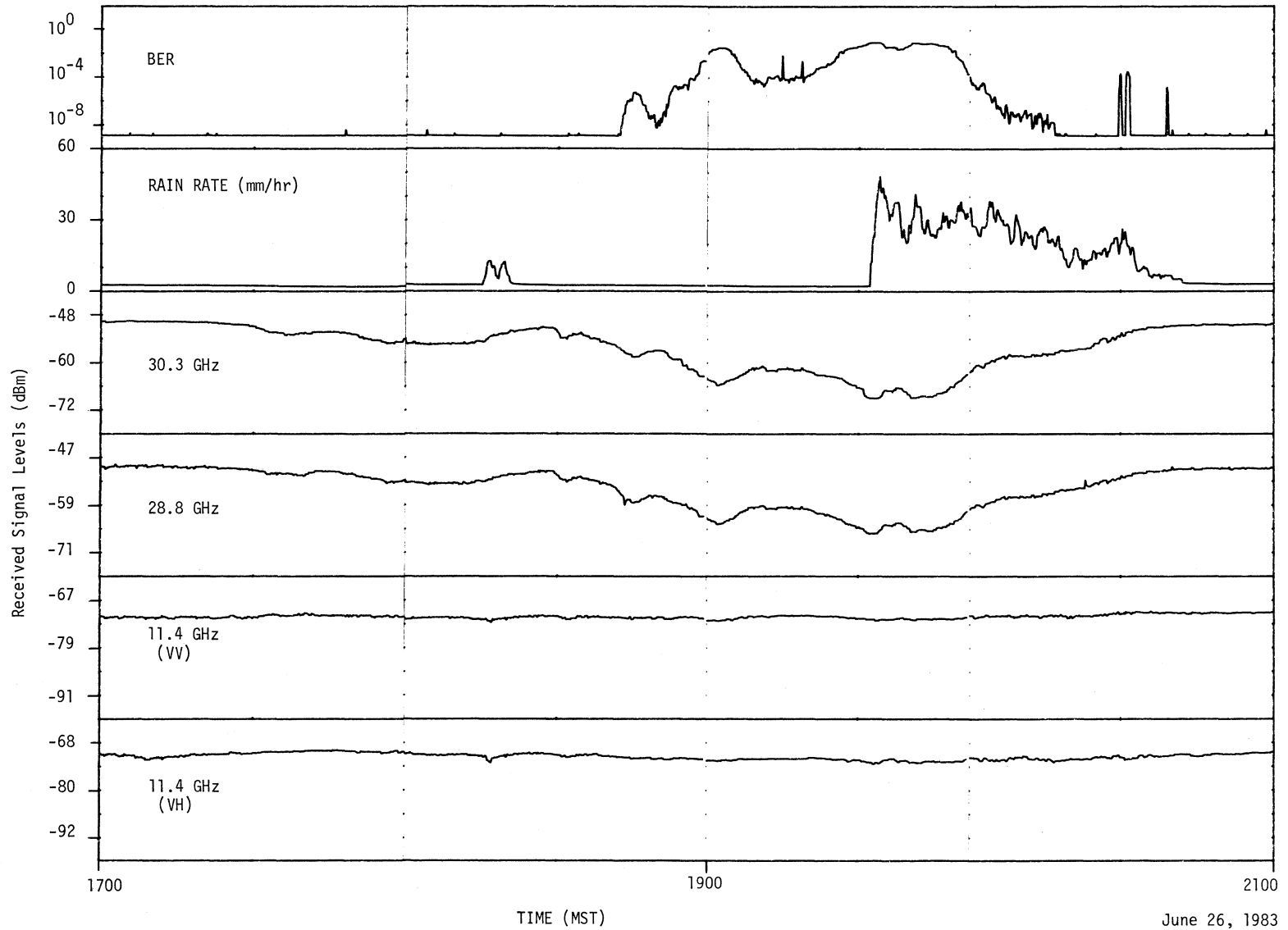


Figure 4.20. Time series records from the 27.2-km path showing results during a rain storm between 1700 and 2100 hours on June 26, 1983.

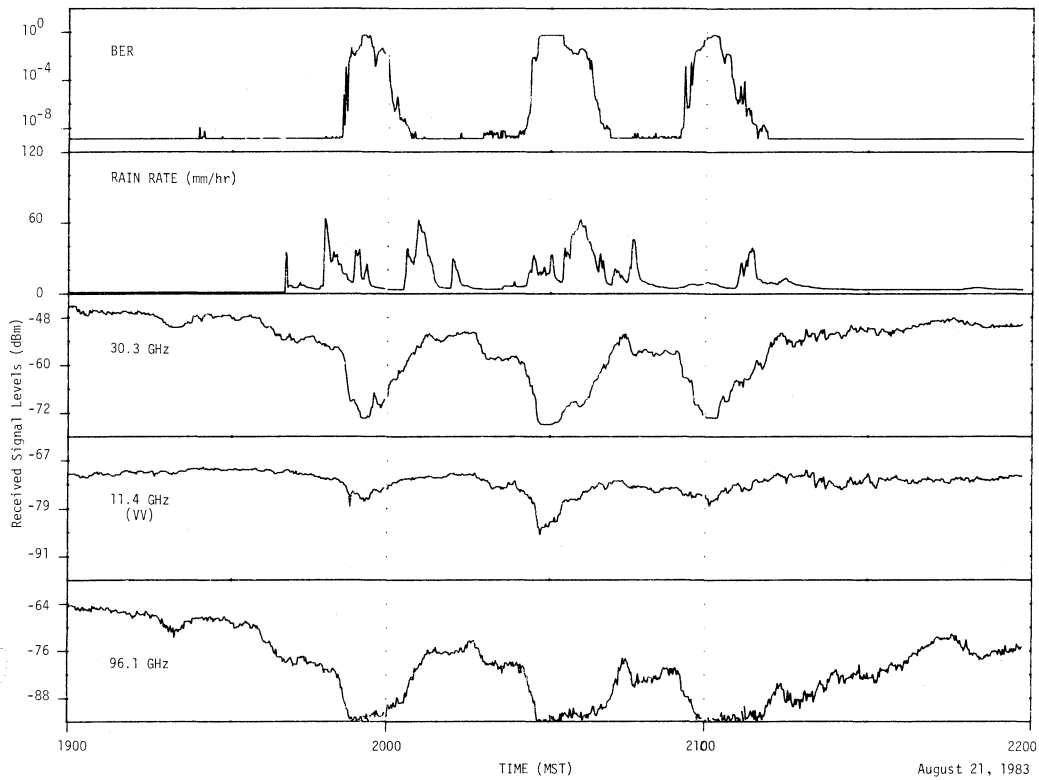
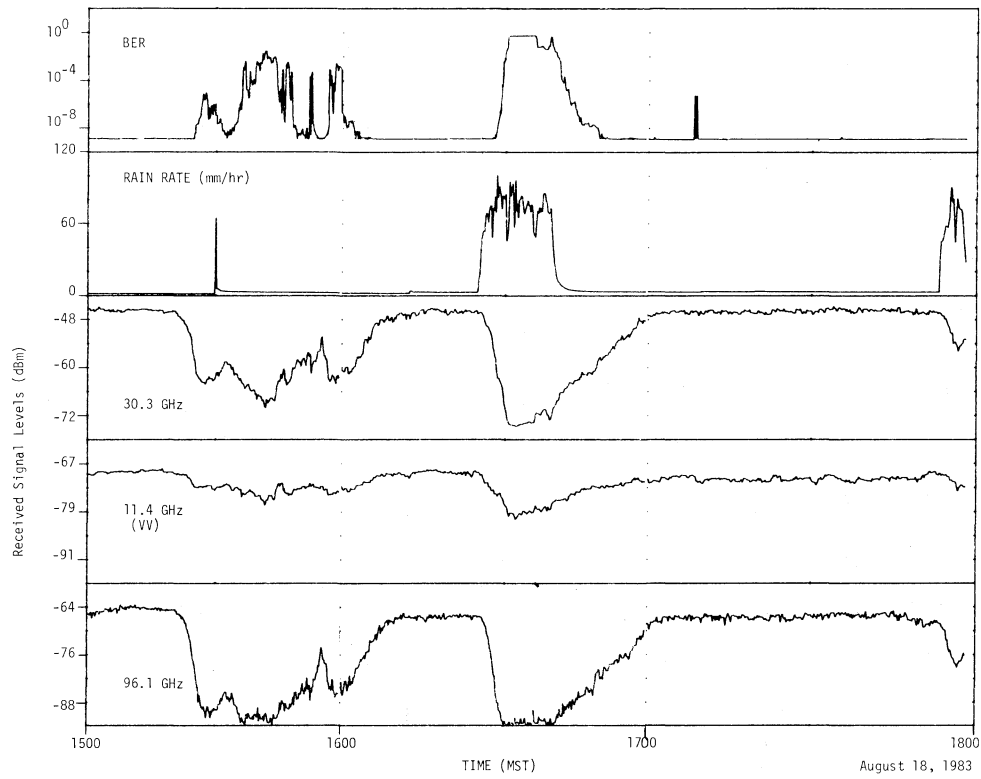


Figure 4.21. Time series segments from the 27.2-km path during rain recorded on August 18 and August 21, 1983.

4.3.3 Multipath Fading

The summer data in Figure 4.14 showed enhanced scintillation and fades compared to the spring data. In the next several figures, examples of some of the deeper fades are shown. Times series records from the 27.2-km path recorded on June 30 and July 6 are shown in Figure 4.22. These data are copied from the computer visual monitor and are of the same format as Figure 4.13 through 4.18. The deepest fades generally occur in the morning hours, quite often near sunrise. These fades are generally of short duration and sometimes have sufficient depth to cause the BER to increase.

The data in Figure 4.23 are reproduced from the 0600 to 0800 MST portion of the June 30 records in Figure 4.22. The upper set of data shows the bit error rate from the 30.3-GHz modulated signal and the received signal levels from the 30.3, 28.8, 11.4 VV, and 11.4 VH-GHz signals. Short-term variations (fades and enhancements) of 20 to 25 dB are noted in the data. At approximately 0645 MST, a fade on the 30.3-GHz channel was sufficient to cause short term bit error up to 1×10^{-2} .

Fades of the type shown above generally result from transmitted rays passing through a region where the dielectric constant or refractive index changes appreciably along the path in either a vertical or horizontal plane or a combination of these. This change in refractive index bends the rays so that two or more rays may arrive at the receiving antenna at different times. If two dominant rays of nearly equal amplitudes and a $\lambda/2$ difference in propagation delay, arrive simultaneously at the receiving antenna, fades of 30 dB or more could occur. Because wavelengths at these frequencies are at most a few centimeters, the delay difference need be only a few tenths of a nanosecond to produce out-of-phase cancellations.

If a delay of 1 or 2 ns were to occur, then intersymbol interference would cause very high BER because the delay time approaches a bit duration (2 ns for the 500 mb/s data rate) (Violette et al., 1983). Delays of one nanosecond or greater generally require ground reflections. The path geometry and the unstable atmosphere in the vicinity of the mountains do not produce the strong, stable stratified layers required for this degree of refractive bending, particularly in the typically dry air of the Colorado climate. Because the amount of ray bending is not frequency dependent, all rays are bent in the same manner and therefore experience the same delays in arriving at the receiver.

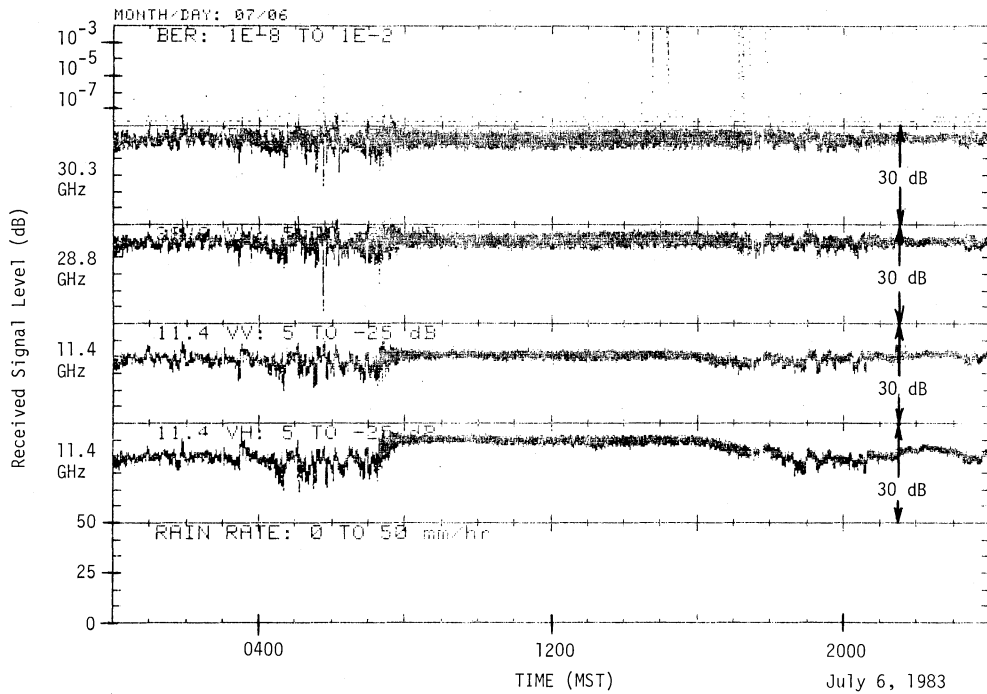
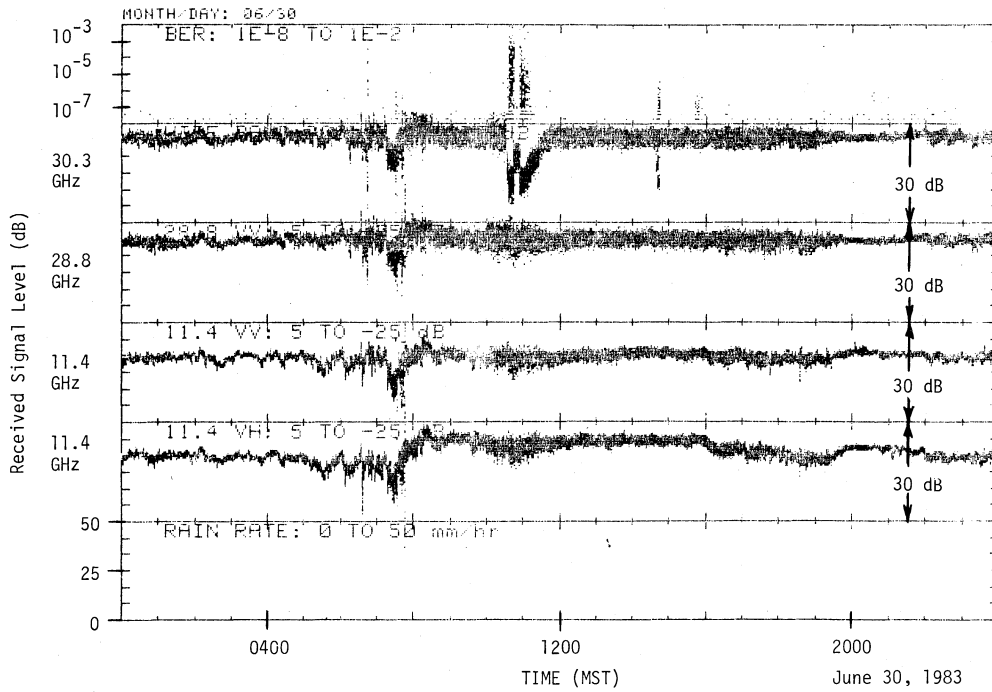


Figure 4.22. Time series records for periods of scintillation and fading on the 27.2-km path recorded on June 30 and July 6, 1983.

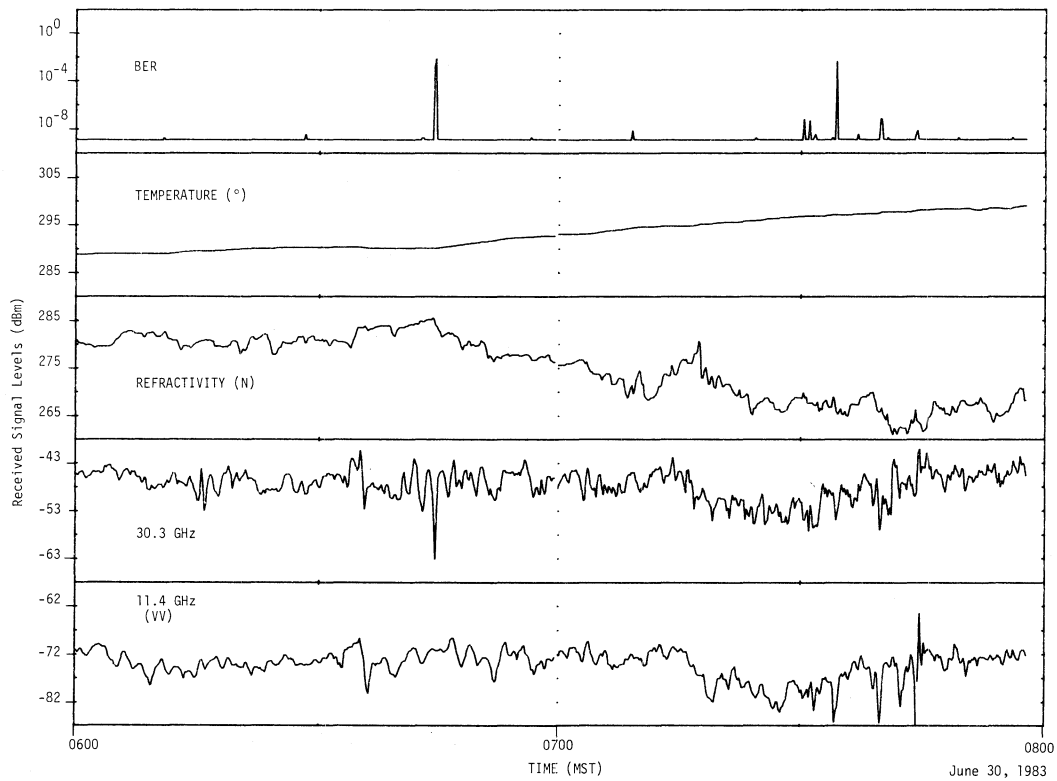
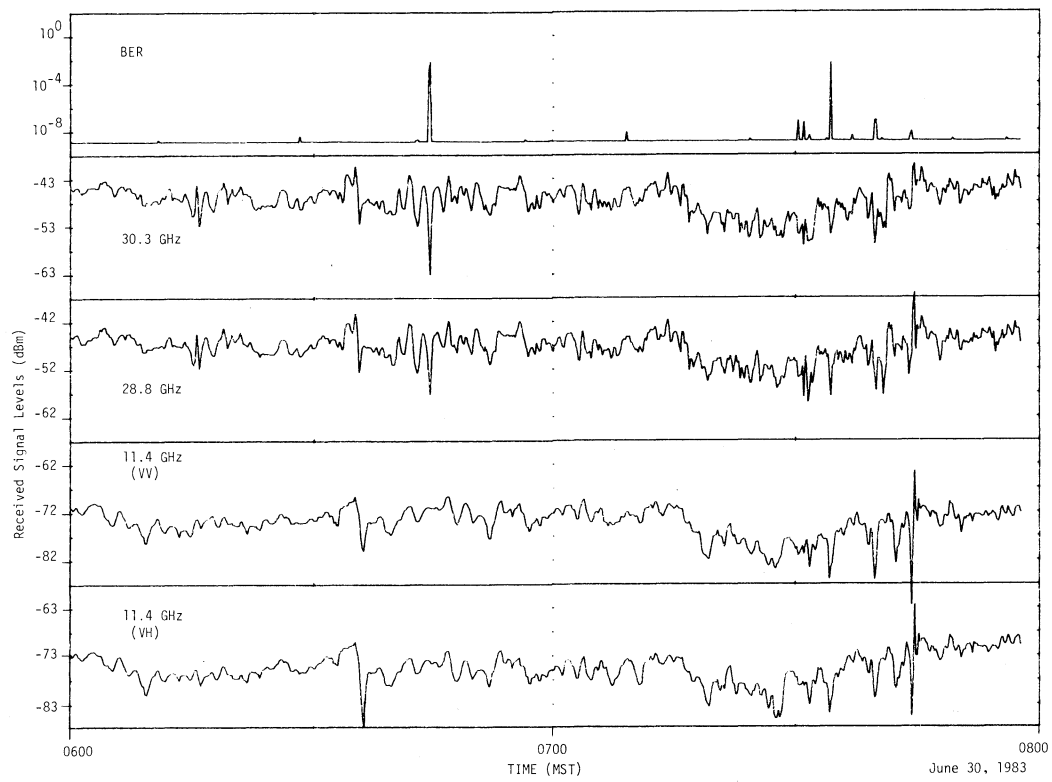


Figure 4.23. Time series segments from the 27.2-km path during periods of fading recorded on June 30, 1983.

One of the variables for measurements in this report is antenna beamwidths and the data show that more multipath opportunities exist for wider antenna beams. A wider beam may admit more multipath components but show shallower fades because a greater number of multipath components will reduce the probability of wave cancellation at the receiver.

Atmospheric multipath fading is characterized by periodicity of fades and enhancements and it has a cyclic period inversely proportional to frequency. In the top data set of Figure 4.23, the well defined fade cycles in the 28.8 and 30.3-GHz data occur much more rapidly than the fade cycles in the 11.4-GHz data. The fade rate ratio between the 30.3 and 11.4-GHz frequencies is 2.66.

The second set of data in Figure 4.23 shows the bit error rate, temperature, refractive index, and RSL at 30.3 and 11.4 GHz. As stated earlier, the meteorological data is recorded only at the receiving terminal and therefore is insufficient to describe the entire 27.2-km path. However, at 0645 MST, a change of slope is noted in the temperature and refractive index profiles that correlate with the multipath activity.

Data from the recordings of July 6 (Figure 4.24) show the multipath fading between 0515 and 0555 hours on July 6 which has characteristics similar to those between 0640 and 0700 hours in Figure 4.23.

Figure 4.25 shows the raw unprocessed data for July 18 in the top data set and 10-s averaged values of the 0100 to 0200 MST portion in the bottom set. These data contain some evidence of multipath, but also an indication of defocusing of the propagated rays. In the time period between 0140 and 0200 MST, all channels fade in a similar manner. This frequency-independent fade is the result of a diverging ray pattern that reduces the ray density at the receiving antenna.

Figures 4.26 and 4.27 show recordings from the 96.1-GHz channel in addition to the 30.3 and 11.4-GHz channels. The top set in Figure 4.26 is non-averaged data for August 12, which highlights the enhanced scintillation of the 96.1-GHz signal compared to the other channels. The 0400 to 0600 MST portion of the August 12 data, with 10-s averaging is shown in the lower data set in Figure 4.26. The magnitude of scintillation is not as evident in the lower recordings because of 10-s averaging. Considerable fading occurs in these data, and the patterns of multipath and beam defocusing fades are apparent by frequency dependent and independent components, even though, their times of occurrence overlap.

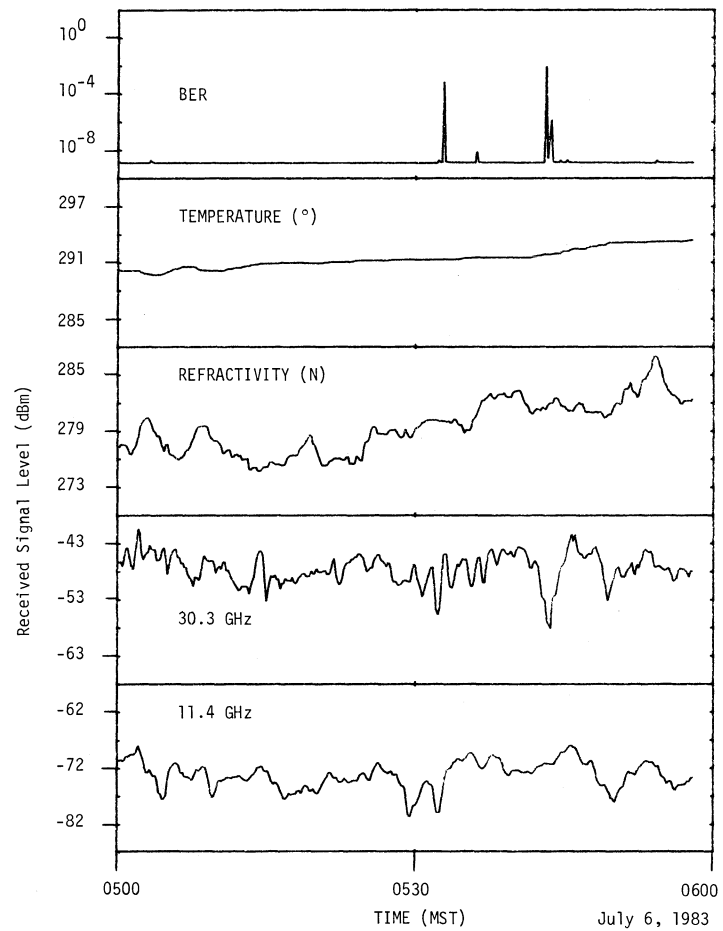
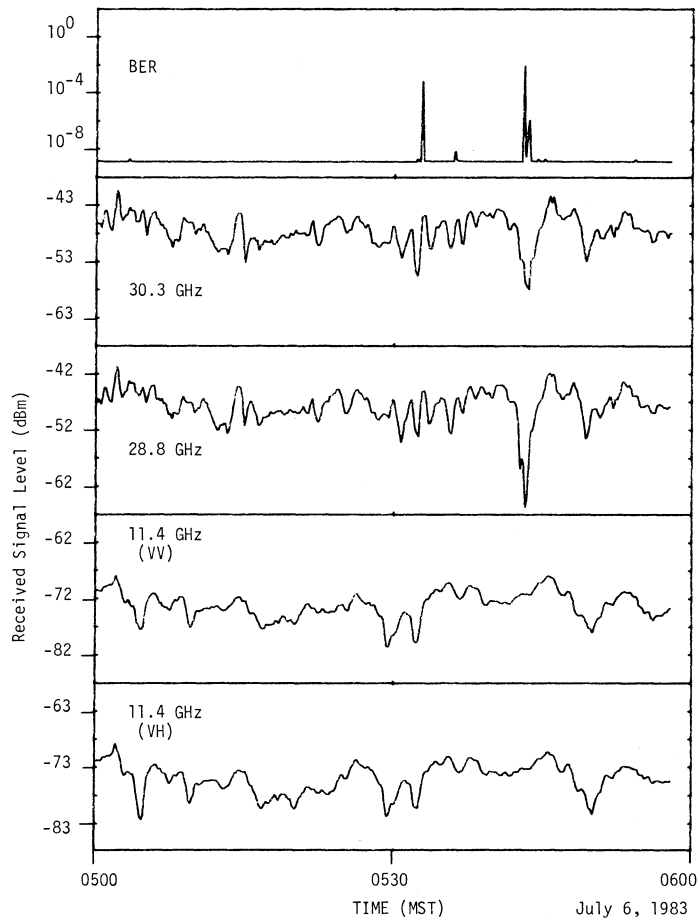


Figure 4.24. Time series segments from the 27.2-km path during periods of fading recorded on July 6, 1983.

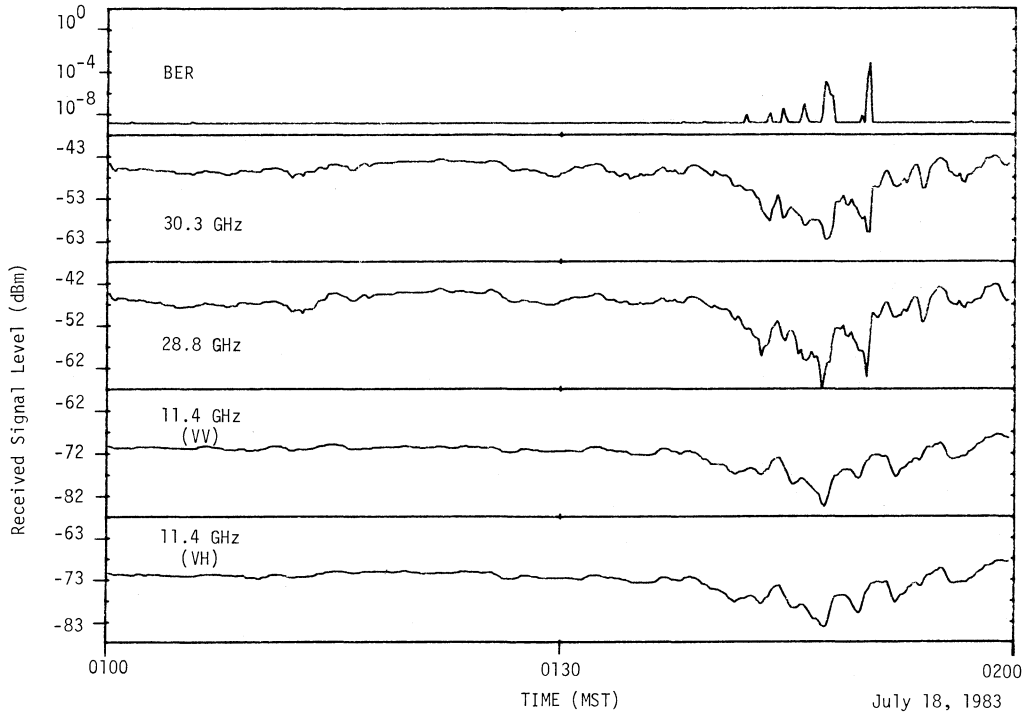
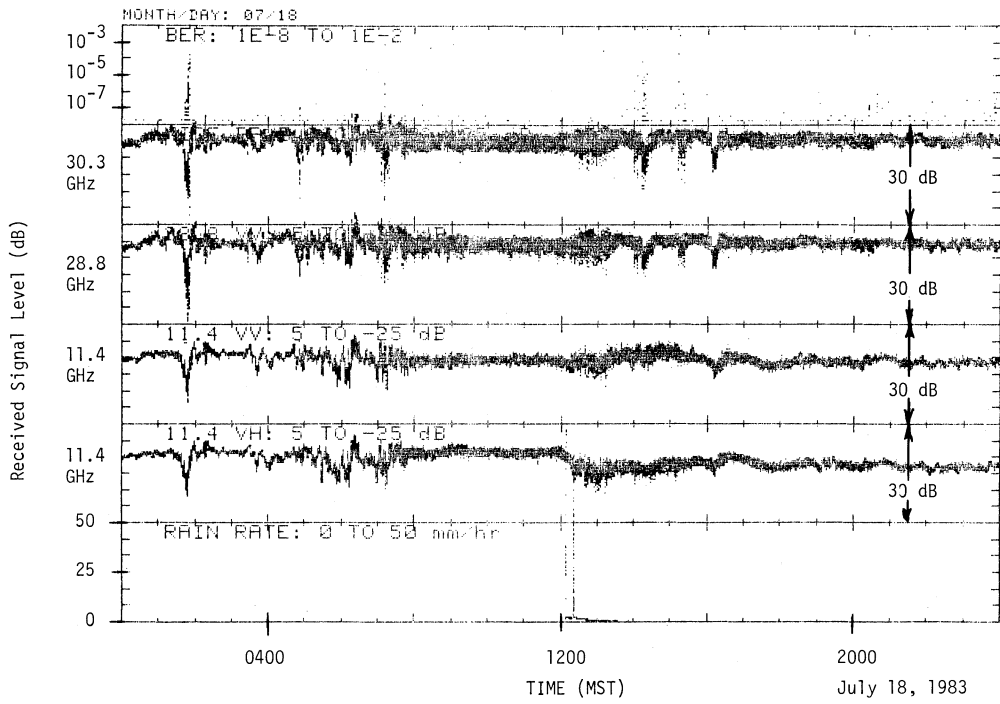


Figure 4.25. Time series records for periods of scintillation and fading on the 27.2-km path recorded on July 18, 1983.

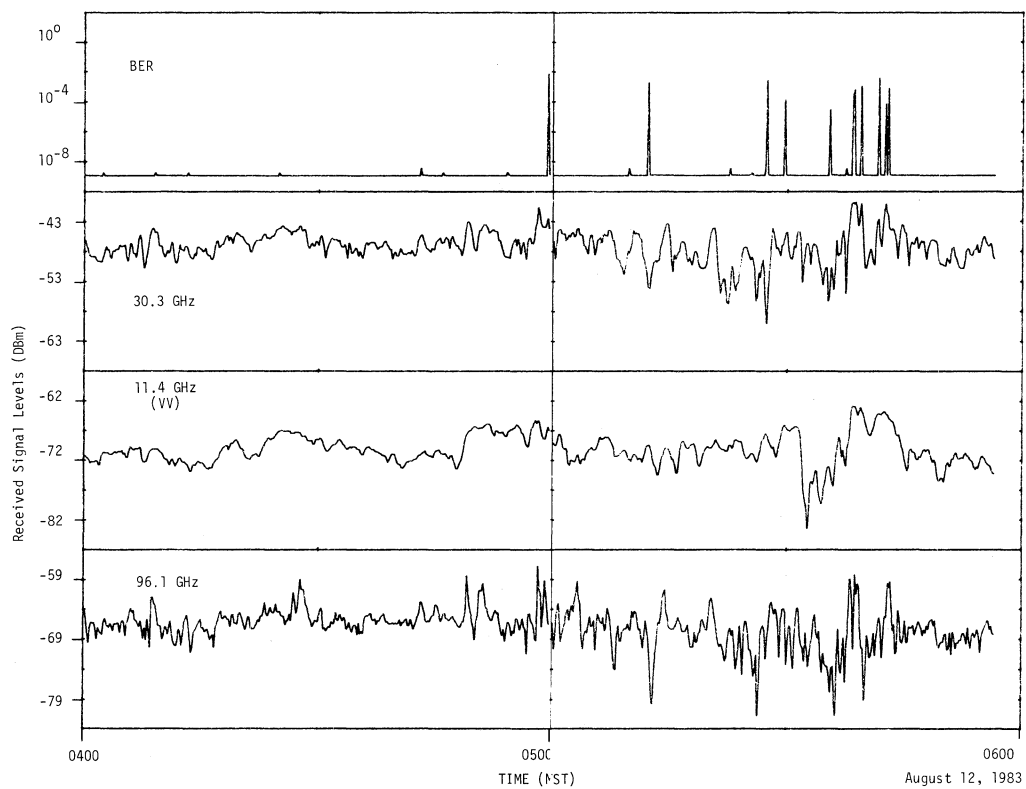
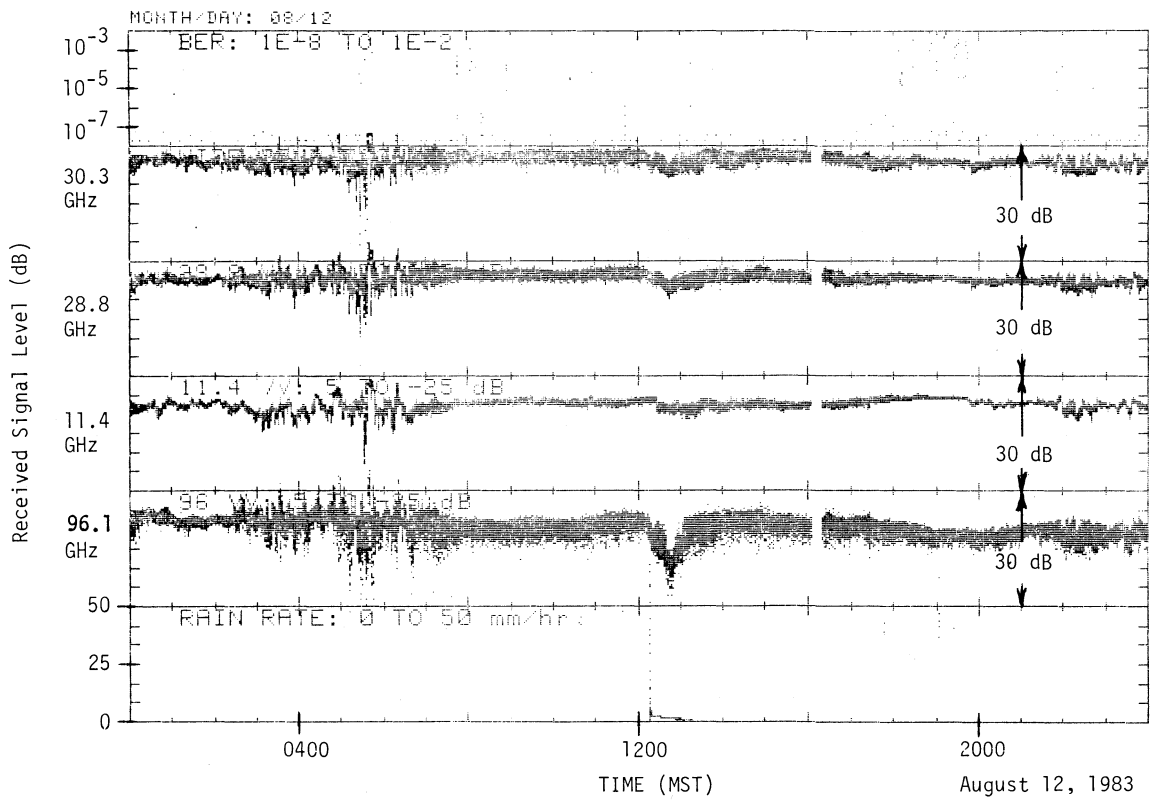


Figure 4.26. Time series records during periods of scintillation and fading on the 27.2-km path recorded on August 12, 1983.

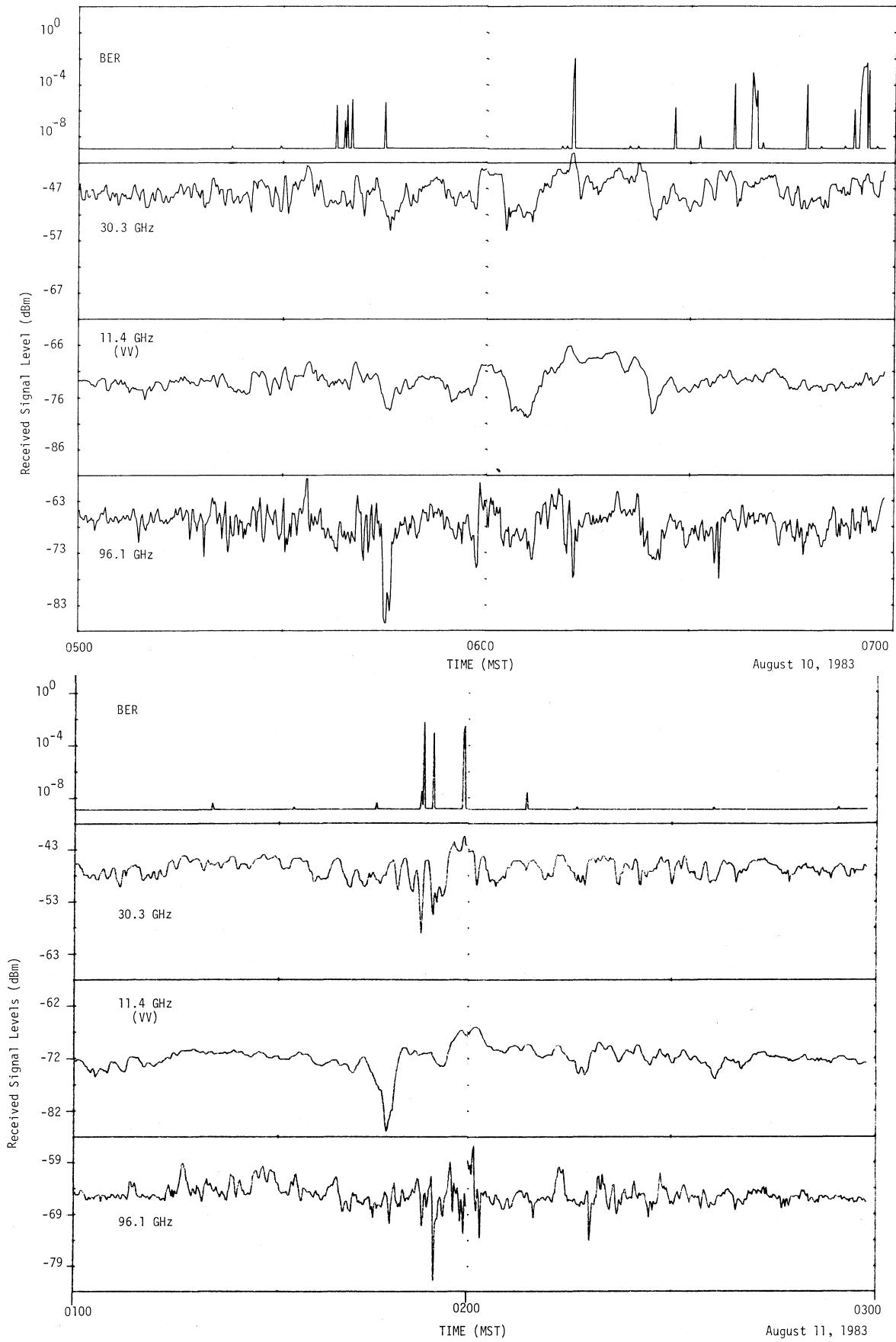


Figure 4.27. Time series segments during periods of fading on the 27.2-km path recorded on August 10 and 11, 1983.

Averaged segments from August 10 and 11 are presented in Figure 4.27. Fading of the order of 10 to 20 dB is observed in these data and evidence of multipath is present at about 0145 to 0200 MST on the 11th of August. Some of the cyclic pattern that might have been present in the 96.1-GHz data may have been lost in the 10-s averaging in the recorded data. Even with the 10-s averaging, which removes the rapid scintillation, depth and numbers of short duration fades (less than 5-min duration) are proportional to frequency, whereas long duration fades (5-min or more) tend to be of more uniform amplitude over a range of channel frequencies. This trend tends to discriminate between the multipath and focusing mechanisms.

The data discussed in this section show short periods of fading and corresponding bit errors associated with the 30.3-GHz channel. Path outages due to clear air fades did not seriously affect the link performance.

4.3.4 Propagation Conditions Analyzed with Impulse Response

As explained in Section 2.3, the data acquisition system was programmed to record impulse response data during times when a potential for channel distortion was indicated by an increase in the BER above a preset level. Many impulse responses were recorded by this mode of operation and many more were recorded by operator command. In this section representative examples of these data are presented for a stable clear-air period, a period of moderate scintillation and fades, and during rain storms.

Figure 4.28 shows the BER and 30.3-GHz received signal level during a stable clear-air period with not more than a decibel of change or scintillation during the hour and only minor bit-error bursts. Selected impulse response curves are shown in Figure 4.29 corresponding to the times indicated in Figure 4.28. These curves are similar to the impulse response curve recorded on the 11.8-km test path shown in Figure 4.4a (Section 4), which was also recorded during a stable and quiet period for which there was no evidence of multipath. The data in Figure 4.29 likewise shows no presence of multipath. An indication of multipath components would be evident in a broadening of the impulse response curve on the trailing edge, such as observed in Figures 4.4b and Figure 4.5.

The leading edges of curves 4.29a and 4.29b (at a level of -27 dB) are generated by excess clock-drive levels in addition to an in-band harmonic of the variable offset clock. This leading edge step has not occurred often and does not mask data because all time delay distortion trails the direct signal.

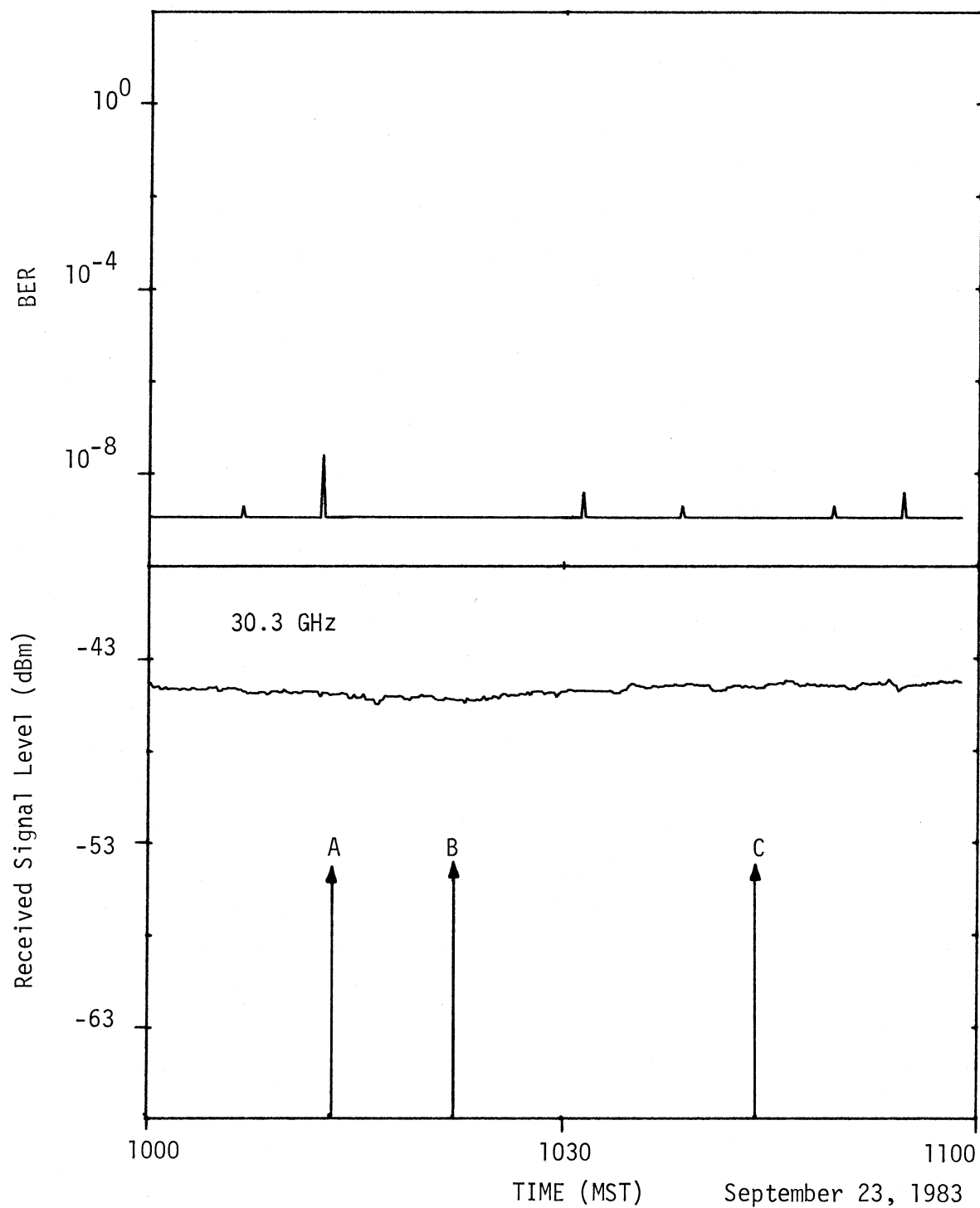


Figure 4.28. A time series of BER and the received signal level at 30.3 GHz recorded September 23, 1983 between 1000 and 1100 on the 27.2-km path.

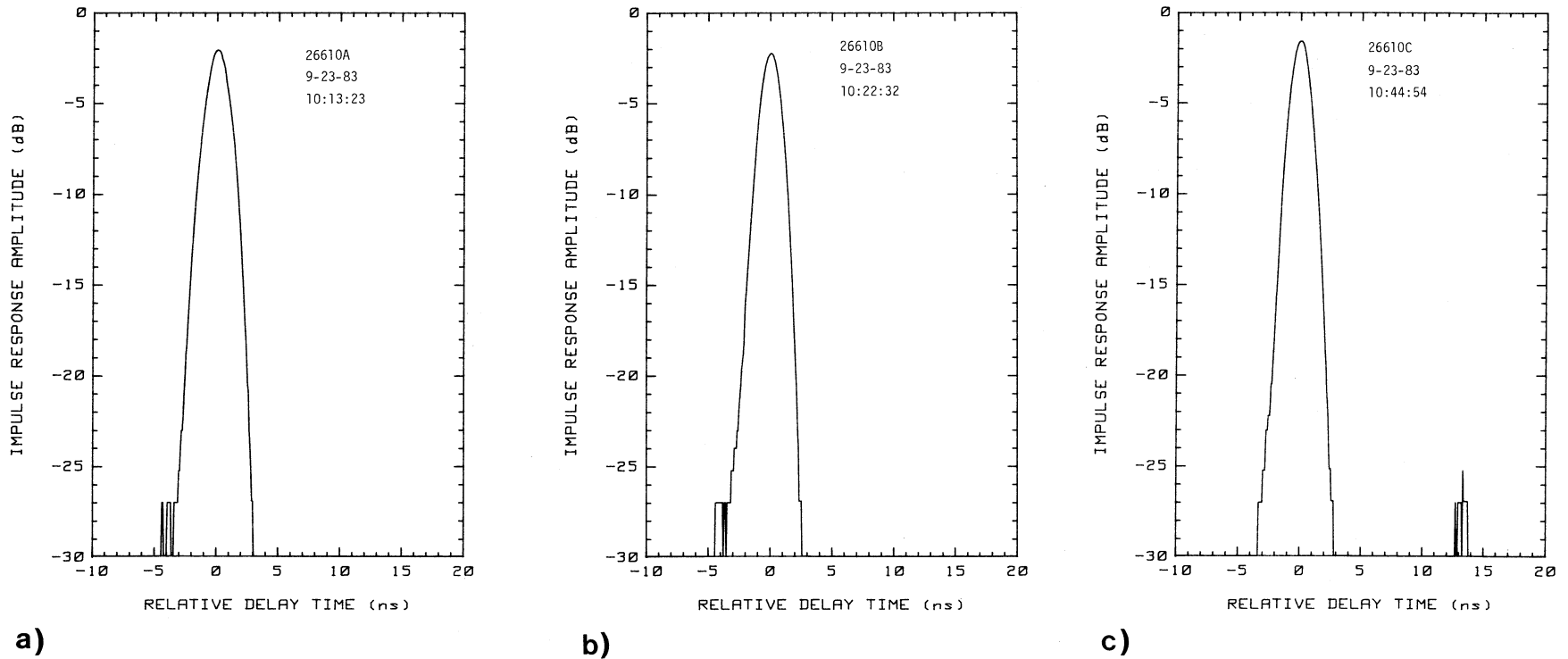


Figure 4.29. Selected impulse response curves recorded from the 27.2-km path between the hours of 1000 and 1100 on September 23, 1983.

The spurious response occurring at a delay of about 13 ns with an amplitude of -26 dB (4.29c) is the result of slight nonsymmetry in the pseudo-random data generator. This spurious response can be removed by a balance adjustment but may drift in amplitude with temperature change as well as with the relative strength of the received signal or peak value of the impulse response. Its position is always the same which would permit a cancellation with additional processing.

The data in Figure 4.30 shows the BER and received signal level of the 30.3-GHz channel during a period of moderate scintillation and fading. Approximately 10 dB level changes are observed. Figure 4.31 shows two impulse response curves recorded at the times indicated in Figure 4.30. These two impulse response curves were manually triggered. The increased noise level in 4.31b as compared to 4.31a resulted from a manual adjustment of the dc bias control by the operator between the recordings of 4.31a and 4.31b. In these curves as in others there is no indication of significant multipath, an observation supported by the absence of bit errors.

The third set of data presented in this section was recorded during rain on the 27.2 km path. The time series of the 30.3-GHz received signal levels and BER (Figure 4.32) show, respectively, a decrease in signal level due to the rain and an increase in the BER due to a reduced S/N. The impulse response curves of Figure 4.33 were recorded during the rain at the times indicated in Figure 4.32. In these curves, there appears to be no indication of a time delay spread due to forward scattering from raindrops. The reduced peak amplitude in Figure 4.33d corresponds to the reduced signal level in Figure 4.32 at the time this impulse response curve was recorded. The strong inverse correlation between the BER and received signal level in Figure 4.32 is also an indication that the bit errors are primarily due to the signal-to-noise ratio at the demodulator.

The data presented in this section indicate that the 27.2-km line-of-sight path on which the data were recorded did not produce multipath signals of sufficient amplitude or delay to cause intersymbol interference as evidenced by the BER and the impulse response data. The increased BER in the multipath examples shown in Section 4.33 is due primarily to a decrease in signal-to-noise ratio caused by a rain fade.

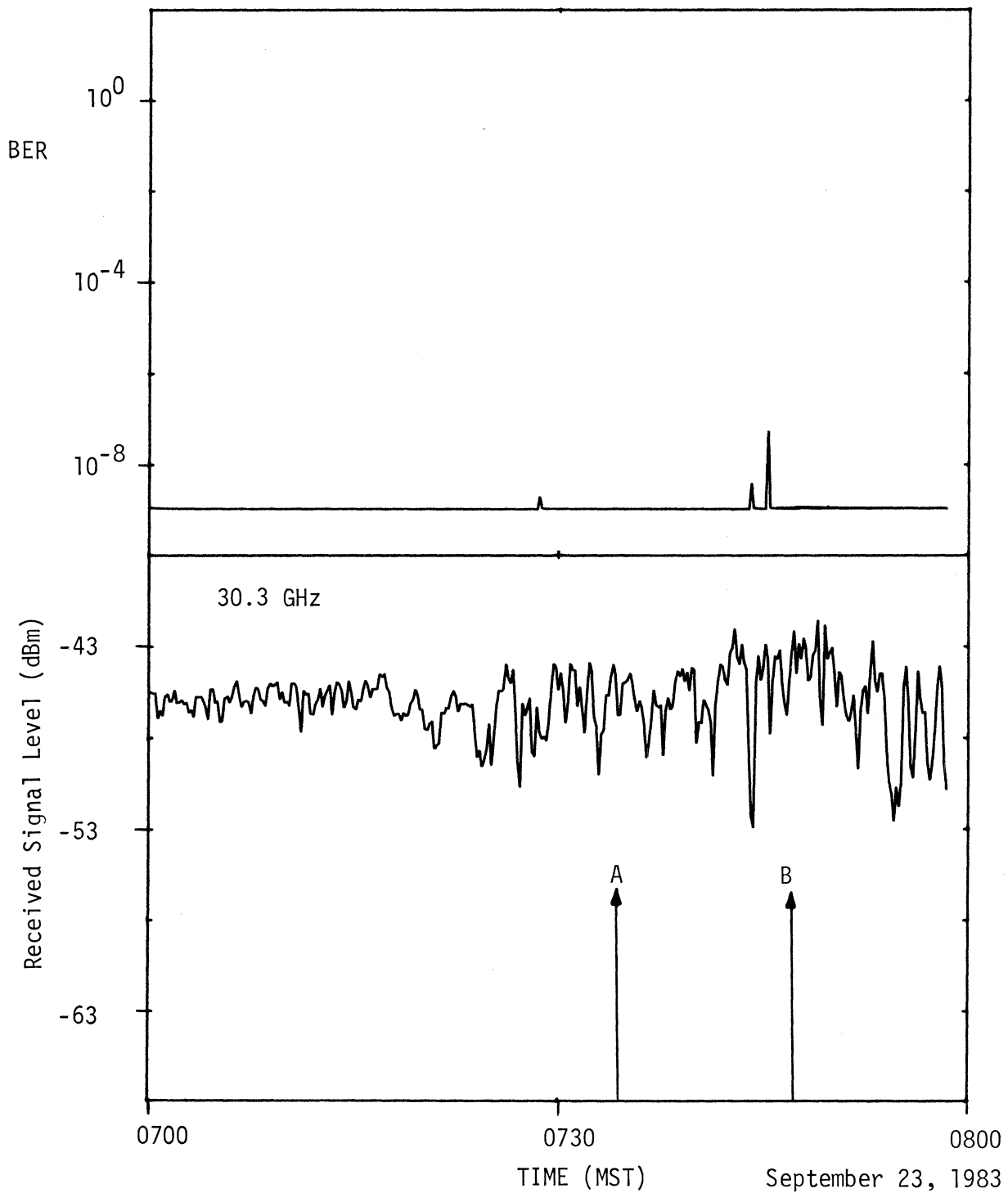


Figure 4.30. A time series of BER and 30.3 GHz received signals recorded on the 27.2-km path during a period of moderate scintillation, 0700 to 0800 on September 23, 1983.

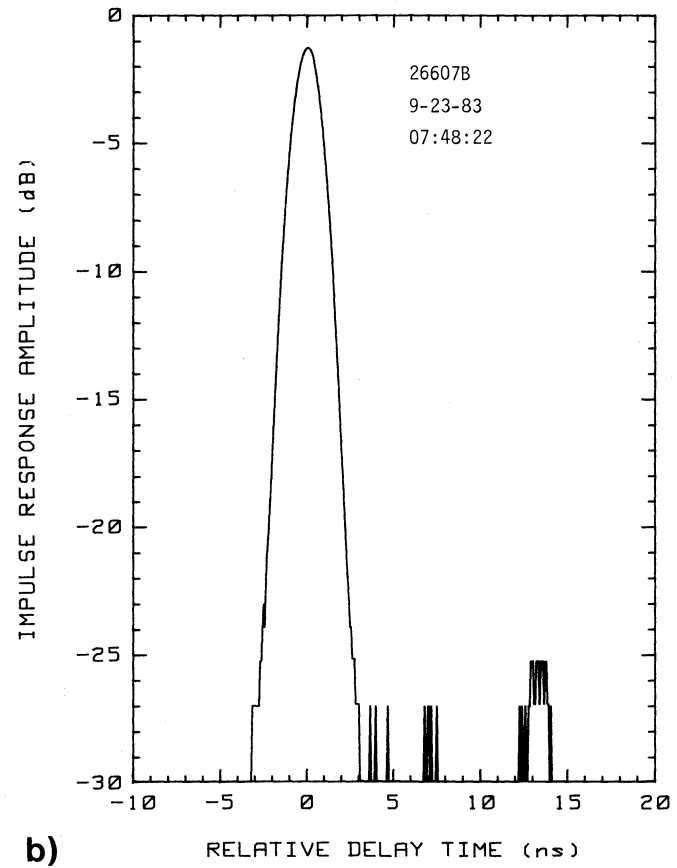
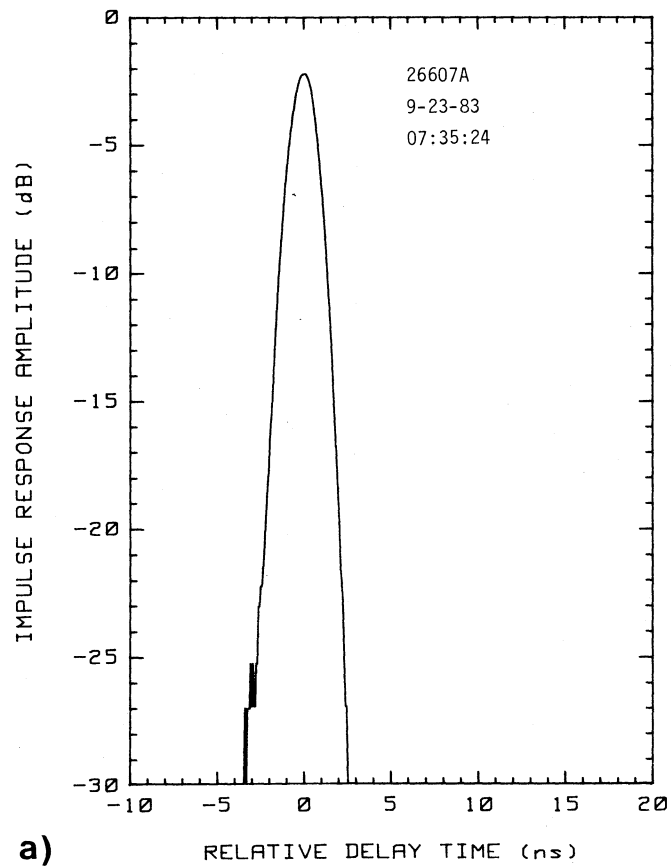


Figure 4.31. Selected impulse response curves recorded from the 27.2-km path between 0700 and 0800 hours on September 23, 1983.

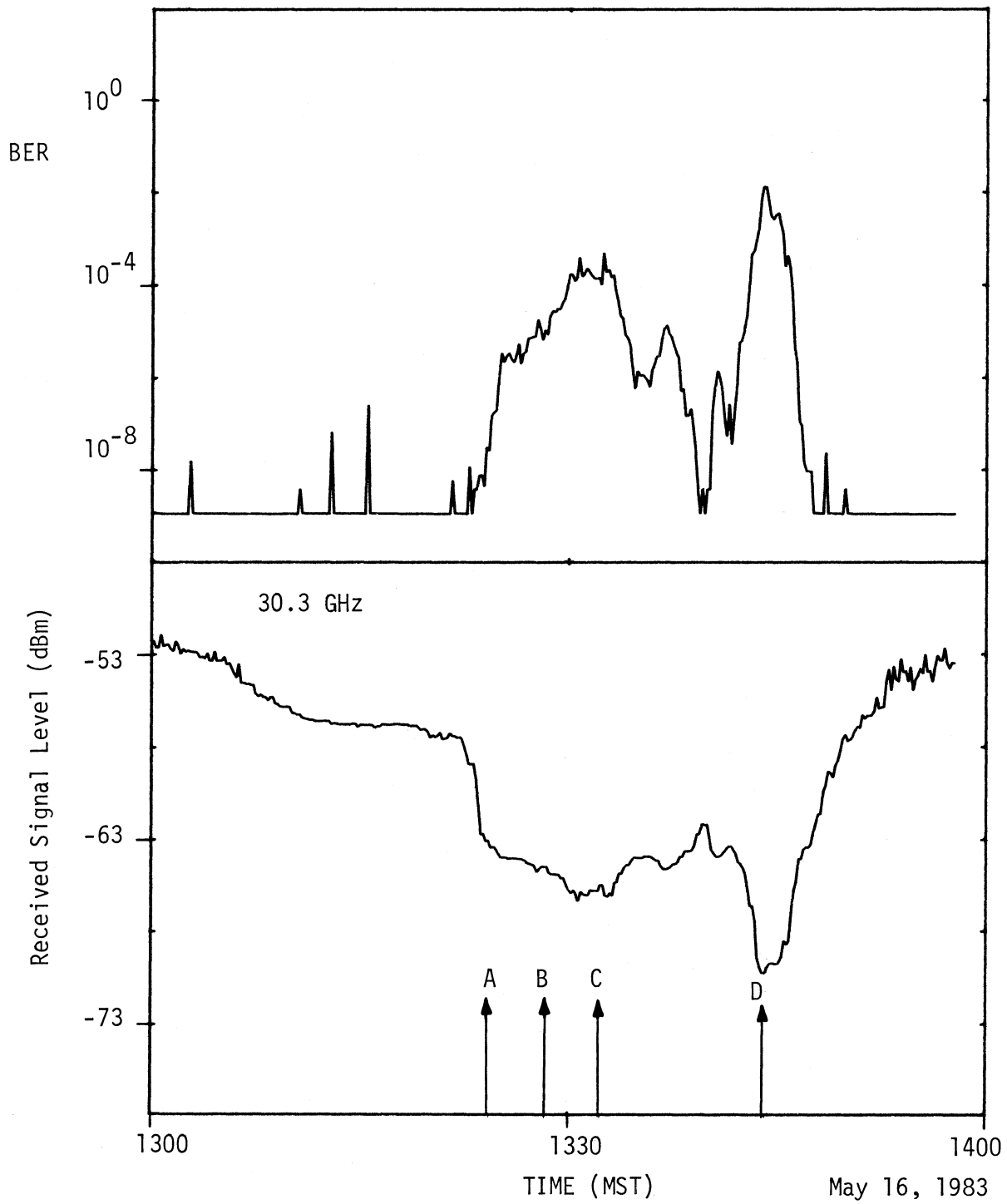


Figure 4.32. A time series of BER and the received signal levels of 30.3 GHz recorded during rain on the 27.2-km path, May 16, 1983.

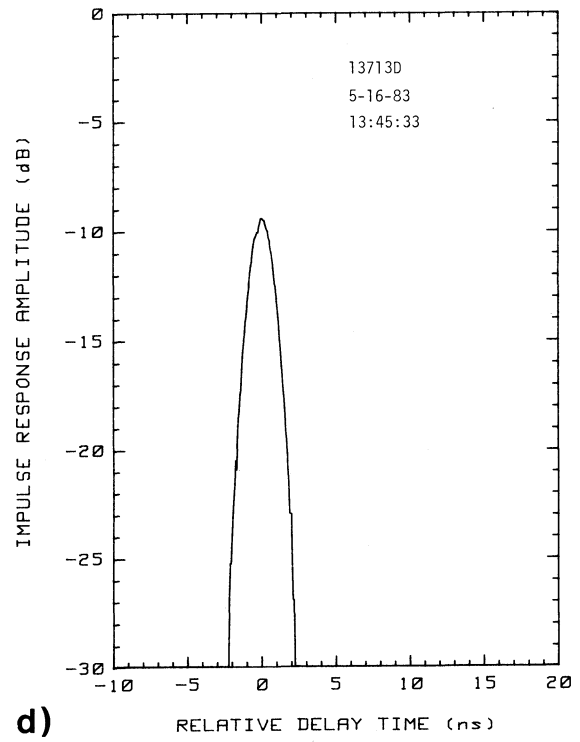
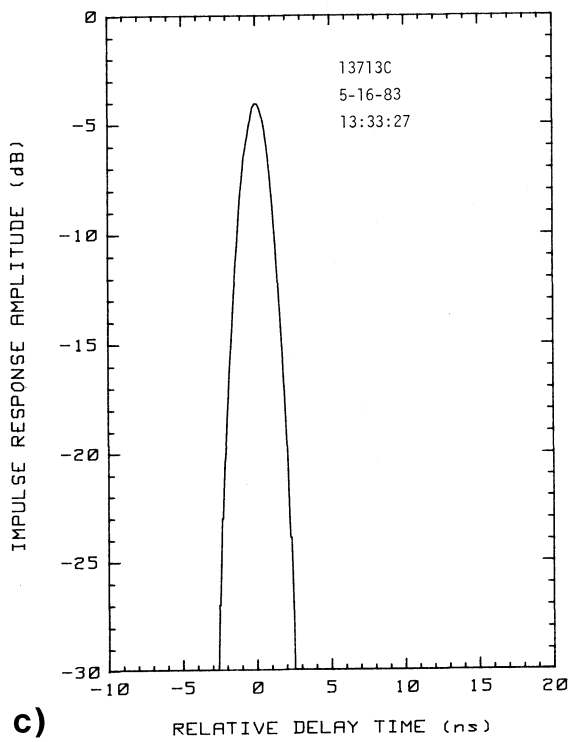
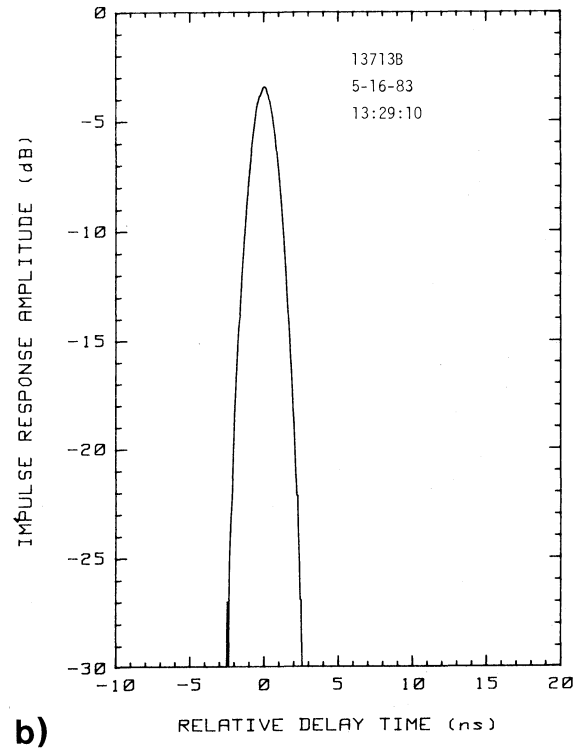
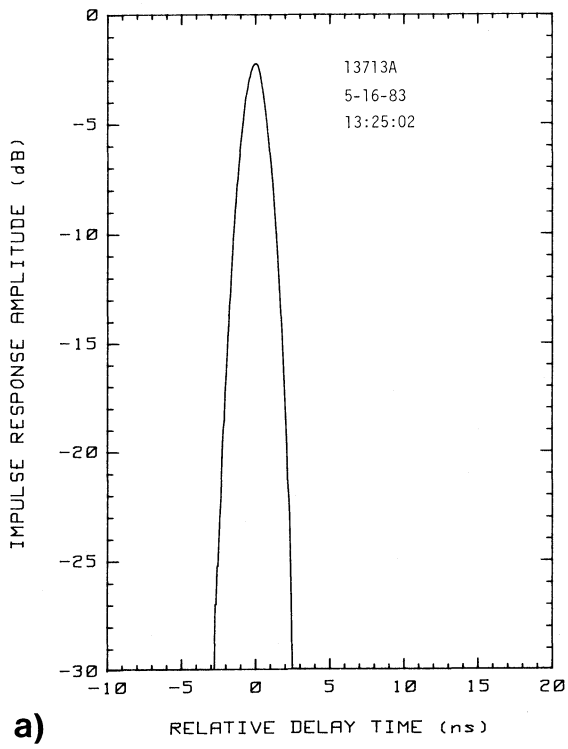


Figure 4.33. Selected impulse response curves recorded during a period of rain on the 27.2-km path, May 16, 1983.

5. STATISTICAL ANALYSES

5.1 Rain Attenuation

In this section, the frequency dependence of attenuation due to rain is studied. The data presented are important since they can be used to predict the performance of communication links near 30 GHz by scaling from data available from links that have been operating near 11 GHz for a number of years. The data also support analyses for determination of the drop-size distribution of rain. The drop-size distribution is a significant factor in the ability to predict rain attenuation distributions for millimeter waves. Drop-size distributions that have proved adequate for predicting attenuation at lower microwave frequencies may not give accurate predictions at higher frequencies where the wavelength approaches the diameter of the raindrops. Before the data is presented some elementary theoretical background is given.

The attenuation A experienced by a radio wave traveling a distance L over a rainy path is given in the classical manner by

$$A = \int_0^L \alpha(\ell) d\ell \quad (5.1)$$

where $\alpha(\ell)$ is the specific attenuation in dB/km along the path (Kerr, 1951). The specific attenuation is usually modeled as

$$\alpha = a R^b \quad (5.2)$$

where R is the rain rate in mm/h and a and b are parameters determined by the raindrop-size distribution and the radio frequency. Choosing any one of a number of popular raindrop-size distributions, gives

$$A = a(f) \int_0^L R(\ell)^{b(f)} d\ell \quad (5.3)$$

where the dependence of the rain rate on position along the path and the dependence of the a and b parameters on frequency f have been emphasized. From (5.3) it can be seen that the ratio of attenuation at two different frequencies [in particular $b(f_1) \neq b(f_2)$] involves the ratio of two integrals. Thus the ratio of attenuation depends not only on the raindrop-size distribution chosen but also on the distribution of the rain rate along the path.

A simplifying assumption is now made to facilitate the evaluation of the ratio of attenuation. The rain rate is assumed to be constant over a portion of the path and zero elsewhere. The length of the interval over which the rain rate is nonzero is called the rainy path length, denoted ℓ_R . With this assumption (5.3) becomes

$$A = a(f) R^{b(f)} \ell_R \quad (5.4)$$

and the ratio of attenuation at frequencies f_1 and f_2 becomes

$$A(f_2)/A(f_1) = \frac{a(f_2)}{a(f_1)} R^{b(f_2)-b(f_1)} \quad (5.5)$$

Although the assumption of a constant rain rate over a portion of the path seems restrictive and idealized, it is very useful. Any real distribution of rain rate along the path could be approximated arbitrarily closely by a step-wise constant function, for which the attenuation would be given by a sum of terms of the form in (5.4). Thus the range of ratios represented by (5.5) completely covers the range of realistic ratios possible for any given raindrop-size distribution model.

In Table 1, the a and b parameters for 11.4 and 28.8 GHz and various raindrop-size distributions are given. These values are interpolated from the table given by Olsen et al. (1978) for 0 deg C.

Table 1
Parameters a and b for 0 deg C

<u>Distribution</u>	11.4 GHz		28.8 GHz	
	<u>a</u>	<u>b</u>	<u>a</u>	<u>b</u>
Laws and Parson, low rain rate	0.0164	1.167	0.148	1.069
Laws and Parson, high rain rate	0.0170	1.160	0.203	0.936
Marshal-Palmer	0.0190	1.140	0.170	1.023
Joss et al., thunderstorm	0.0232	1.060	0.250	0.807
Joss et al., drizzle	0.0153	0.980	0.118	1.048

With these parameter values, the ratio of attenuation has been computed using (5.5) for various rain rates and the results are presented in Table 2.

Table 2

Ratio of attenuation at 28.8 GHz to that of 11.4 GHz
for various rain drop-size distributions and rain rates

<u>Distribution</u>	<u>Rain rate (mm/h)</u>			
	<u>1</u>	<u>10</u>	<u>100</u>	<u>200</u>
Laws and Parsons, low rain rate	9.02	7.20	5.74	5.37
Laws and Parsons, high rain rate	11.94	7.13	4.26	3.64
Marshall-Palmer	8.95	6.84	5.22	4.82
Joss et al., thunderstorm	10.78	6.02	3.36	2.82
Joss et al., drizzle	7.71	9.02	---	---

Ratios even larger than those presented in the table are possible for rain rates less than 1 mm/h, but at such rain rates the attenuation would be very small. Ratios smaller than those in the table are possible at rain rates greater than 200 mm/h but such rain rates are very rare and probably would not occur on a path without other smaller rain rates also occurring simultaneously on the path. Thus one would expect ratios between about 6 and 9 to be most common.

The measurement of the ratio of attenuation due to rain can be difficult. The time series of a fading event due to precipitation is presented in Figure 5.1. (These data are also discussed in Section 4.3.2.) As is indicated in the figure by the decrease in the 28.8-GHz signal level, rain began to occur on the path near 0100 MST on March 15, 1983. This rain turned into snow and it snowed vigorously for the next 12 hours. Little attenuation was observed after 0410 MST as was usually observed during times of snowfall on this path. It is therefore assumed that between 0300 and 0400 MST the rain was turning into snow along the path as the signal levels were recovering. In order to determine the ratio of the attenuation at 28.8 GHz and 11.4 GHz, unattenuated reference signal levels must be determined. But as can be seen in Figure 5.1, the signal amplitude varied before the fade and returned to different levels afterwards so that an accurate measure of the amount of attenuation due to the precipitation seems impossible. Even if reference signal levels could be determined for individual rain events the ratio of the attenuation would be expected to vary throughout the event. In Figure 5.1 it is apparent that the ratio is different before and after 0300 MST.

Cross-plots of the signal amplitudes have proven very useful in overcoming these difficulties. In Figure 5.2 a cross-plot is presented of the data from 0100 to 0500 MST of Figure 5.1. The initial fading and recovery of the signal

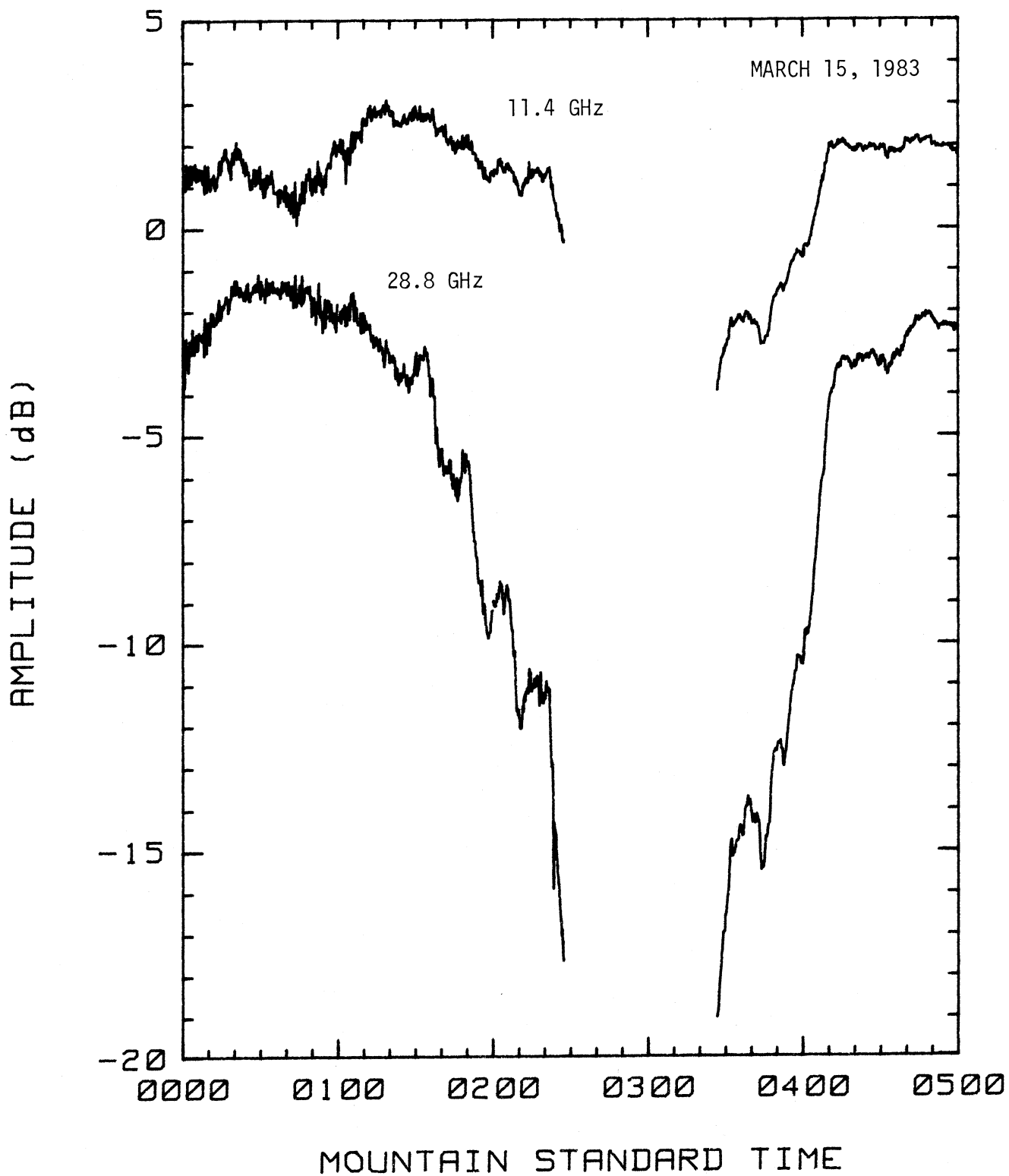


Figure 5.1. A time series record of 11.4 and 28.8-GHz signals recorded during periods of rain and snow on the 27.2-km path on March 15, 1983.

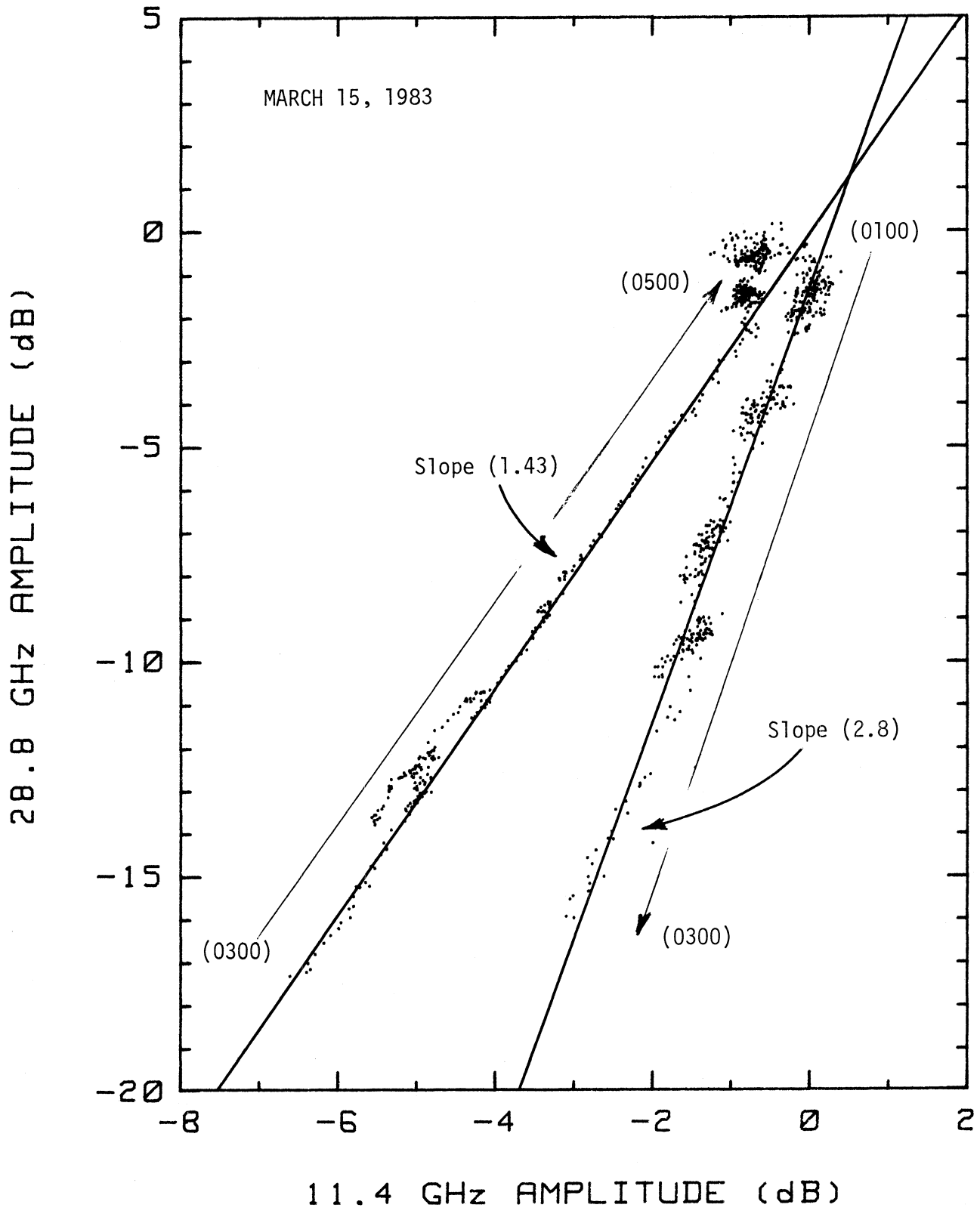


Figure 5.2. A cross-plot of 28.8 and 11.4 GHz signal amplitudes recorded between 0100 and 0500 MST, March 15, 1983.

amplitudes are clearly visible in the figure. The signal amplitudes have been arbitrarily offset for convenience of presentation. The most striking feature of Figure 5.2 is the linear relationships of the signal amplitudes as the signal levels decrease and increase in tandem. This feature consistently reoccurred in the cross-plots of rain events from March through July of 1983. These nearly straight-line features must intuitively be closely related to the ratio of attenuation. If a point near the top of one of these features is used to determine the reference levels for measuring the attenuation, then all the points on the line would have the same ratio of attenuation. With this interpretation, it is no longer necessary to select unattenuated reference levels to determine the ratio of attenuation. That is, Figure 5.2 indicates that before 0300 MST the ratio of attenuation was consistently one value and after 0300 MST it was consistently a different value. The transition between the two values occurred during the time for which the data are missing. It is a convenient aspect of Figure 5.2 that the slope of the two linear features represent the ratio of attenuation.

The linear pattern in the cross-plots is surprising in consideration of the form of (5.5), which shows that the ratio of attenuation is a power function of the rain rate. One is led immediately to ask why a linear relationship in signal amplitude is maintained as the signals fade. Or more directly, what kind of change is occurring along the path in the rain rate and/or rainy path length? Thus the kind of cross-plots produced by the model developed above were investigated.

In Figure 5.3 and 5.4 cross-plots of signal levels predicted by the model using a Laws and Parsons, low rain rate drop-size distribution are presented. In Figure 5.3 the rain rate was assumed to be constant (either 1, 10, or 100 mm/h) and the rainy path length was varied from 0 to 27.2 km. The resulting fades in the cross-plot are straight lines that have slopes determined by the rain rate, a result consistent with (5.5). In Figure 5.4 the rainy path length was assumed to be constant (either 1, 10, or 27.2 km) and the rain rate was varied from 0 to 150 mm/h. The cross-plots, while not straight lines, are nearly linear and have slopes determined by the rainy path length.

Thus nearly constant slopes in the cross-plots of the observed rain events is consistent with the model. Since these nearly linear features contain most of the data during fading events, their slopes estimate a majority of the attenuation ratios observed, i.e., they are a convenient and good measure of attenuation ratios.

From the precipitation events observed during March through July 1983, 114 ratios of attenuation at 28.8 GHz and 11.4 GHz were estimated by measuring the slopes of lines fit by visual inspection to fades in the cross-plots. These data

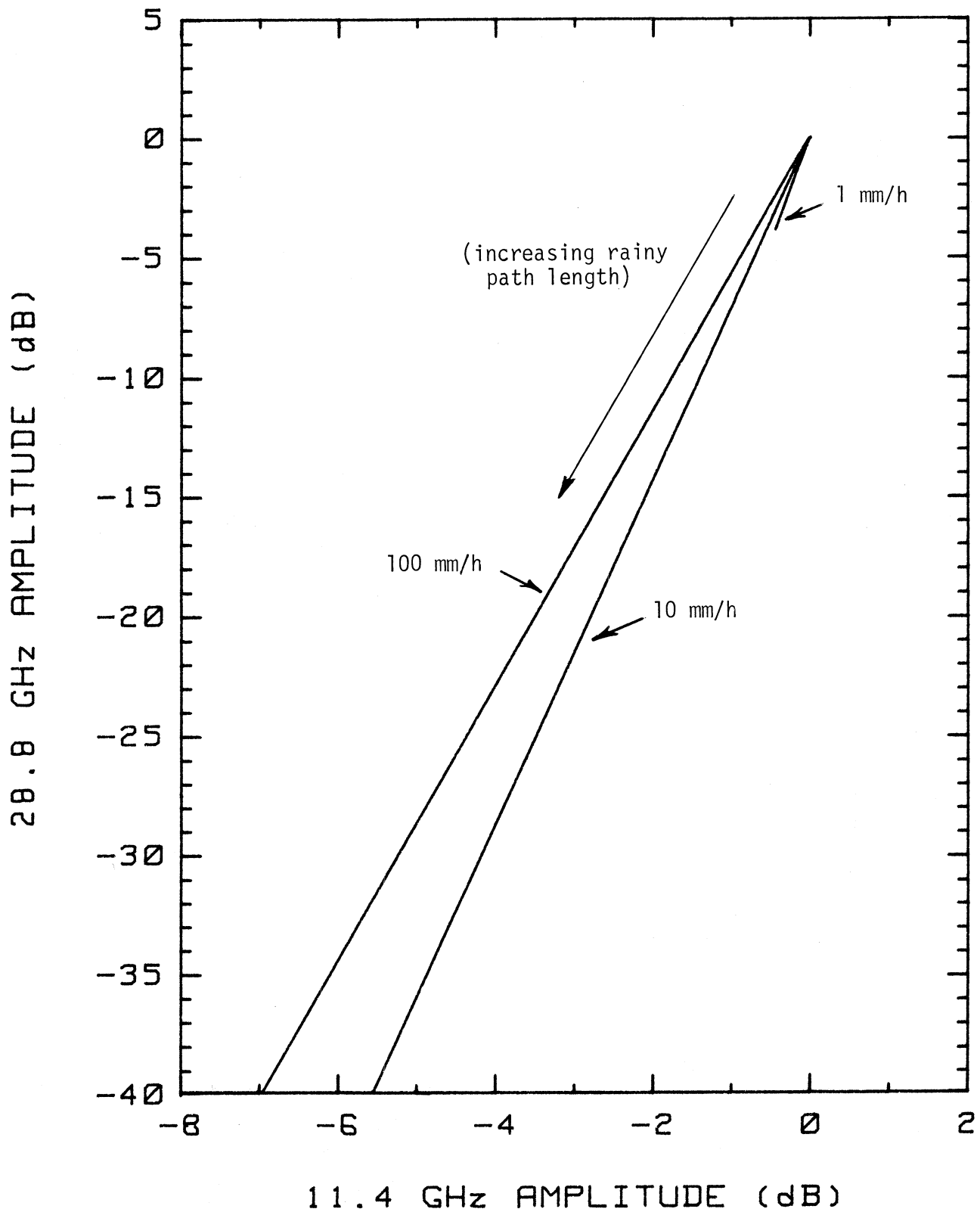


Figure 5.3. Signal amplitude at 28.8 and 11.4 GHz for rain rates of 1, 10, and 100 mm/h as the rainy path length is varied from 0 to 27.2-km. Attenuation predicted using (5.4) with the a and b parameters of Table 1 for the Laws and Parson's, low rain rate distribution.

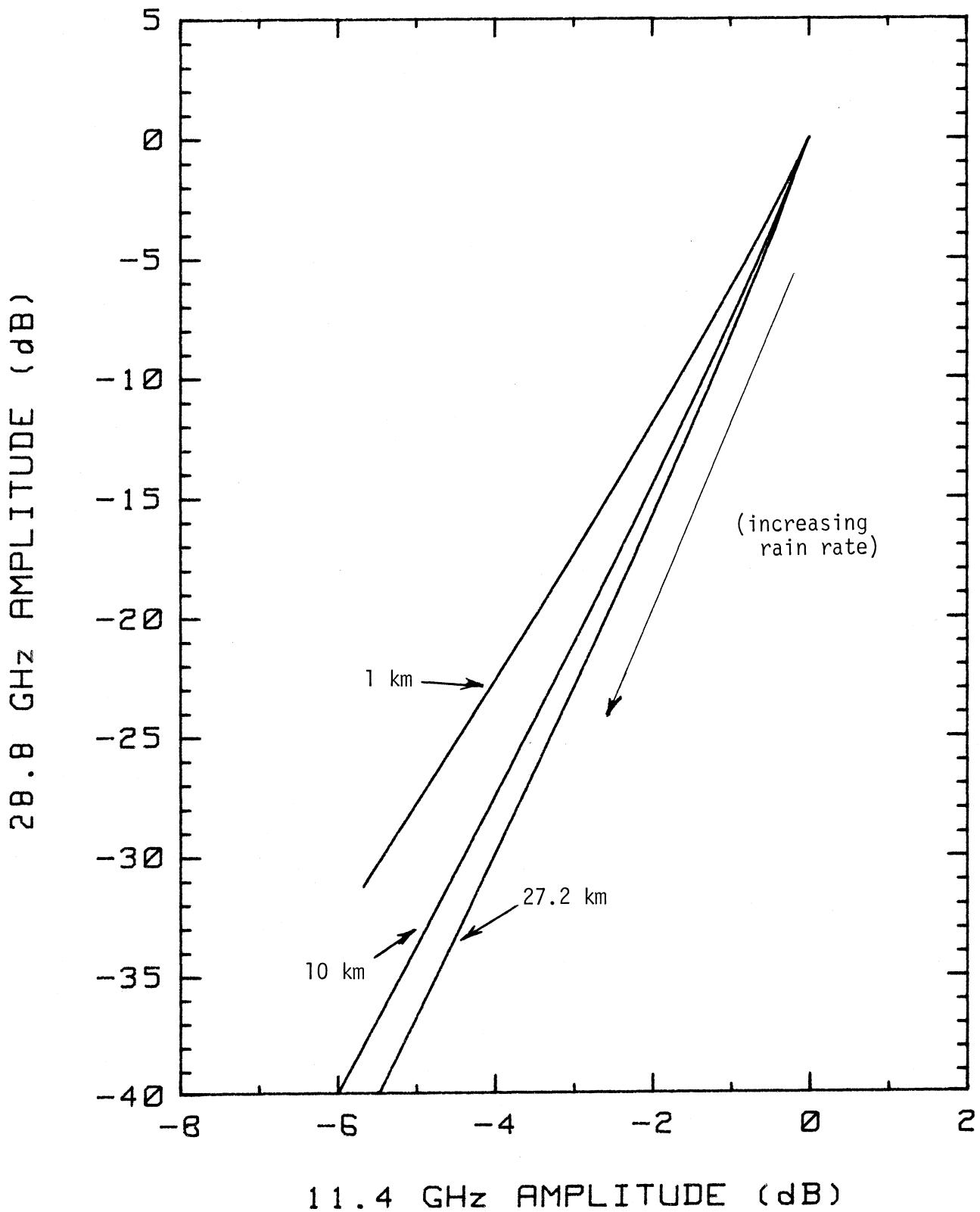


Figure 5.4. Signal amplitude at 28.8 and 11.4 GHz for rain rates of 1, 10, and 27.2-km as the rain rate is varied from 0 to 150 mm/h. Attenuation predicted using (5.4) with the a and b parameters of Table 1 for the Laws and Parson's, low rain rate distribution.

are plotted in Figure 5.5 according to the time of year they were observed. The symbols used represent the time of day the event occurred using the following scheme: M-morning, A-afternoon, E-evening, and N-night. As can be seen there is no strong trend in the ratio of attenuation in regard to the time of day that the precipitation occurred. There is also no trend with regard to the time of year except that during the month of July (after Julian day 181) no ratios greater than 6 were observed.

In Figure 5.6 the ratio of attenuation is plotted according to the depth of fade experienced at 28.8 GHz. The symbols used represent the type of precipitation classified according to the following scheme: S-snow, C-convective rain (thunderstorm), and W-wide spread rain. As can be seen there is no strong trend in the ratio of attenuation in regard to the depth of fade experienced at 28.8 GHz. There also is no relationship between the type of rain and the ratio of attenuation apparent in the data. However, the ratios of attenuation associated with snow events are clustered near 3.

In Figure 5.7 a histogram of the ratio of attenuation for all the precipitation events is presented. The sample mean of the ratios is 4.74 and the sample variance is 11.9. Using the sample variance, the standard deviation of the sample mean is 0.33. Thus, with a 95% probability, the sample mean is within 0.66 of the true mean. Comparing the sample mean of the ratios to the contents of Table 2 shows that it is much lower than would be expected based on the popular raindrop-size distributions. Only at very high rain rates do some of the predicted ratios approach the observed mean ratio. Also in Figure 5.7 the spread in observed ratios is much greater than the range of ratios indicated in Table 2. If the ratios of attenuation indicated in Figures 5.3 and 5.4 (Laws and Parsons, low rain rate distribution) are compared to the observations it can be seen that the spread in observed ratios cannot be explained as resulting from variations in the distribution of rain along the path. The only possible explanation is a large drop-size distribution. Thus it is seen that the data indicates a large variation in rain drop-size distribution and that the sample mean ratio is not consistent with the Laws and Parsons, low rain rate, rain drop-size distribution. In fact the sample mean ratio is not consistent with any of the mentioned models except the Joss, thunderstorm distribution and even it seems to predict ratios that are slightly too high.

In Figure 5.8 and 5.9 the histograms of the ratio of attenuation for convective and wide spread rain, respectively, are presented. In both figures the data presents the same aspects as the combined data. No distinction between the two

RATIO OF ATTENUATION (28.8/11.4 GHz)

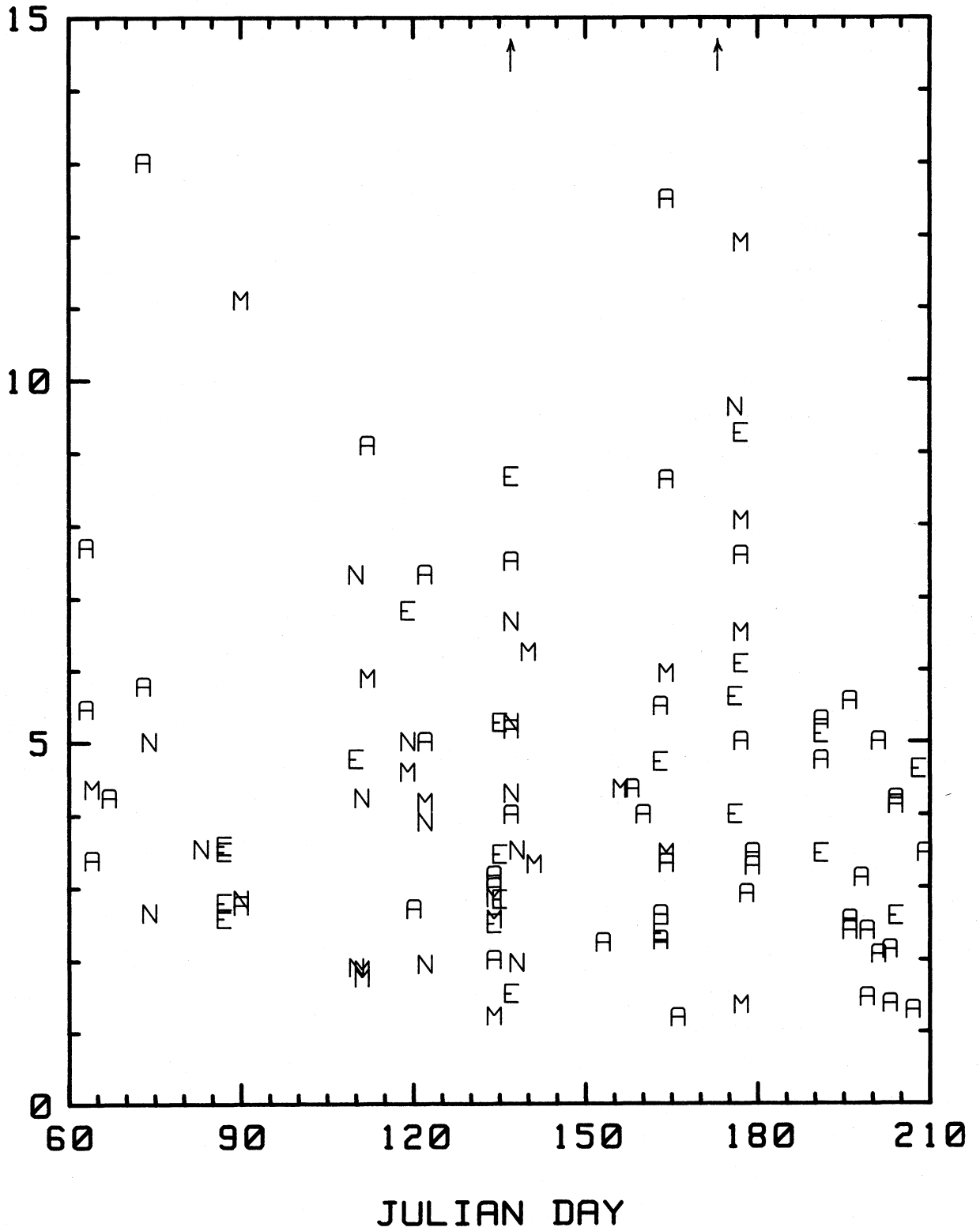


Figure 5.5. Plots of attenuation ratios due to precipitation for 28.8 GHz compared to 11.4 GHz as a function of time of day. Symbols: M = morning, A = afternoon, E = evening, and N = night.

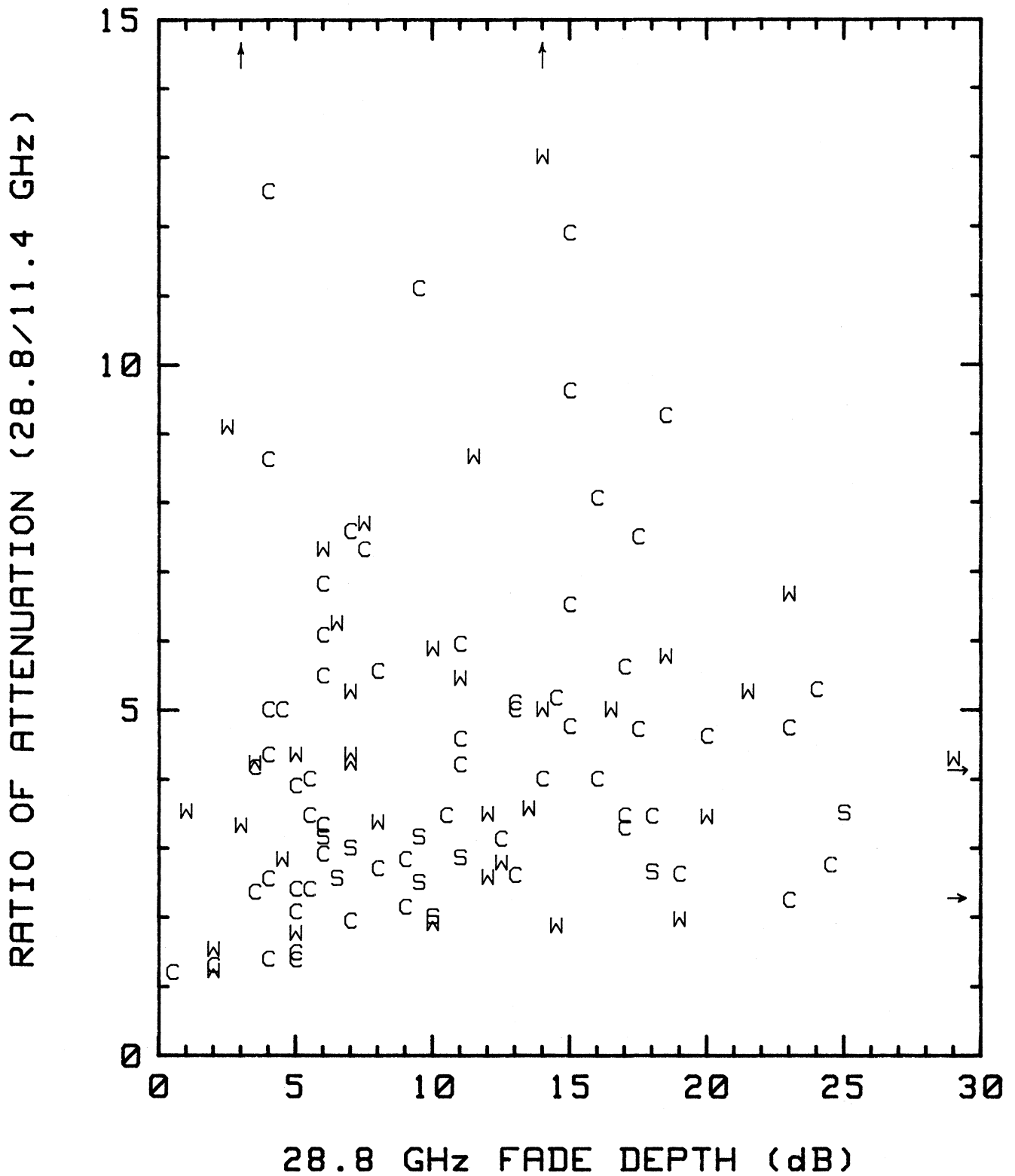


Figure 5.6. Plots of attenuation ratios due to precipitation for 28.8 GHz compared to 11.4 GHz as a function of fade depth at 28.8 GHz. Symbols: S = snow, C = convective rain (thunderstorms), and W = wide spread rain.

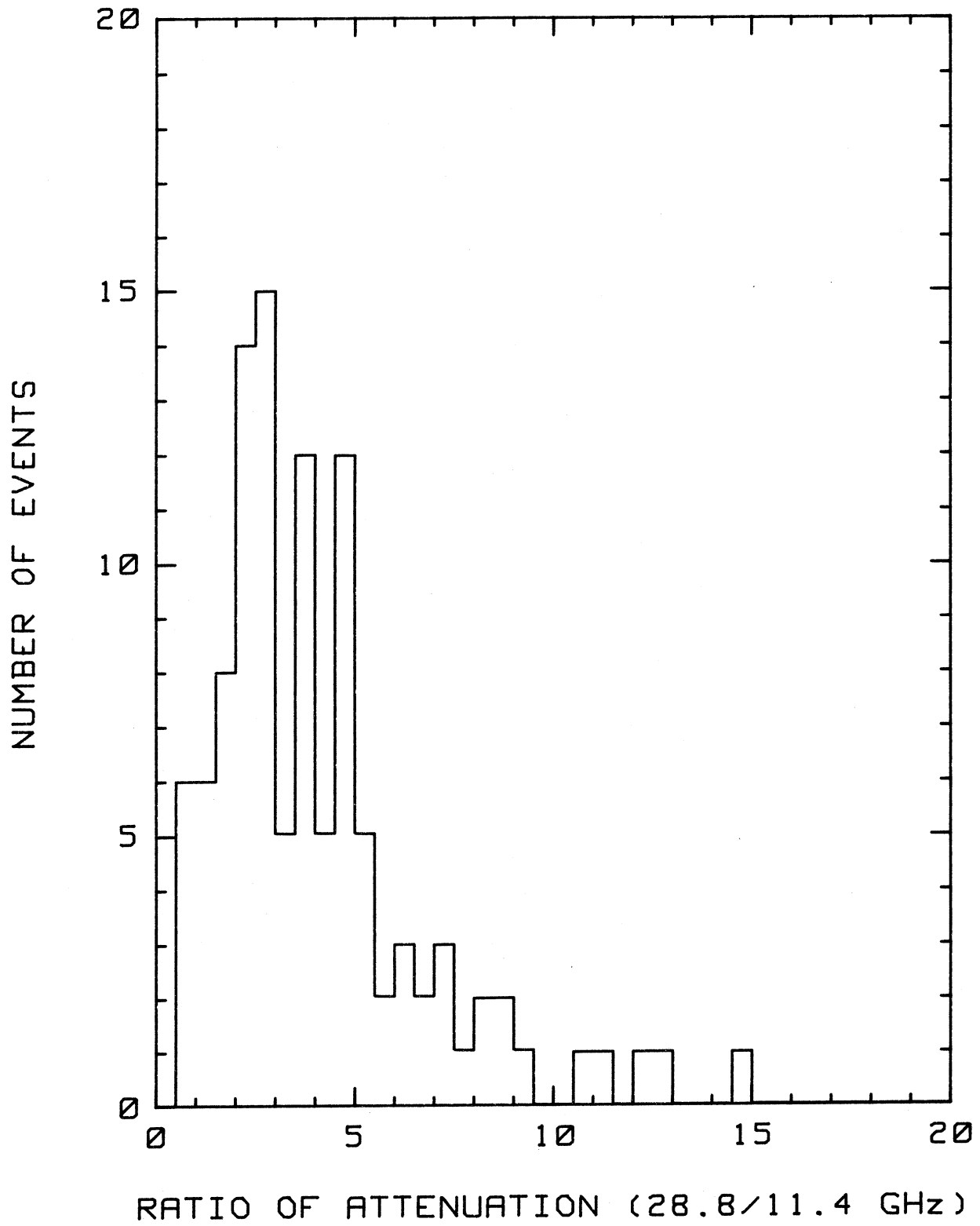


Figure 5.7. A histogram of the ratio of attenuation (28.8/11.4-GHz) for all the precipitation events recorded on the 27.2-km path.

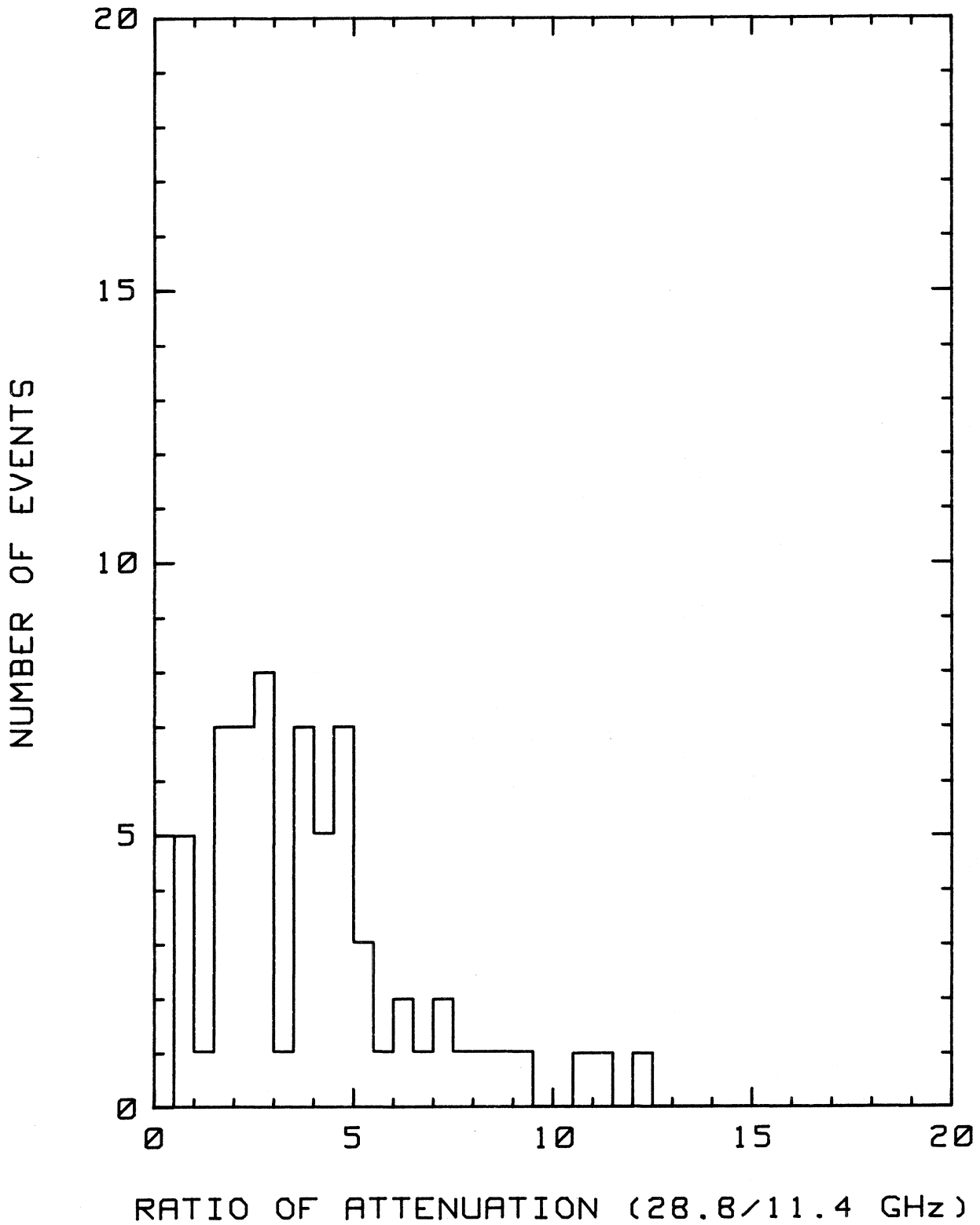


Figure 5.8. A histogram of the ratio of attenuation (28.8/11.4-GHz) for convective type (thunderstorm) rain events recorded on the 27.2-km path.

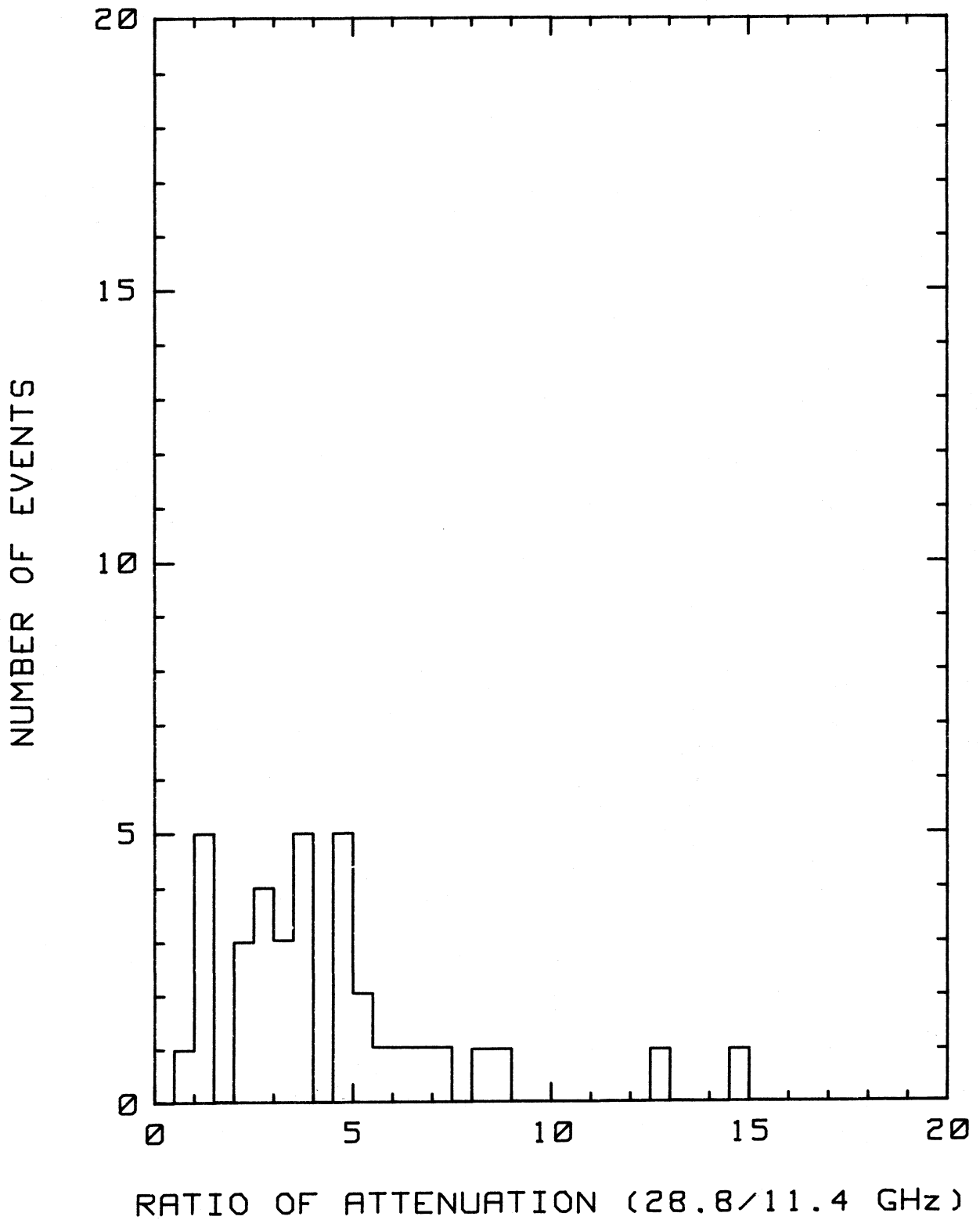


Figure 5.9. A histogram of the ratio of attenuation (28.8/11.4-GHz) for wide-spread rain events recorded on the 27.2-km path.

types of rain is apparent. The sample mean ratios for convective and wide spread rain are 4.93 and 4.87, respectively.

In Figure 5.10 the histogram of the ratio of attenuation for snow events is presented. Only events where significant attenuation occurred are included. During most snows negligible attenuation was observed. These events, therefore, are probably due to snow that is wet and very close to being rain. It must be noted that rain may have occurred somewhere on the path when snowfall was observed at the receiving site. The contrast of this data with the rain data is great. The sample mean ratio is only 2.82 and the sample variance is only 0.2. Thus, the mean ratio is significantly different from that associated with rain. The spread in ratios is much less and indicates that the snow events that cause significant attenuation must be very similar both on the micro and macro scale. Thus, a very specific meteorological condition must occur to produce high attenuation during snow.

5.2 Water Vapor Content and Attenuation

Measurements of the clear air absorption at 96.1 GHz were made by averaging the received signal level in decibels over the 27.2-km path for 1-h periods. Only hours for which clear air conditions existed over the path were used. In addition, only hours in which the signal level remained steady except for scintillation fading were selected. Because the signal level consistently displayed more stability through the midday hours, only hours between 1000 and 1700 local standard time were accepted. These hours of the day are also preferred because the atmospheric turbulence generated by the midday heating of the earth's surface increases the uniformity of the atmosphere along the path.

The calculation of the clear air absorption was based on the calibration of the transmitter and receiver over a 105-m path. The transmitter was then moved out to 27.2 km and two calibrated attenuators (58.3 ± 0.2 dB) were removed from the waveguide feeding the transmitting antenna. The additional free-space loss of the longer path over the shorter path was computed to be 48.2 dB. Thus, the received signal level should have been 10.1 dB higher on the longer path except for the clear air absorption. After operating on the long path during August and September, the 96.1-GHz channel was rechecked on the 105-m calibration path. The signal level was monitored for several days over a range of ambient temperatures and found to be in complete agreement with the calibration made before the measurements. The total peak-to-peak variation in the short path hourly averages of signal level for both calibrations was 0.6 dB and the variations showed no correlation

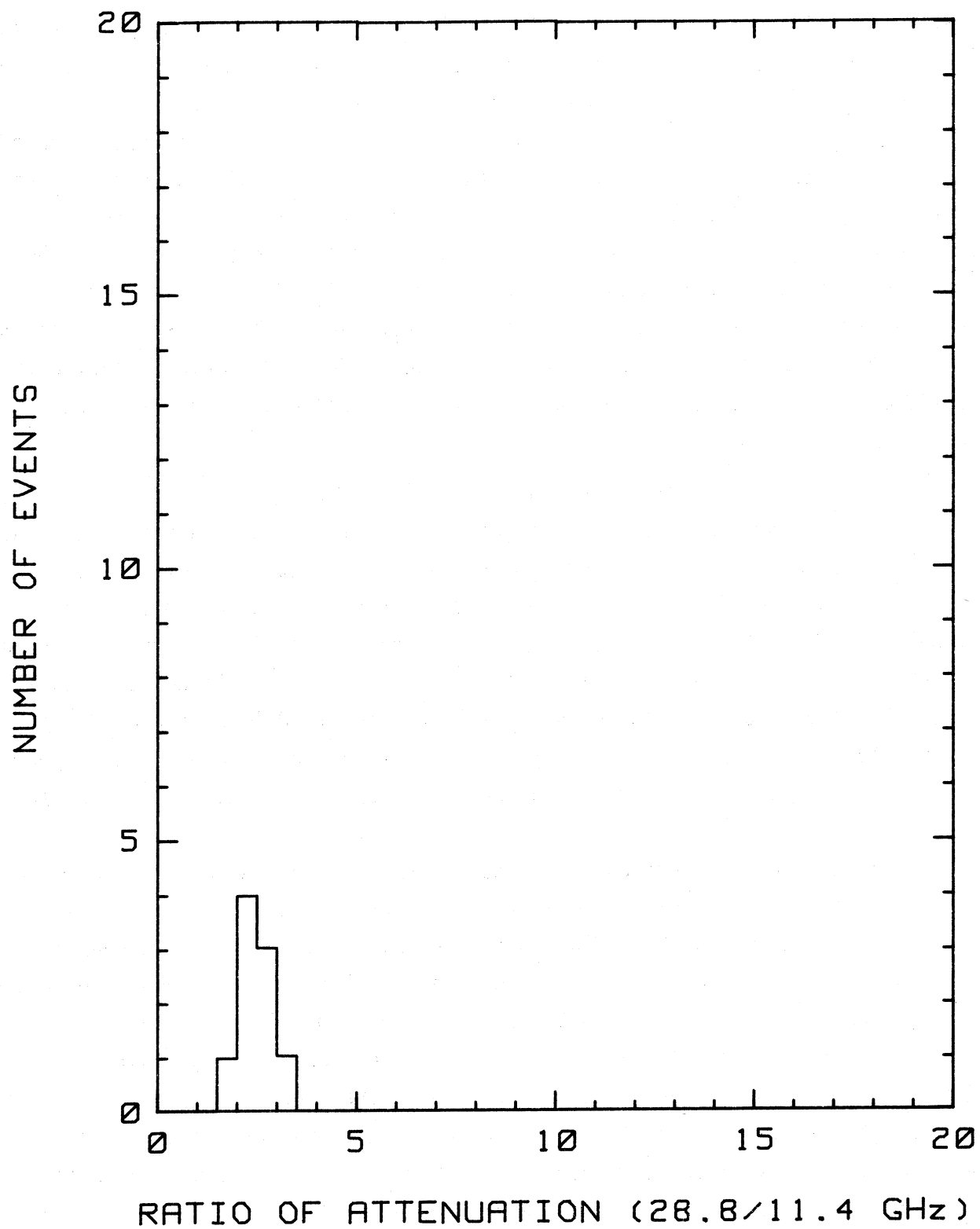


Figure 5.10. A histogram of the ratio of attenuation (28.8/11.4-GHz) for snow events recorded on the 27.2-km path.

with temperature over the range of temperatures for which there is long path data. Therefore, the total long path clear-air absorption measurements should be accurate to within ± 0.3 dB if no other propagation loss mechanisms are considered. This translates into an accuracy of ± 0.01 dB/km for the measurement of the average specific attenuation over the long path.

Of course, clear air absorption depends on various meteorological parameters. Atmospheric temperature, pressure, and refractivity were recorded at the receiving terminal and from the hourly averages of the data, the atmospheric partial water vapor pressure was calculated as described in Section 2.2. The temperature and pressure sensors were calibrated to accuracies of $\pm 0.5^\circ\text{C}$ and ± 1 mb respectively. The refractometer was calibrated to an accuracy of ± 0.5 N. The resulting accuracy for the partial water vapor pressure is ± 0.3 mb.

Since parameters for determining water vapor are measured at only one end of the path, there is some discrepancy possible between them and the path average. The measured temperature averaged over an hour is probably within 2°C of the path average temperature averaged for the hour. The atmospheric pressure variations over the path should be negligible. The path average water vapor pressure is probably very close to that measured at one end of the path when averaged over one hour, say within ± 0.5 mb.

In Figure 5.11, the measured 96.1-GHz specific attenuation is plotted versus the measured water vapor pressure. Although some attenuation at 96.1 GHz is due to absorption by other gases, most of it is due to water vapor and in fact most of it is due to very strong water vapor absorption lines in the infrared. The absorption contributed by these lines in the millimeter wave portion of the spectrum is called the water vapor absorption continuum. Measurements of this continuum appear to be about 5 times stronger than predicted by theory. The model described by Allen and Liebe (1983) was used to subtract the amount of absorption due to dry air and the water vapor lines below 1 THz from the measured values based on the measured pressure, temperature, and water vapor pressure. The remaining absorption is supposedly the water vapor continuum. These measurements of the continuum absorption are shown in Figure 5.12.

Several models of the water vapor continuum absorption have been developed. They are presented here in forms meant to allow easy comparison among them. The Gaut and Reifenstein (1971) model is given by

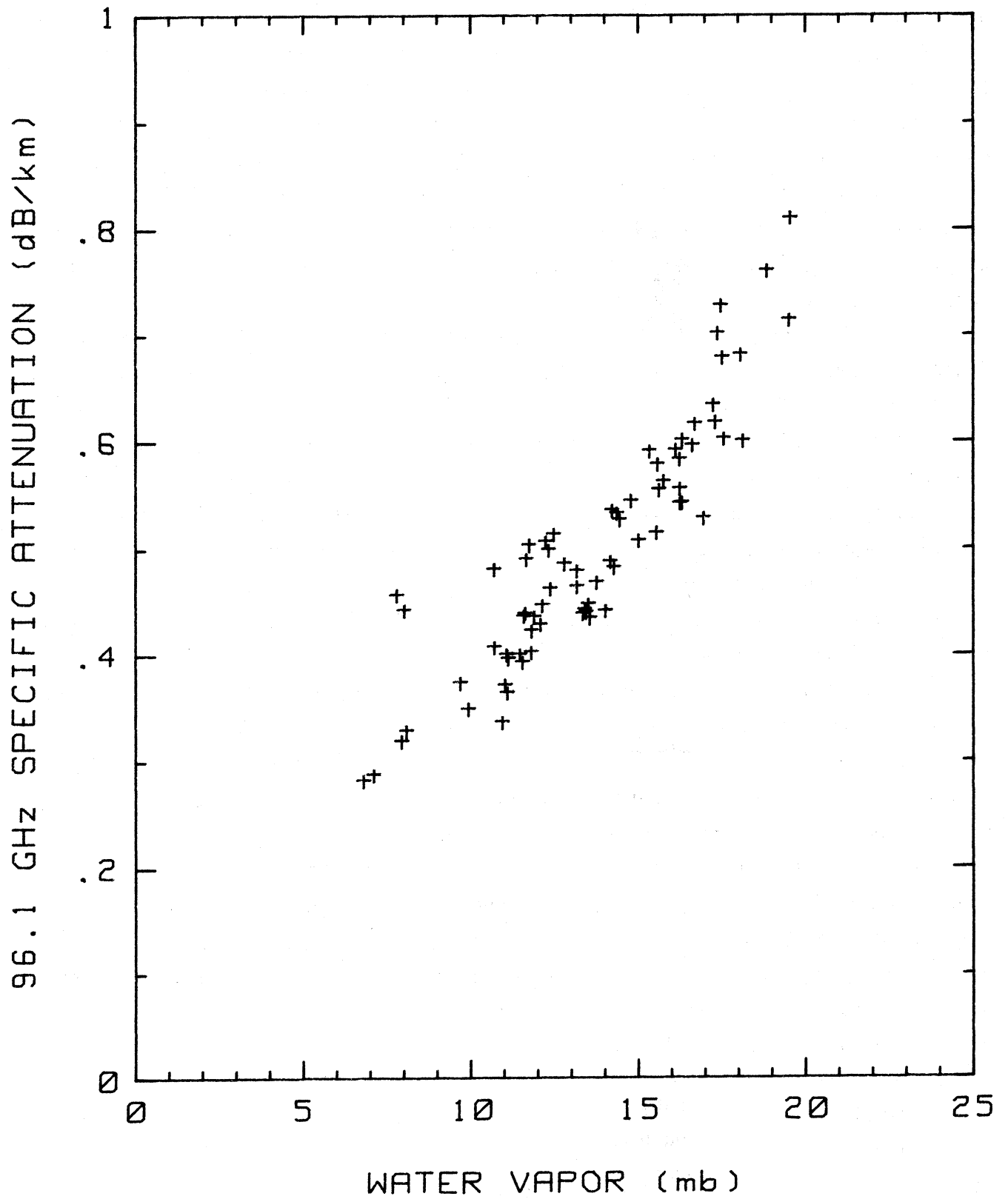


Figure 5.11. A plot of the measured specific attenuation at 96.1 GHz versus the measured water vapor pressure.

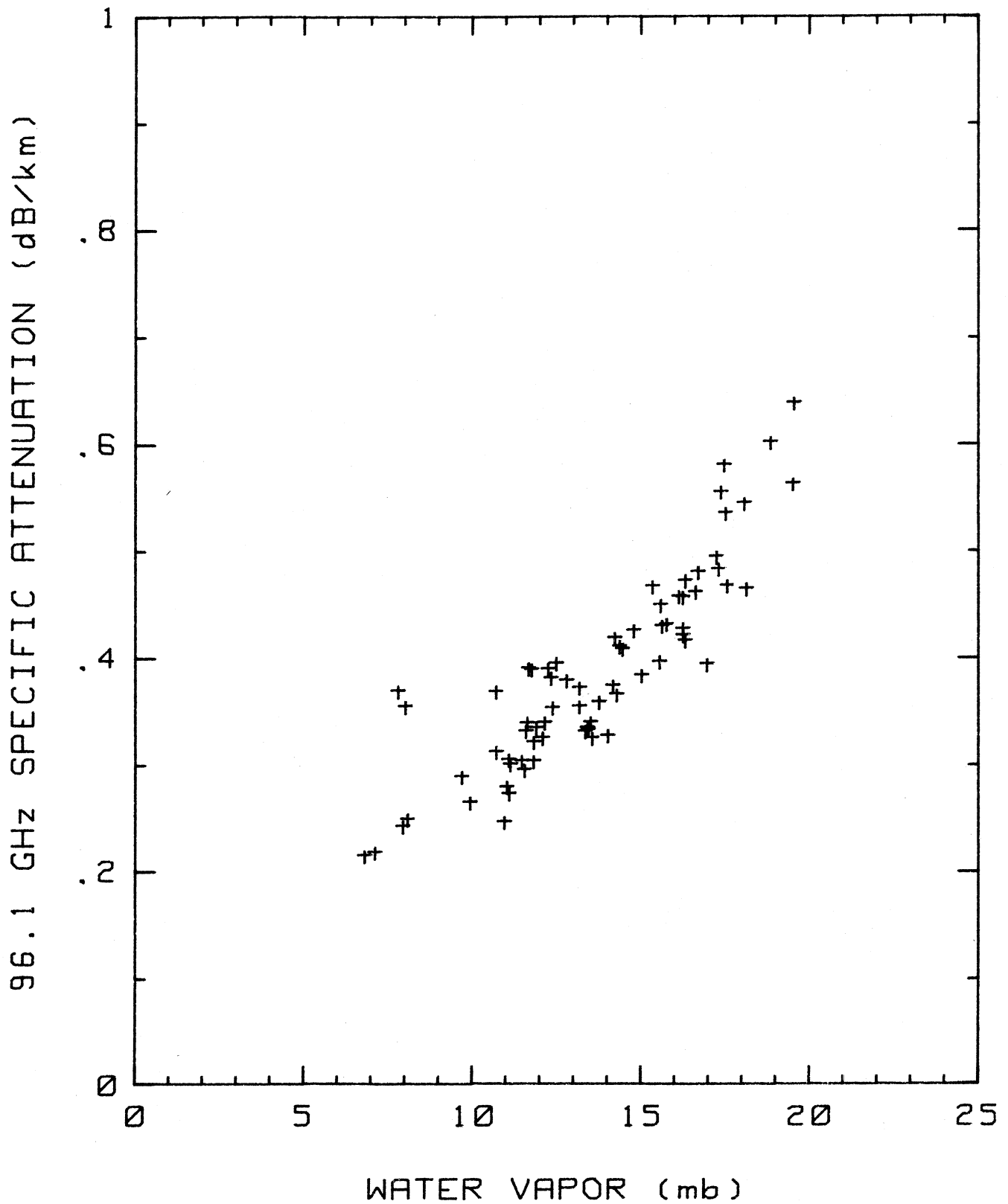


Figure 5.12. A plot of the measured specific attenuation at 96.1 GHz (with the attenuation due to dry-air and water vapor lines below 1 THz subtracted out) versus the measured water vapor pressure.

$$\alpha = 3.39 \times 10^{-9} \cdot E \cdot (P+E) \cdot \theta^{3.1} \cdot F^2, \quad \text{dB/km}; \quad (5.6)$$

the Rice and Ade (1979) model is given by

$$\alpha = 1.68 \times 10^{-7} \cdot E \cdot (P+E) \cdot \theta^{3.1} \cdot F^{1.22}, \quad \text{dB/km}; \quad (5.7)$$

and the Liebe and Layton (1983) model is given by

$$\alpha = (3.39 \times 10^{-9} \cdot E \cdot P \cdot \theta^{2.4} + 1.11 \times 10^{-7} \cdot E^2 \cdot \theta^3) \cdot F^2, \quad \text{dB/km}, \quad (5.8)$$

where F is frequency in GHz, E is water vapor pressure in millibars, P is dry air pressure in millibars, and θ is the relative inverse temperature, $\theta = 300/T$, T in Kelvin. The term (P+E) is the total atmospheric pressure.

The data were compared with these three models. In Figure 5.13 the measured continuum absorption is plotted against the predicted continuum absorption using the Gaut-Reifenstein model. In Figures 5.14 and 5.15 the same type presentations are shown for the Rice-Ade and Liebe-Layton models, respectively. Also presented in the figures are regression lines through the data and the origin. It is apparent in the figures that the Gaut-Reifenstein model fits the data most closely, because the slope of its regression line is closest to the desired value of 1.0 and the scatter of the data about the regression is smallest. These results are summarized in Table 3.

Table 3

Comparison of Data with Models

Model	Mean Square Error of Prediction (dB/km) ²	Slope of Regression	Mean Square Error about Regression (dB/km) ²
Gaut-Reifenstein	2.54×10^{-3}	1.106	1.09×10^{-3}
Rice-Ade	1.26×10^{-2}	0.786	1.09×10^{-3}
Liebe-Layton	3.02×10^{-2}	0.701	1.99×10^{-3}

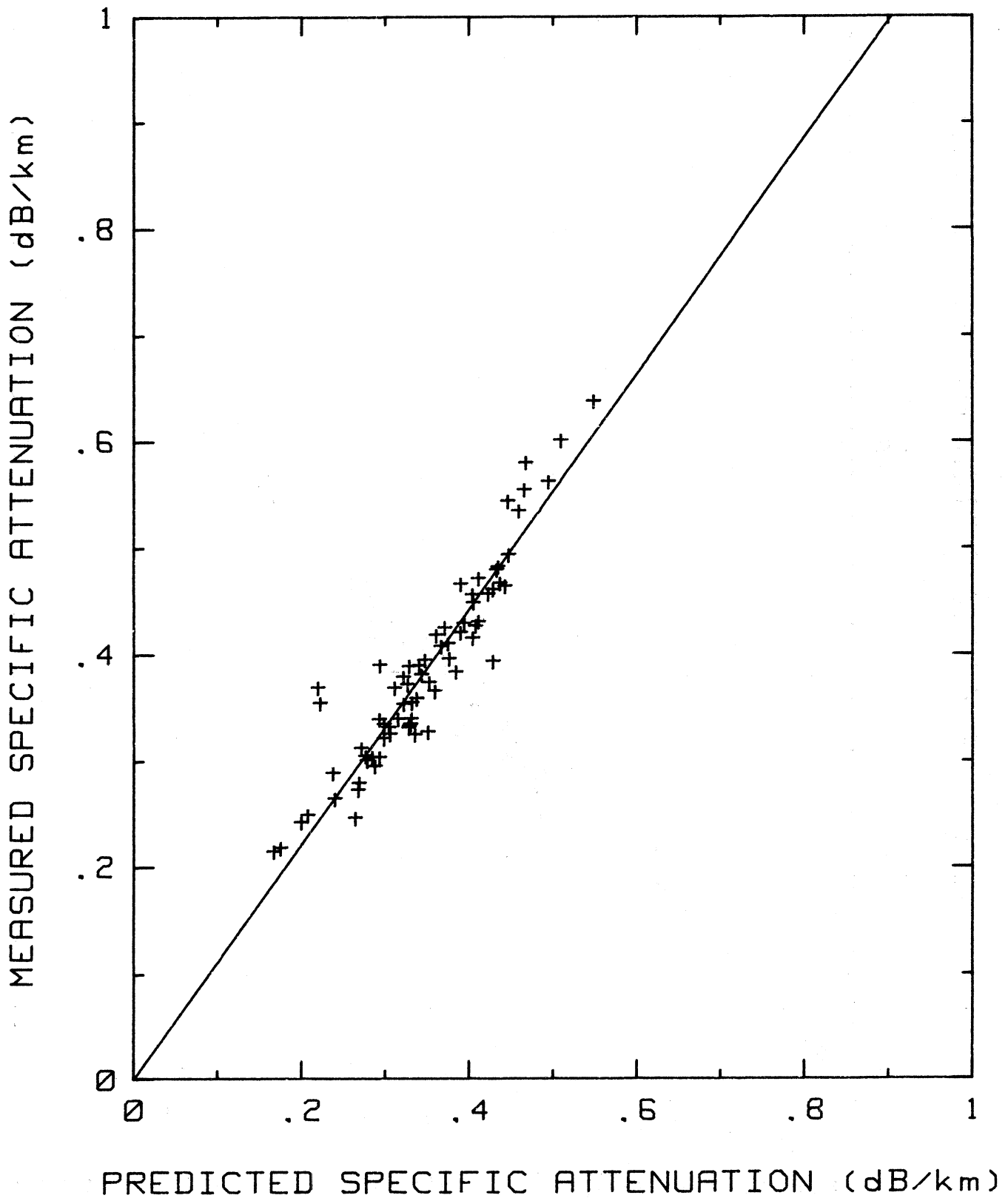


Figure 5.13. A plot of the measured specific attenuation at 96.1 GHz (with the attenuation due to dry-air and water vapor lines below 1 THz subtracted out) versus data from the predicted continuum absorption using the Gaut-Reifenstein model.

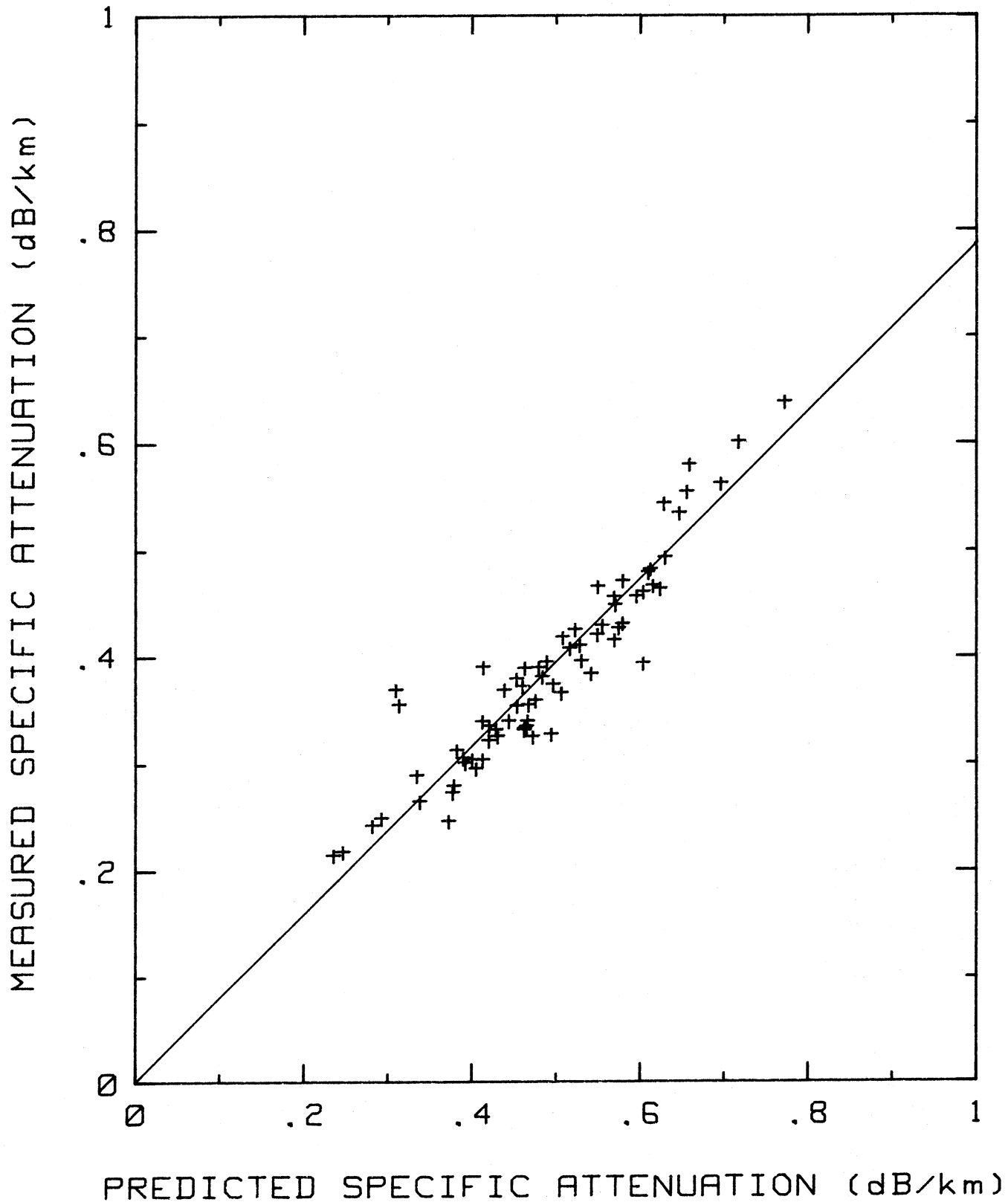


Figure 5.14. A plot of the measured specific attenuation at 96.1 GHz (with the attenuation due to dry-air and water vapor lines below 1 THz subtracted out) versus data from the predicted continuum absorption using the Rice-Ade model.

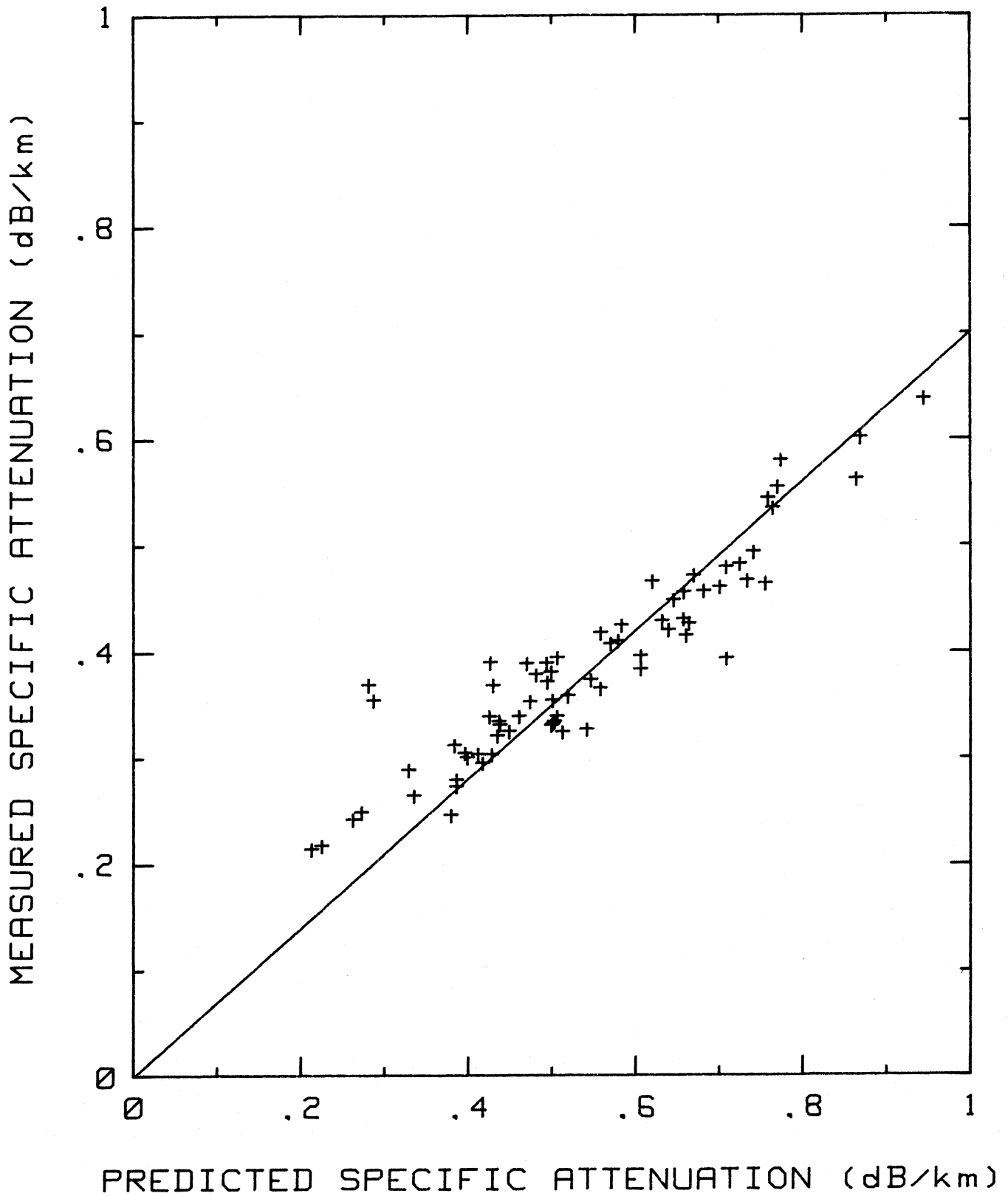


Figure 5.15. A plot of the measured specific attenuation at 96.1 GHz (with the attenuation due to dry-air and water vapor lines below 1 THz subtracted out) versus data from the predicted continuum absorption using the Liebe-Layton model.

5.3 Cumulative Distributions of Bit Error Rate

The bit error rate experienced by the wide-band 500 Mb/s BPSK link at 30.3 GHz over the 27.2-km path was monitored beginning in February 1983 and continuing through September 1983. The bit error rate (BER) was computed by counting the number of errors occurring each second and dividing the count by the number of bits per second. Cumulative distributions of the 1-s BER were recorded hourly.

Subsequently, to aid in the determination of the relative impact on BER of different mechanisms of signal degradation, each hour of data was classified as clear air, fog, snow, or rain according to the weather conditions on the path. The resulting number of hours for each class of data for the months March through August are summarized in Table 4.

Table 4
The number of observation hours of each meteorological classification by month.

Number of Observation Hours					
<u>Month</u>	<u>Clear Air</u>	<u>Fog</u>	<u>Snow</u>	<u>Rain</u>	<u>Total Number of observation hours</u>
March	482	5	102	57	646
April	447	0	78	26	551
May	412	0	29	87	528
June	469	0	0	96	565
July	639	0	0	76	715
August	659	0	0	54	713
Total for March through August	3108	5	209	396	3718

Some of the observation hours classified as rain, snow, or fog also include time of clear-air conditions since precipitation and fog do not stop or begin with the hours of the clock. If these hourly cumulative distributions are added together to create cumulative distributions of BER during rain, snow, or fog, the resulting distributions include arbitrary amounts of clear-air observation time. This inclusion of extra (clear-air) time in the cumulative distribution directly effects the percent of time a given BER is exceeded since it is found by dividing the number of seconds the BER is exceeded by the total number of seconds in the observation period. Thus, an arbitrary error is introduced into the cumulative distribution computed for rain, snow, or fog conditions. Even if the data were not restricted to hourly time periods, the determination of the exact beginning or ending of any

meteorological condition on path would be very subjective and introduce error in the distribution computed for that meteorological condition. Therefore, the computation of distributions of BER for periods of rain, snow, or fog was not attempted.

Instead, monthly cumulative distributions of BER and the portion of these distributions due to rain, snow, and fog were computed. The portion of a monthly distribution due to rain, for instance, is computed by dividing the number of seconds a given BER is exceeded during rain by the total number of seconds of observation time during the month. In this case, the clear-air time included in the data introduces error in the portion of the distribution due to rain only at the very low BER's ($< 10^{-6}$) normally associated with clear-air conditions. Thus, the amount of time during any month that the BER exceeds some threshold due to rain, snow, fog, or clear-air conditions can be found from the portion of the distribution associated with each meteorological condition (except for thresholds $< 10^{-6}$). These portions of the distribution reveal the true significances of each meteorological condition for signal degradation by including not only the severity of the performance impairment but also its likelihood of occurrence. The total time a fixed BER is exceeded is equal to the sum of the times it is exceeded during rain, snow, fog, and clear-air conditions, i.e., the cumulative distribution equals the sum of the portions due to each meteorological condition.

These portions are advantageous for determining the relative impact of the different meteorological conditions as degraders of BER performance for the given system/path configuration. For example, in Figure 5.16, the cumulative distribution of BER for March 1983 and the portions due to each meteorological classification are shown.

Although the number of bit errors during fog may be higher than the number of errors experienced during an equivalent interval of time under clear-air conditions, in the figure the portion of the distribution due to fog is lower than that due to clear-air because fog was only observed for 5 hours while clear-air conditions prevailed on the path for 482 hours. That is, so many errors occurred under clear-air conditions that any additional errors due to fog were insignificant. Also, although it snowed on the path during 102 observation hours and only rained during 57 hours, the degradation in the signal during rain was so much more severe that the portion of the cumulative distribution due to rain is approximately 10 times that for snow.

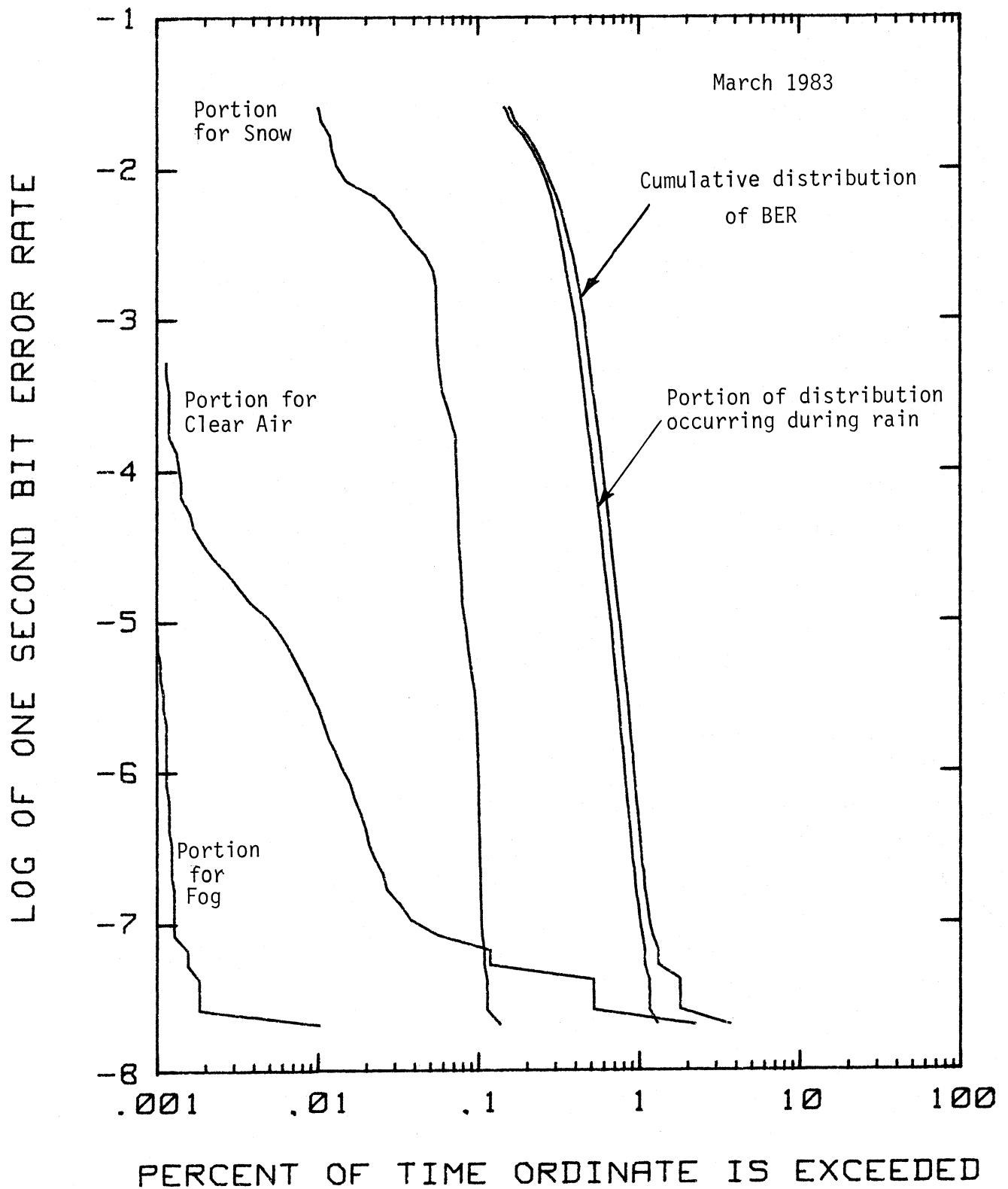


Figure 5.16. Cumulative distribution of BER and the portion of the distribution contributed under each meteorological classification recorded during March, 1983 on the 27.2-km path.

Since the cumulative distribution of 1-s BER lies just above the portion of the distribution due to rain, rain is seen to have been the primary impairment to performance, accounting for nearly all the increase in BER above 10^{-6} during March 1983.

Cumulative distributions for April through August 1983 are presented in Figure 5.17 through 5.21, respectively. The data are presented in the same manner as that for March 1983 in Figure 5.16 discussed above. The portion of the distributions due to clear-air conditions vary widely from month to month.

Unfortunately, the portions of the distributions due to clear-air are not indicative of any propagation-related degradation of the signal. Rather, the variability in the clear-air distributions are due to equipment. Voltage transients from air conditioners, induction motors, soldering guns, etc., sometimes generated momentary high error rates; even though they are of short duration they heavily weight the average BER.

There was a gradual degradation in performance caused by slight drifts in phase positioning of the reconstructed carrier, in decision timing for testing the voltage output of the matched filter, and in the reconstructed clock phase positioning at the BER detector. Because the signal level fluctuates due to scintillation caused by the atmosphere, it was difficult to consistently re-adjust to the same optimum performance level. Finally, periods of elevated BER became more and more frequent during July and August. The progressive failure of a component in the BER receiver was the cause of this deteriorated performance.

Tests were conducted to measure BER versus signal-to-noise ratio (S/N) performance, by inserting wideband noise into the received channel (Violette, et al., 1983) with the transmitter and receiver terminals connected back-to-back, and then compared to performance over the 27.2-km atmospheric path. Results indicated that it was not possible to detect a difference in S/N versus BER between back-to-back performance and the 27.2-km path even during rain. As stated earlier it was difficult to perform measurements of this type with precision over an atmospheric path due to scintillation but degradation due to propagation distortion did not exceed a fraction of a decibel in the S/N versus BER performance curve.

From comparisons of the BER with the signal amplitude at 30.3, 28.8, and 11.4 GHz no increase in BER could be associated with multipath during the six months operations reported here. All increases in the BER not related to equipment were due to the decrease in signal-to-noise ratio resulting from signal fading caused by precipitation on the path. In Figure 5.22 the cumulative distribution

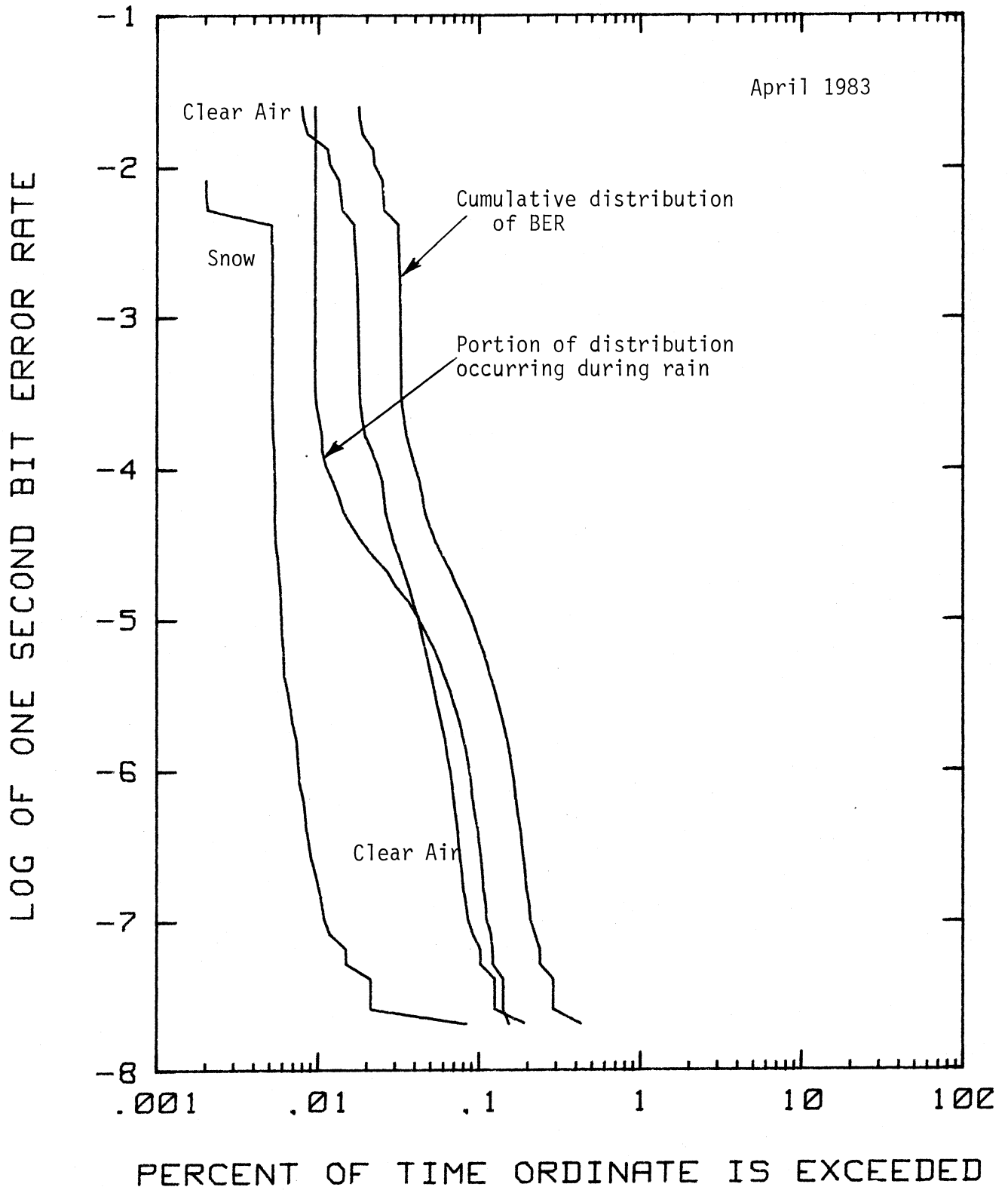


Figure 5.17. Cumulative distribution of BER and the portion of the distribution contributed under each meteorological classification recorded during April, 1983 on the 27.2-km path.

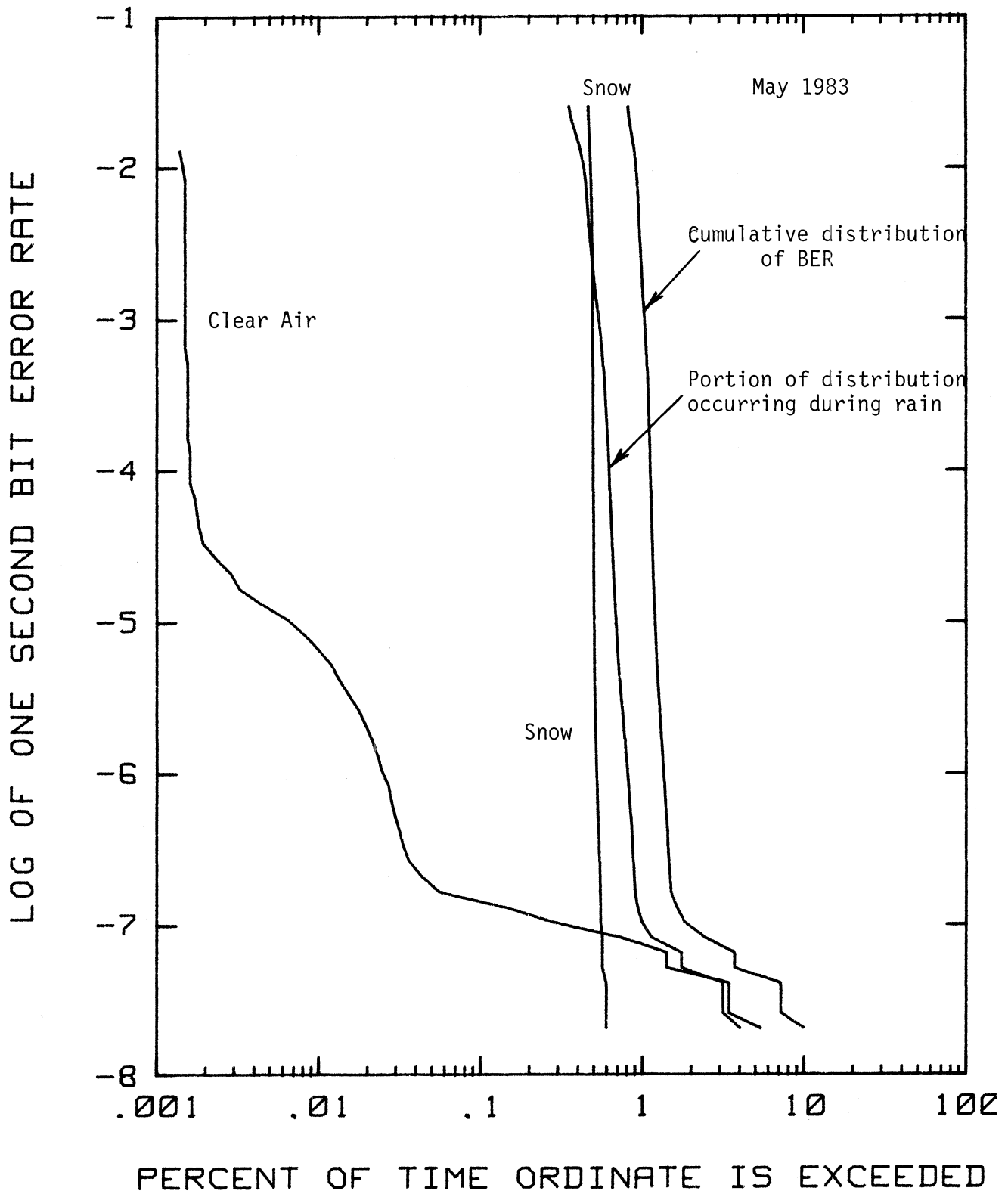


Figure 5.18. Cumulative distribution of BER and the portion of the distribution contributed under each meteorological classification recorded during May, 1983 on the 27.2-km path.

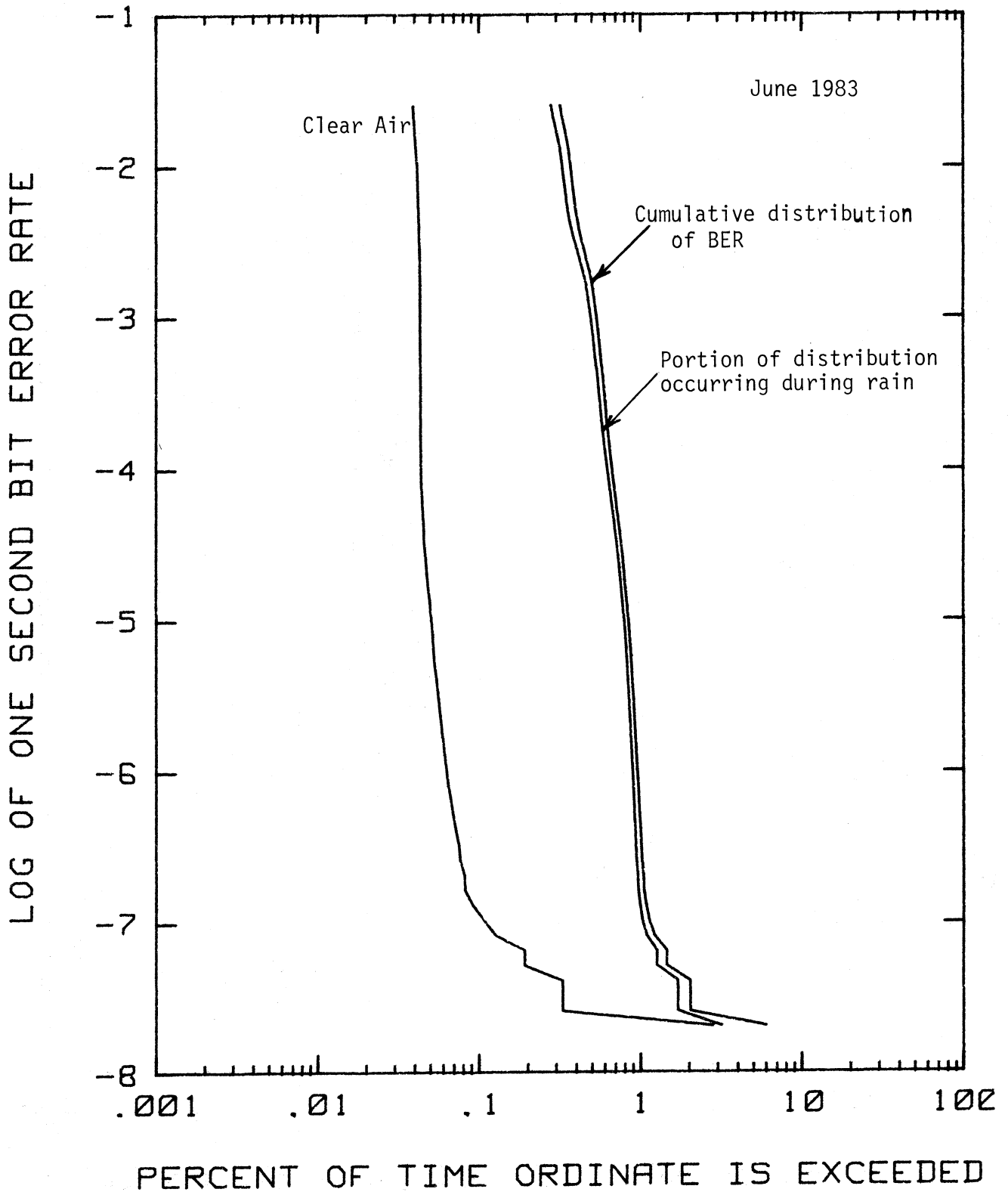


Figure 5.19. Cumulative distribution of BER and the portion of the distribution contributed under each meteorological classification recorded during June, 1983 on the 27.2-km path.

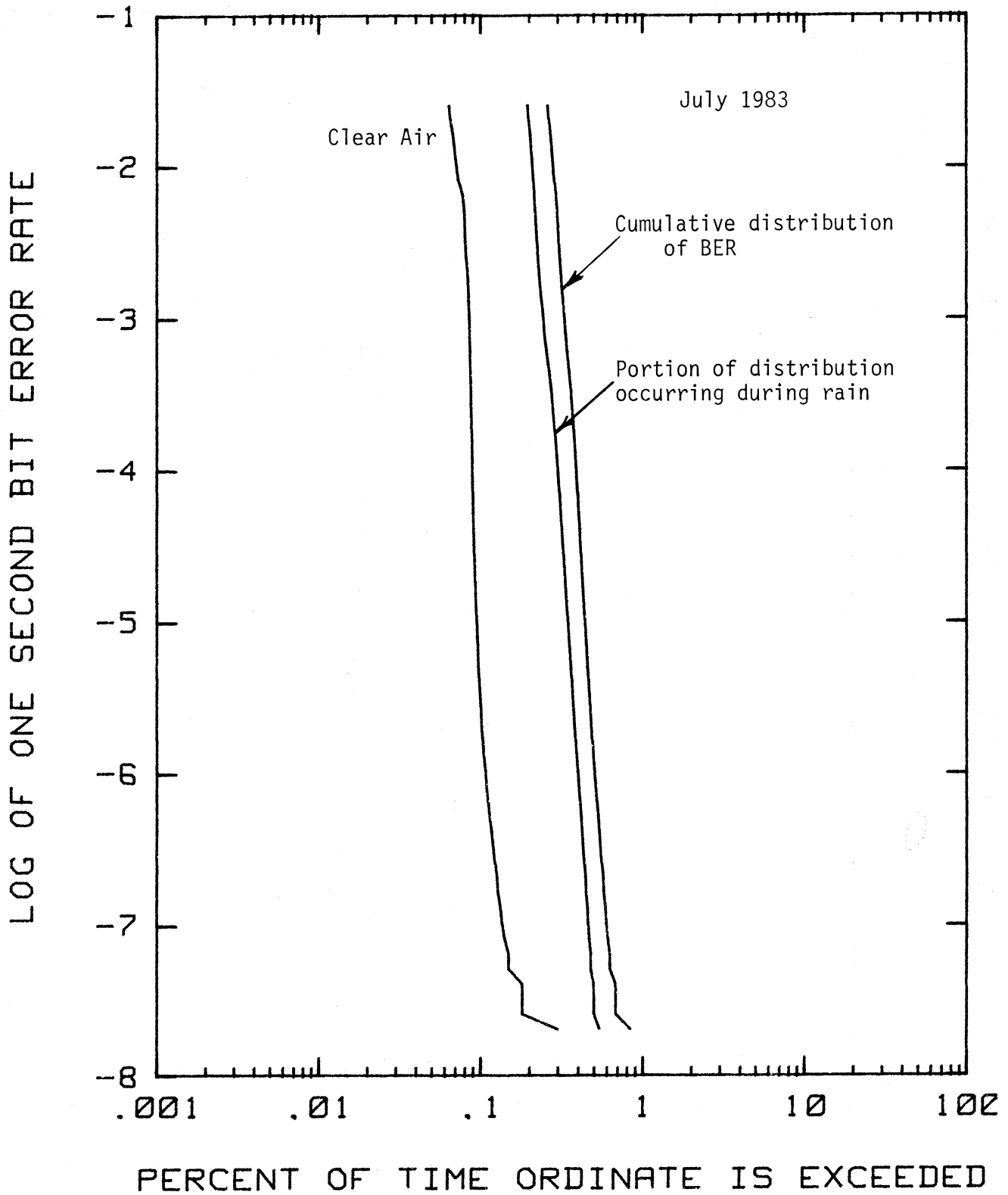


Figure 5.20. Cumulative distribution of BER and the portion of the distribution contributed under each meteorological classification recorded during July, 1983 on the 27.2-km path.

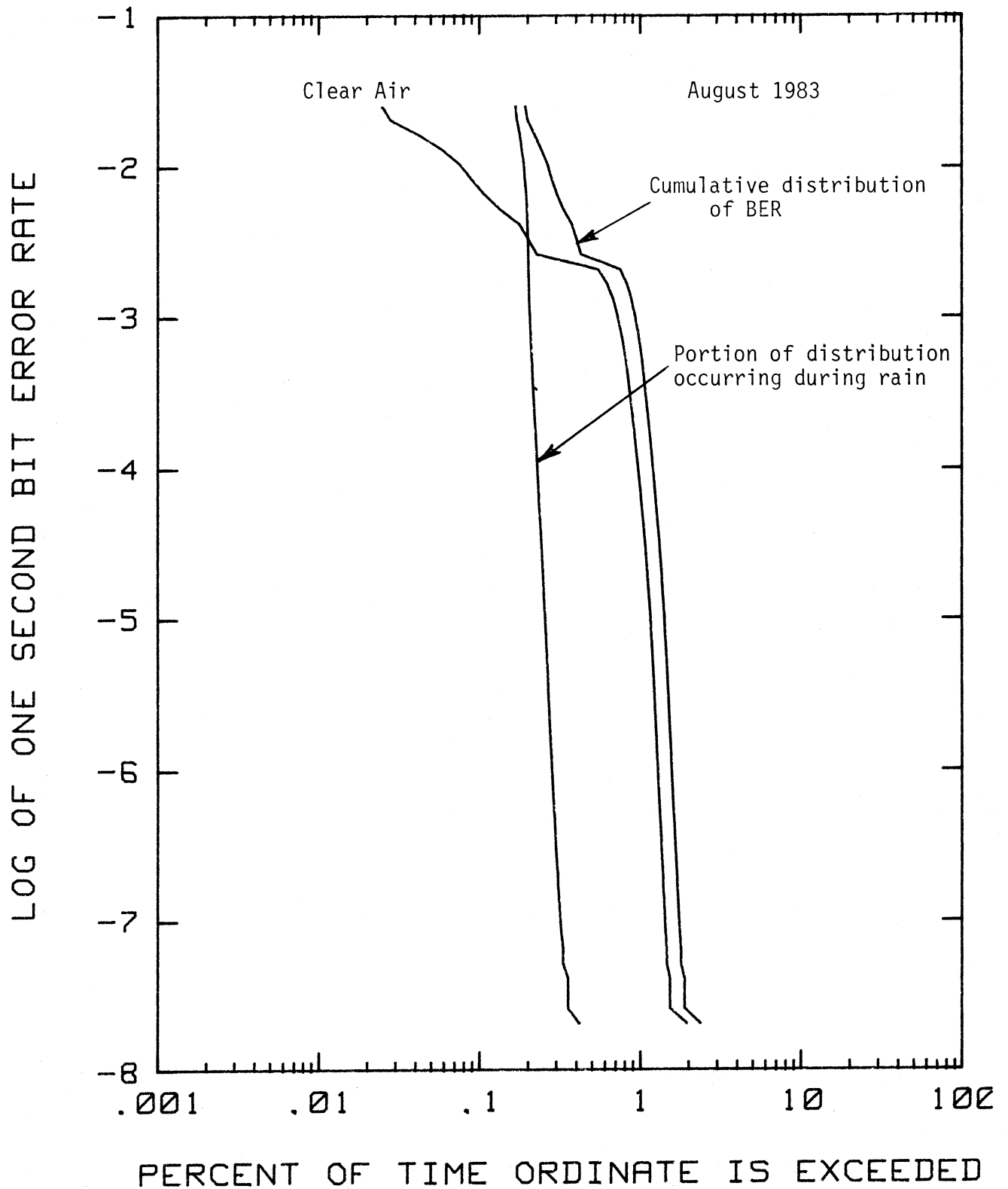


Figure 5.21. Cumulative distribution of BER and the portion of the distribution contributed under each meteorological classification recorded during August, 1983 on the 27.2-km path.

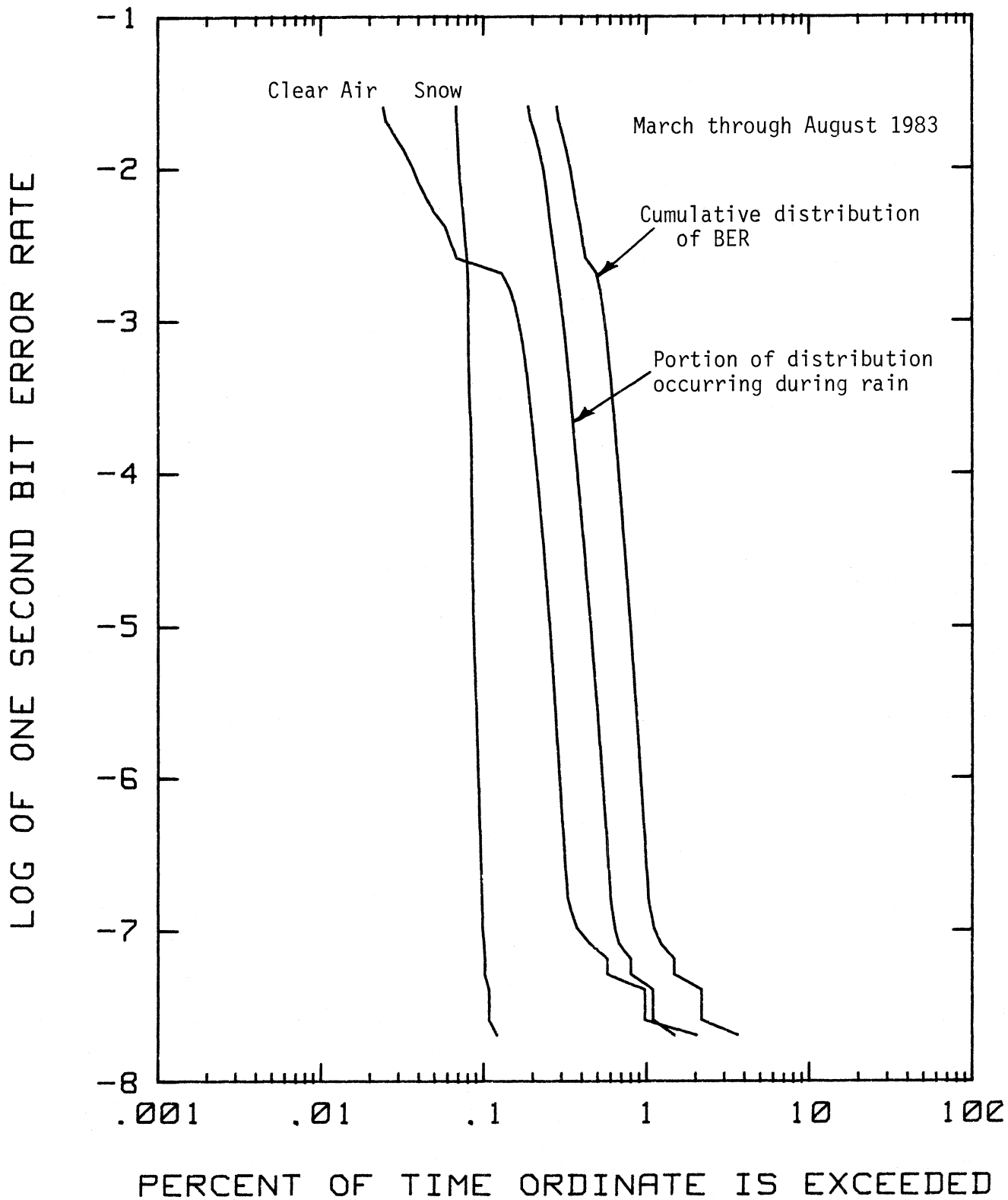


Figure 5.22. Cumulative distribution of BER and the portion of the distribution contributed under each meteorological classification for all recorded data from March through August, 1983 on the 27.2-km path.

and the portions due to each meteorological classification for the total observation period of March through August 1983 are shown. The portion of the distribution due to snow on the path is determined by those few events when deep fading was associated with snow discussed in Section 5.1. During most of the time when it snowed on the path, little attenuation occurred, with no significant increase in the BER. In the figure it can be seen that rain was the primary cause of increased BER. Rain together with snow melting as it fell accounted for essentially all the bit errors and essentially determined the total cumulative distribution of BER.

For the total observation period, disregarding equipment related errors, the BER exceeded 0.001 less than 0.5 percent of the time. The cumulative distributions for each of the 6 months are presented in Figure 5.23. May showed the worst performance with the BER exceeding 0.001 for 1 percent of the time and April was the best month with the BER exceeding 0.001 for less than 0.04 percent of the time.

6. CONCLUSIONS

The diagnostic probe operating at 30.3 GHz with 500 Mb/s BPSK modulation and at 11.4, 28.8, and 96.1 GHz with cw channels was first calibrated on short paths (105 m and 125 m) and then operated on an 11.8 km link to verify system performance and to collect data during a controlled multipath mode of operation. The most significant information learned on this path was the absence of detectable time delay spread distortion during rain as sensed by observation of the BER of the 30.3-GHz 500 Mb/s channel. Also, the amplitude and delay time of multipath signals were measured with the impulse response probe and the resulting effect of intersymbol interference distortion on the BER was recorded.

The probe was operated on a 27.2-km, line-of-sight path at frequencies of 11.4, 28.8, and 30.3 GHz from mid-February through mid-September 1983. The 96.1-GHz channel was added on August 9, 1983, and was also operated through the middle of September. During these periods, received signal levels and BER were recorded for all available channels except for short periods of system repair and adjustment. Meteorological data, including rain rate, temperature, barometric pressure, and the refractive index (N) were also recorded at the receiving terminal.

Clear-air scintillations and fades of the order of 2 to 3 dB were typically observed during the spring and 6 to 8 dB during the summer. Deeper fades were observed during rain and in the presence of atmospheric multipath. Essentially no increase in attenuation occurred during snow, except for a few periods of very wet snow or rain and snow mixed. Two separate periods of fog on the path showed maximum attenuations of 8 and 5 dB at 30.3 GHz and 6 and 4 dB at 28.8 GHz, respectively,

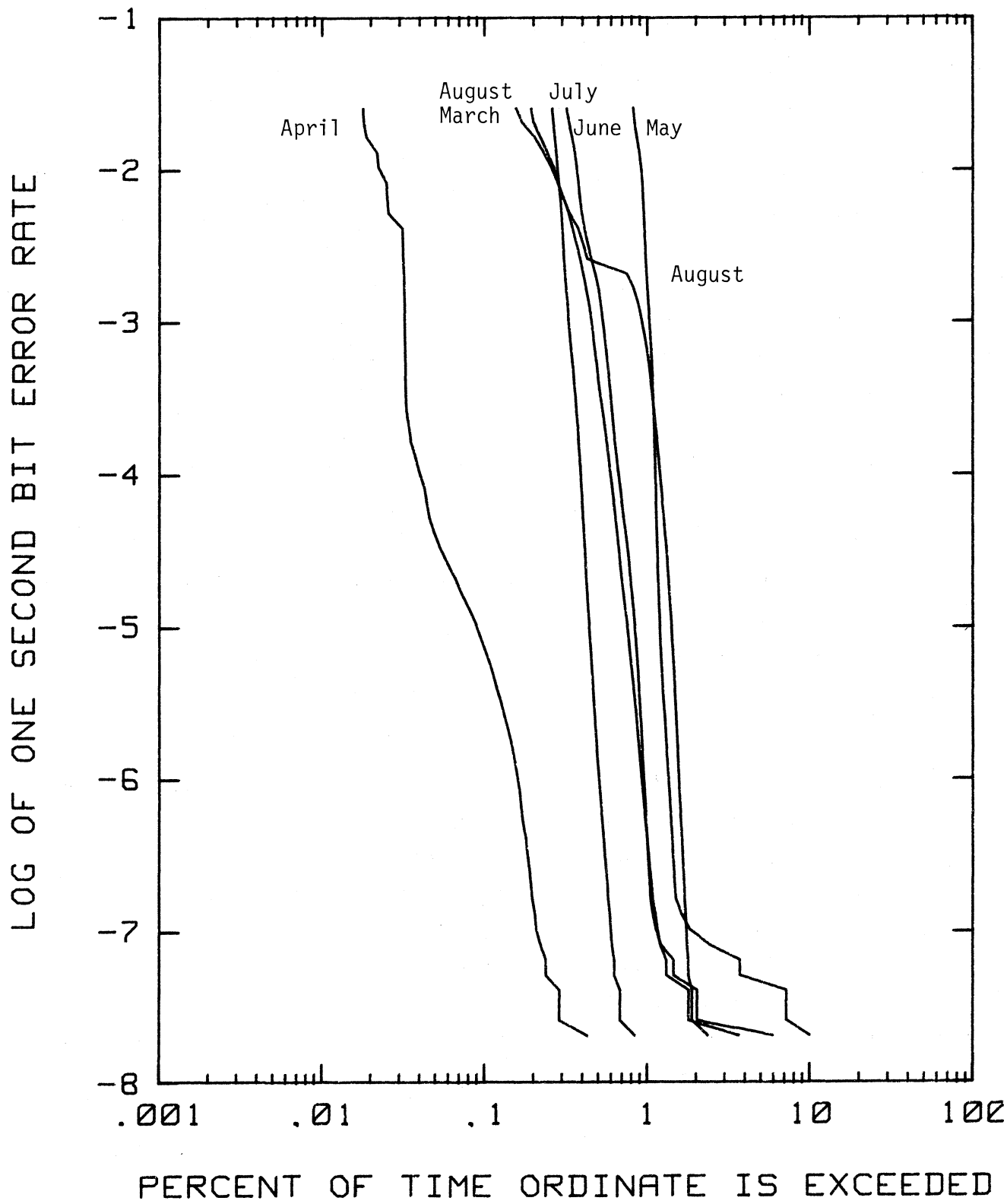


Figure 5.23. Cumulative distributions of BER for each month on the 27.2-km path from March through August, 1983.

Cumulative distributions of bit error rate (BER) measured on the 30.3-GHz, 500 Mb/s channel from transmission on the 27.2-km path are presented by month from March through August 1983. These data show that the most significant contributor to high BER is rain. Deterioration and eventual failure of a component in the error detector circuit produced erroneously elevated BER data for the channel when actual clear-air values were consistently in the 10^{-9} to 10^{-11} range with fades less than about 10 dB. For the total observation period, and disregarding times when the equipment was not operating because of calibration or system modification, the BER exceeded .001 less than 0.5 percent of the time. May was the month showing the worst performance with the BER exceeding .001 one percent of the time and April showed the best performance with the BER exceeding .001 less than 0.04 percent of the time.

For a comparison, a specification of error performance and outage of a digital system using a percent-of-time interval measure described by the International Telephone and Telegraph Consultative Committee (CCITT) states that two specific performance criteria have thus far been adopted for an international connection at 64 Kbits/s. They are that

at least 90 percent of 1-minute intervals have error rates of 10^{-6} or less averaged over that minute, and that

at least 92 percent of 1-second intervals be error-free.

The cumulative distribution data (Figures 5.12 through 5.17) show that for the overall period (March through August) 96 percent of the 1-s intervals had error rates of 2×10^{-8} or less averaged over the second. These results indicate high performance with potential for further improvement if operated as a dedicated link, instead of a developmental-experimental channel.

A 96.1-GHz channel developed and calibrated for the 27.2-km path performed well during clear-air conditions, but showed levels of scintillation up to 15 dB. It also shows higher levels of attenuation due to rain during the approximately 1-month period from mid-August through mid-September

and no measurable attenuation on the 11.4-GHz channel. During periods of heavy rainfall, the signal attenuation for both the 28.8 and 30.3-GHz channels exceeded the system fade margin (33 dB for 28.8 GHz and 30 dB for 30.3 GHz). Likewise, attenuation of the 96.1-GHz received signal level (due to rain) exceeded the fade margin of 32 dB. Maximum attenuation of the received signal level due to rain on the 11.4 GHz channel reached 25 dB, but did not exceed the 41 dB fade margin. Multipath fades of the order of 15 to 20 dB were observed for short periods on all channels, primarily in the early morning hours during the summer. Information indicating the fade mechanism was atmospheric multipath is drawn from the use of multiple frequency channels. A strong correlation was observed between the BER and the received signal level of the 30.3-GHz channel, suggesting that almost no distortion occurred in propagation over this atmospheric channel. As the received signal level decreased more than 10 dB below an average clear-air level, the BER increased above the 1×10^{-8} minimum display level. These fades, observed primarily during rain and periods of multipath, showed a normal dependence on system signal-to-noise ratio and no detectable degradation due to time delay or amplitude dispersion within the 1-GHz bandwidth. Impulse response measurements recorded during periods of clear-air fades support the conclusion that the 27.2-km path produced only atmospheric multipath signals with delay times very short compared to the 2 ns bit duration and therefore did not cause errors due to intersymbol interference.

Cross-plots of measured signal attenuation due to rain at 11.4 and 28.8 GHz show fade ratios that are nearly constant for periods of time during the fade. These observations are compared to predictions based on popular raindrop-size distribution models. No strong trend was observed in the ratio of attenuation at 28.8 GHz to that at 11.4 GHz as a function of type of storm, time of day, or season (data available only for spring and summer). Histograms of the ratio of attenuation at 28.8 GHz to that at 11.4 GHz for all precipitation events indicate that the sample mean of the ratios (4.74) is lower than would be expected based on predicted values of the popular raindrop-size distribution models.

Values for gaseous absorption at 96.1 GHz were calculated from hourly averages of received signal level and densities of the main constituents producing attenuation (oxygen and water vapor) were determined from meteorological data recorded for the 27.2-km path. These data when corrected for dry-air absorption were compared to three prediction models: Gaut-Reifenstein, Rice-Ade, and Liebe-Layton. The measured data produced the best fit when compared to the Gaut-Reifenstein model.

7. REFERENCES

- Allen, K. C. (1983), Attenuation of millimeter waves on earth-space paths by rain clouds, NTIA Report 83-132, August (NTIS Access. No. PB84-115120).
- Allen, K. C., R. H. Ott, E. J. Violette, and R. H. Espeland (1982), Height-gain study for 23 km links at 9.6, 11.4, and 28.8 GHz, IEEE Trans. Ant. Prop. AP-30, No. 4, pp. 734-740.
- Allen, K. C., and H. J. Liebe (1983), Tropospheric absorption and dispersion of millimeter and submillimeter waves, IEEE Trans. Ant. Prop. AP-31, No. 1, pp. 221-223.
- CCIR (1978), Radio emission due to absorption by atmospheric gases and precipitation, Volume 5, Report 720, International Telecommunication Union, 2 Rue Varembe 1211, Geneva 20, Switzerland.
- CCIR (1978), Attenuation and scattering by rain and other atmospheric particles, Volume 5, Report 721, International Telecommunication Union, 2 Rue Varembe 1211, Geneva 20, Switzerland.
- Crombie, D.. (1983), Characteristics of lower atmospheric influence on radiowave propagation, AGARD Conference Pre-print 346.
- Dutton, E. J. (1977), Precipitation variability in the U.S.A. for microwave terrestrial system design, OT Report 77-134 (NTIA Access No. AD A049041).
- Dutton, E. J., H. K. Kobayashi, and H. T. Dougherty (1982), An improved model for earth-space microwave attenuation distribution prediction, Radio Sci. 17, No. 6, pp. 1360-1370.
- Gaut, N. E., and E. C. Reifenstein, III (1971), Interaction model of microwave energy and atmospheric variables, NASA Report CR-61348, N7125079.
- Gray, J. S. (1969), Signal conditioning, bit synchronization, and group synchronization for high bit rate PCM, National Telemetry Conference, Washington, D. C.
- Gray, J. W. (1972), Signal processing for digital communications for a 1 Gb/s data rate, International Communications Conference, Philadelphia, PA.
- Kerr, D. E. (1951), Propagation of Short Radio Waves, (McGraw-Hill Book Co., New York, NY), p. 672.
- Liebe, H. J. (1981), Modeling attenuation and phase of radio waves in air at frequencies below 1000 GHz, Radio Sci. 16, No. 6, pp. 1183-1199.
- Liebe, H. J. (1984), The atmospheric water vapor continuum below 300 GHz, International J. Infrared and Millimeter Waves, Vol. 5, No. 5.
- Liebe, H. J., and D. H. Layton (1983), Experimental and analytical aspects of the atmospheric EHF water vapor continuum, Proc. URSI Commission F Symposium, Louvain, Belgium (June ESA SP-194).

- Olsen, R. L., D. V. Rogers, and D. B. Hodge (1978), The aR^b relation in the calculation of rain attenuation, IEEE Trans. Ant. Prop. AP-26, No. 2, pp. 318-329.
- Rice, D. P., and P. A. Ade (1979), Absolute measurements of the atmospheric transparency at short millimetre wavelengths, Infrared Phys. 12, pp. 575-584.
- Skolnik, M. T. (1962), Introduction to Radar Systems (McGraw-Hill, New York, NY), p. 364.
- Smith, E. K., and S. Weintraub (1953), The constants in the equation for atmospheric refractive index at radio frequencies, Proc. IRE 41, pp. 1035-1037.
- Violette, E. J., R. H. Espeland, and K. C. Allen (1983), A diagnostic probe to investigate propagation at millimeter wavelengths, NTIA Report 83-128, August (NTIS Access No. PB 84-104223).
- Wait, D. F. (1973), Considerations for the precise measurement of amplifier noise, NBS Technical Note 640, August.

BIBLIOGRAPHIC DATA SHEET

	1. PUBLICATION NO. NTIA Report 84-149	2. Gov't Accession No.	3. Recipient's Accession No.
4. TITLE AND SUBTITLE Atmospheric Channel Performance Measurements at 10 to 100 GHz		5. Publication Date APRIL 1984	6. Performing Organization Code
7. AUTHOR(S) R. H. Espeland, E. J. Violette, and K. C. Allen		9. Project/Task/Work Unit No.	
8. PERFORMING ORGANIZATION NAME AND ADDRESS U. S. Department of Commerce National Telecommunications and Information Administration Institute for Telecommunication Sciences Boulder, Colorado 80303		10. Contract/Grant No.	
11. Sponsoring Organization Name and Address same		12. Type of Report and Period Covered	
		13.	
14. SUPPLEMENTARY NOTES			
15. ABSTRACT (A 200-word or less factual summary of most significant information. If document includes a significant bibliography or literature survey, mention it here.) A diagnostic probe designed to investigate propagation at millimeter wavelengths was operated on 11.8 and 27.2-km line-of-sight paths near Boulder, CO. A 30.3-GHz carrier is biphase-shift-keying modulated at a 500 Mb/s with bit error rates less than 10^{-8} in clear air and a fade margin of about 30 dB on the 27.2-km path. In addition, fully coherent carrier wave channels at 11.4, 28.8, and 96.1 GHz provide data to analyze fade mechanisms and evaluate frequency dependent performance characteristics of the link. Data during fog, snow, rain, and clear-air fade events are included with statistical analyses of event occurrence, signal levels, and bit error rates. Time delay distortion and amplitude dispersion on the channel are also examined during fading events by the wide-band digital channel operated as an impulse probe. Rain attenuation, path absorption due to water vapor content, and seasonal variations as a function of frequency are presented and described.			
16. Key Words (Alphabetical order, separated by semicolons) Atmospheric; diagnostic; digital; millimeter waves, probe; propagation; water vapor; wide band			
17. AVAILABILITY STATEMENT <input checked="" type="checkbox"/> UNLIMITED. <input type="checkbox"/> FOR OFFICIAL DISTRIBUTION.		18. Security Class. (This report) Unclassified	20. Number of pages 119
		19. Security Class. (This page) Unclassified	21. Price:

